



Cite this: *Chem. Soc. Rev.*, 2019,  
48, 310

## An overview on enhancing the stability of lead halide perovskite quantum dots and their applications in phosphor-converted LEDs

Yi Wei,<sup>ab</sup> Ziyong Cheng<sup>\*ab</sup> and Jun Lin<sup>ID \*abc</sup>

Beyond the unprecedented success achieved in photovoltaics (PVs), lead halide perovskites (LHPs) have shown great potential in other optoelectronic devices. Among them, nanometer-scale perovskite quantum dots (PQDs) with fascinating optical properties including high brightness, tunable emission wavelength, high color purity, and high defect tolerance have been regarded as promising alternative down-conversion materials in phosphor-converted light-emitting diodes (pc-LEDs) for lighting and next-generation of display technology. Despite the promising applications of perovskite materials in various fields, they have received strong criticism for the lack of stability. The poor stability has also attracted much attention. Within a few years, numerous strategies towards enhancing the stability have been developed. This review summarizes the mechanisms of intrinsic- and extrinsic-environment-induced decomposition of PQDs. Simultaneously, the strategies for improving the stability of PQDs are reviewed in detail, which can be classified into four types: (1) compositional engineering; (2) surface engineering; (3) matrix encapsulation; (4) device encapsulation. Finally, the challenges for applying PQDs in pc-LEDs are highlighted, and some possible solutions to improve the stability of PQDs together with suggestions for further improving the performance of pc-LEDs as well as the device lifetime are provided.

Received 12th September 2018

DOI: 10.1039/c8cs00740c

rsc.li/chem-soc-rev

<sup>a</sup> State Key Laboratory of Rare Earth Resource Utilization, Changchun Institute of Applied Chemistry, Chinese Academy of Sciences, Changchun, 130022, China.

E-mail: jlin@ciac.ac.cn, zycheng@ciac.ac.cn

<sup>b</sup> University of Science and Technology of China, Hefei, 230026, China

<sup>c</sup> School of Applied Physics and Materials, Wuyi University, Jiangmen, Guangdong 529020, P. R. China



Yi Wei

Yi Wei received his BS degree (2015) from Northeast Normal University (NENU), Republic of China. He is currently pursuing a PhD degree in chemistry at Changchun Institute of Applied Chemistry (CIAC), Chinese Academy of Sciences, under the supervision of Prof. Ziyong Cheng and Prof. JunLin. His research focuses on improving the stability of lead halide perovskite quantum dots, and their applications in solid-state lightings and displays.

### 1. Introduction

Lead halide perovskites (LHPs) have been regarded as promising classes of materials for photovoltaics (PVs) and optoelectronic devices, owing to the unique characteristics, such as long charge



Ziyong Cheng

Ziyong Cheng earned his BS degree in materials engineering from Changchun University of Technology in 1994 and his PhD degree from the Changchun Institute of Applied Chemistry (CIAC), Chinese Academy of Sciences, in 2006. Following postdoctoral studies at the Max-Planck Institute for Polymer Research (Mainz, Germany), he returned to CIAC (2008) to take up an associate professor position in inorganic chemistry. In 2013, he was promoted to a full professor. His research interests are nanostructured materials including perovskite quantum dots in photoelectric applications and polymer-inorganic nanocomposites for biomaterials related fields.

carrier diffusion lengths, precise tunable bandgaps, high light-absorption coefficients, and high defect tolerance.<sup>1–10</sup> Research on LHPs has been gaining increasingly intense interest over the past years. Since the first perovskite photovoltaics with a power conversion efficiency (PCE) of 3.9% came out in 2009, the new record is over 23% now.<sup>1,10</sup> The great success of applying LHPs in PVs has triggered a number of corresponding research studies. Applications of LHPs in the fields including light-emitting diodes (LEDs),<sup>11–20</sup> lasers,<sup>21–26</sup> X-ray imaging,<sup>27–32</sup> and photodetectors (PDs)<sup>33–38</sup> have been massively investigated. Among them, LEDs in particular have attracted worldwide attention with a rapid rise in the electroluminescence (EL) efficiency of perovskite LEDs (PeLEDs).

Perovskite nanomaterials could be divided into five main types by multiple dimensions:<sup>39,40</sup> nanospheres<sup>41</sup>/nanocubes<sup>42</sup> (both of them can be regarded as quantum dots), nanorods<sup>43</sup>/nanowires,<sup>44,45</sup> nanoplates<sup>46</sup>/nanodisks,<sup>47</sup> supercrystals,<sup>48</sup> and polycrystalline films.<sup>49,50</sup> Among them, polycrystalline films and colloidal quantum dots represent the most recent type of LHP materials with promising EL applications.<sup>51</sup> However, due to the low film quality as well as low photoluminescence quantum yields (PL QYs) of LHP polycrystalline films, achieving high EL efficiency PeLEDs is somewhat difficult.<sup>12,15,52</sup> The PL QYs of perovskite quantum dots (PQDs) solution are much higher.<sup>41,53–56</sup> Unfortunately, the charge injection efficiency of PQDs is relatively low owing to the fact that the poor conductive surface ligands block the charge injection.<sup>42</sup> The EQE was successfully improved *via* surface ligand density control, sufficient purification, etc.<sup>57–61</sup> In comparison with the mature technology such as organic LEDs (OLEDs)<sup>62</sup> and CdSe-based QD LEDs (QLEDs)<sup>63,64</sup> that have optimized device structure, further studies are needed to boost the EL efficiency and brightness.



**Jun Lin**

(USA, 1998) and University of New Orleans (USA, 1999). He came back to China in 2000, and since then has been working as a professor at CIAC. His research interests include bulk and nanostructured luminescent materials and multifunctional composite materials together with their applications in the display, lighting, and biomedical fields.

Although luminescent LHPs have led to rapid advancement in EL LEDs and presented the opportunity for lighting devices and the next-generation displays, phosphor-converted LEDs (pc-LEDs) remain in the mainstream at present due to their extraordinary luminous efficiency, high electro-optical conversion efficiency, long operation life, etc.<sup>65–70</sup> The so-called pc-LEDs consist of inorganic phosphors as the down-conversion layer and a blue InGaN chip as the light source. Owing to the highly efficient blue InGaN chip which has been widely recognized as an optimal light emission source, utilizing appropriate color converters plays a pivotal role in the performance of pc-LEDs.

Recently, PQDs with almost every figure of merit, such as high brightness, tunable emission, high color purity, high light-absorption coefficient, high defect tolerance and facile fabrication, have shown promise as phosphors in pc-LEDs.<sup>56,71–85</sup> Especially, PQDs present high color purity together with a narrow full width at half maximum (FWHM) ranging from 12 to 40 nm.<sup>54,71</sup> The color gamut of pc-LEDs composed of PQDs could cover over 140% of the National Television System Committee (NTSC) standard, which is superior to commercial OLEDs and QLEDs.<sup>86–89</sup> All these advantages suggest their potential as color-converters in pc-LEDs for solid-state lighting as well as future displays (Fig. 1).

Despite the huge success achieved in various fields, the applications of perovskite materials are impeded by several issues related to their stability.<sup>90–96</sup> (1) LHPs are highly sensitive to polar solvents due to their inherent ionic nature.<sup>71</sup> They usually lose optical properties, surface ligands (for perovskite nanomaterials), and even structural integrity in polar organic solvents or water.<sup>97–99</sup> Particularly, LHPs even decompose in a moist condition, which really impedes their practical applications.<sup>100</sup> (2) Owing to the low formation energy, LHPs are vulnerable to environmental stress like light, oxygen, heat, etc.<sup>93,101–103</sup> As the color-converter for practical pc-LED devices, they would function on a hot LED chip in ambient air. Environmental stress has become the most harmful factor that affects their performance. Therefore, environmental stability also has nearly become the primary concern for LHPs.<sup>94</sup> (3) The photoluminescence (PL) of all kinds of luminescent materials would be inevitably affected upon heating, especially for LHPs.<sup>98</sup> On the one hand, LHPs would be decomposed directly under exceedingly high temperature.<sup>104,105</sup> On the other hand, thermal stress might accelerate the rates of oxidation and hydration, which amplify the oxygen- and moisture-induced PL quenching. (4) Fast ion-exchange takes place and brings in the severe PL emission shift when two LHPs with varied halide components are mixed.<sup>106–108</sup> For example, the red and green PL shifts to yellow rapidly when green-emitting and red-emitting LHPs are mixed.<sup>109</sup> It is worth noting that the ion-exchange occurs in gas, liquid, and solid phases, which seems to be irresistible.<sup>110–112</sup> All these stability-related shortcomings mentioned above cause serious problems in material synthesis, storage, operation, and device fabrication. PQDs which represent one of the most recent types of LHP materials also suffer from the same problem.<sup>113,114</sup> And not only that, PQDs reunite and lose colloidal stability as well as quantum efficiency under continuous illumination<sup>115</sup> or during purification,<sup>97</sup> which makes their application more challenging.

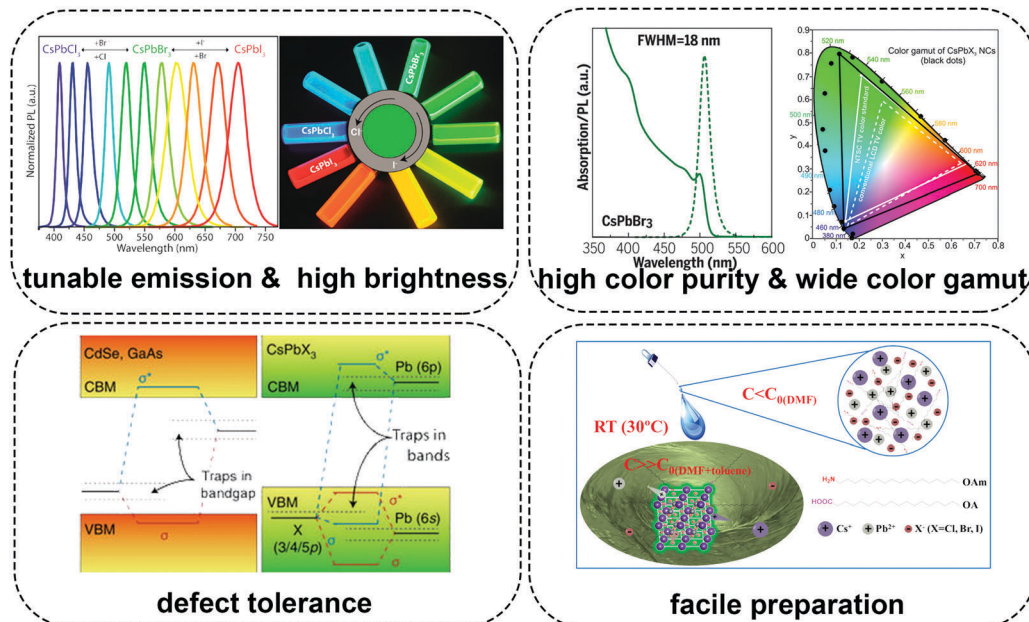


**Fig. 1** Schematic illustration describing the advantages of lead halide perovskite quantum dots in pc-LEDs. Figures in the section of tunable emission & high brightness are reprinted with permission from ref. 78. Copyright 2018, American Chemical Society. Figures in the section of high color purity are reprinted with permission from ref. 72. Copyright 2017, AAAS. Figures in the section of wide color gamut are reprinted with permission from ref. 71. Copyright 2015, American Chemical Society. Figures in the section of defect tolerance are reprinted with permission from ref. 73. Copyright 2018, Springer Nature. Figures in the section of facile preparation are reprinted with permission from ref. 55. Copyright 2016, Wiley-VCH.

Stability is the common issue for all of the perovskite-related fields, and the poor stability limits their broad applications. Recently, the structural<sup>116</sup> and irradiant<sup>96</sup> effects on the optoelectronic properties and stability of perovskites have been reported. Nevertheless, most of the reviews have mainly focused on applications of LHPs in PV technologies.<sup>90,93,94</sup> The ion-diffusion-induced optoelectronic device degradation and the strategies to improve the stability of perovskite films in EL type of LEDs have been reviewed recently.<sup>92</sup> However, the degradation mechanisms for perovskite films in optoelectronic applications and PQDs in photonic applications are different. In this review, the origins of the instability of PQDs such as structural stability, interfacial stability, atmospheric stability (including the effects caused by light, oxygen and moisture), and thermal stability combined with the full understanding of degradation mechanisms under diverse conditions are summarized. Meanwhile, we review the recent studies on enhancing the stability of PQDs. According to the principle, these strategies can be classified into four types: (1) compositional engineering; (2) surface engineering; (3) matrix encapsulation; (4) device encapsulation. Their performance in pc-LEDs is also summarized. At last, based on the inspiring achievements in the issue, some possible solutions to improve the stability of PQDs and the device performance of pc-LEDs are highlighted, and the prospects for applying PQDs in pc-LEDs are presented.

## 2. Origins of the instability of PQDs

### 2.1. Instability derived from the crystal structure

Perovskite is a calcium titanium oxide mineral species consisting of calcium titanate, with the chemical formula  $\text{CaTiO}_3$ .<sup>117</sup>

The discovery of perovskite ( $\text{CaTiO}_3$ ) dates back to 1839 in the Ural Mountains of Russia by Gustav Rose. The mineral is named after the Russian mineralogist L. A. Perovski (1792–1856). Materials with a similar type of crystal structure as  $\text{CaTiO}_3$  are known as perovskites. And any compound denoted by the general chemical formula of  $\text{ABX}_3$  can be described as a perovskite. The previous research centered on compounds consisting of oxygen, tetravalent metal cations (such as  $\text{Ge}^{4+}$ ,  $\text{Ti}^{4+}$ ,  $\text{Zr}^{4+}$ , etc.) and bivalent metal cations (e.g.,  $\text{Ca}^{2+}$ ,  $\text{Sr}^{2+}$ ,  $\text{Ba}^{2+}$ , etc.), which are known as perovskite oxides.<sup>118–120</sup> Recent studies have focused on perovskites composed of halide anions ( $\text{Cl}^-$ ,  $\text{Br}^-$ , or  $\text{I}^-$ ), bivalent metal cations (such as  $\text{Pb}^{2+}$ ,  $\text{Sn}^{2+}$ ,  $\text{Cu}^{2+}$ ,  $\text{Ge}^{2+}$ ,  $\text{Eu}^{2+}$ ,  $\text{Ni}^{2+}$ , etc.), and monovalent inorganic metal cations or organic cations (e.g.,  $\text{Cs}^+$ ,  $\text{Rb}^+$ ,  $\text{CH}_3\text{NH}_3^+$  (methylammonium, MA),  $\text{CH}(\text{NH}_2)_2^+$  (formamidinium, FA), etc.).<sup>40,121–124</sup>

**2.1.1. 3D perovskites.** The structure of LHPs is rather simple and highly symmetric. A typical perovskite structure is shown in Fig. 2A. The Pb ion is located at the center of the cube, and A cations and halide anions occupy the vertexes and face-centers, respectively. The central Pb ion octahedrally coordinates with six X ions in a  $\text{PbX}_6$  configuration. They form a 3D framework perovskite structure through a continuous array of corner-sharing  $\text{PbX}_6$  octahedra. An ideal 3D cubic phase perovskite structure (space group  $Pm\bar{3}m$ ) is shown in Fig. 2B. However, on numerous occasions, perovskites are distorted away from the ideal cubic structure and have become a less symmetrical orthorhombic phase (Fig. 2C) due to the tilting of the  $\text{PbX}_6$  octahedra.<sup>125–127</sup> For instance, even the origin of the perovskite  $\text{CaTiO}_3$  mineral is a pseudo-cubic. The factors leading to tilting of  $\text{PbX}_6$  octahedra can be categorized into five types:<sup>128,129</sup> (1) Jahn-Teller effect induced

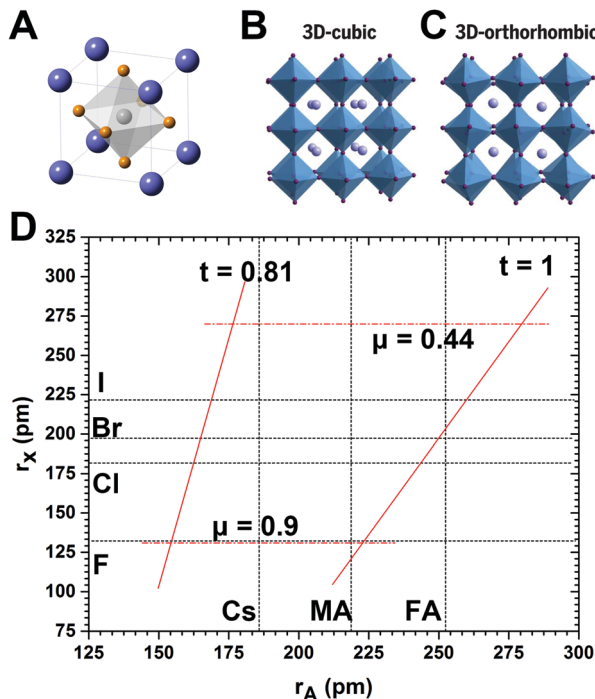


**Fig. 2** (A) Depiction of  $\text{APbX}_3$  perovskites with cubic structure, and crystal structures of lead halide perovskites with (B) cubic and (C) orthorhombic phase. (D) Formability of 3D lead halide perovskites as a function of A-site cation and halide anion radii. The solid and dashed lines mark the bounds of the tolerance and octahedral factors, respectively. (B and C) Reprinted with permission from ref. 72. Copyright 2017, AAAS.

octahedral distortion; (2) off-center displacement effect of the central cations in the octahedra, which might be the foundation of ferroelectricity; (3) small ionic radii A cation filling the interstices of the continuous  $\text{PbX}_6$  octahedral framework; (4) ordering of mixed cations A or B, or vacancies; (5) ordering of mixed anions X, or vacancies. It is clear that a small distortion makes little difference in the electronic properties like bandgap or optical absorption,<sup>130</sup> and the physical properties of perovskites dramatically change following a large octahedral distortion.<sup>116,131</sup> Uncontrollable octahedral distortion leads to difficulty in practical applications. But from the other side, manipulating distortions by ion substitution and other means can be a powerful tool to fine-tune the physical properties of perovskites.<sup>132–134</sup>

The A cations occupy the 12-fold coordinated sites surrounded by eight  $\text{PbX}_6$  octahedra. Therefore, the A cation is limited by the interstices of the 3D  $\text{PbX}_6$  framework. A large A cation cannot be accommodated into the interstice, while a small A cation filling in the interstice leads to collapse of the 3D perovskite structure. For an ideal cubic perovskite structure, A cation that should be accommodated into the framework and the ionic radii have the following geometrical relationship:

$$r_A + r_X = \sqrt{2}(r_B + r_X) \quad (1)$$

where  $r_A$ ,  $r_B$  and  $r_X$  correspond to the radius of the component A, B, and X, respectively. As is well known, a semiempirical geometric parameter, Goldschmidt tolerance factor,  $t$ , can be used to

evaluate the structural stability and distortion of the perovskite structure.<sup>135</sup> The Goldschmidt tolerance factor  $t$  can be described as

$$t = \frac{r_A + r_X}{\sqrt{2}(r_B + r_X)} \quad (2)$$

Although the formula has been proposed for nearly 100 years (in the early 1920s) by Goldschmidt,  $t$  is still widely accepted as a criterion for predicting the formability of 3D perovskite structures.<sup>136</sup> Generally, most perovskites maintain 3D connectivity in the range of approximately  $0.813 \leq t \leq 1.107$ .<sup>137</sup> A recent study shows that the range of  $0.9 \leq t \leq 1$  is generally considered as a good fit for an ideal cubic perovskite structure, implying the likely formation of cubic structures.<sup>138</sup> The range for the tolerance factor  $t$  between 0.71 and 0.9 implies the likelihood of an orthorhombic or rhombohedral structure owing to the distortion of the  $\text{PbX}_6$  octahedra. When the condition cannot be satisfied, the 3D octahedral framework would collapse. In detail, when  $t \geq 1$  or  $t \leq 0.71$ , non-perovskite structures of  $\text{CsNiBr}_3$ -type (1D hexagonal structures formed by the face-sharing of octahedra) or  $\text{NH}_4\text{CdCl}_3$ -type (1D orthorhombic structures formed by the edge-sharing of octahedra) with much large band gaps and poor electroconductivity are formed, respectively.<sup>72,139</sup>

The other semiempirical geometric parameter, octahedral factor,  $\mu$ , can be used to predict the octahedral stability. The octahedral factor  $\mu$  can be described as

$$\mu = r_B/r_X \quad (3)$$

Typically,  $\text{BX}_6$  octahedra are stable in the range between 0.442 and 0.895. As shown in Fig. 2D, the combination of Goldschmidt tolerance factor  $t$  and octahedral factor  $\mu$  provides a parameter space for 3D perovskite formability.<sup>140</sup> It is easy to draw a conclusion that appropriate ionic radii of components are crucial for forming a stable cubic perovskite. Cubic structures of perovskites are usually stable at high temperature, and after cooling down to RT, tetragonal or orthorhombic phases with less symmetry are thermodynamically preferred.<sup>127</sup> MA-based LHPs present the nearly ideal cubic perovskite structure, whereas Cs and FA ions are slightly small or large to perfectly accommodate A-sites.<sup>141</sup> Both  $\text{MAPbCl}_3$  and  $\text{MAPbBr}_3$  have a cubic structure,<sup>142</sup> and  $\text{MAPbI}_3$  perovskites have a tetragonal structure at RT.<sup>103,143</sup> The bulk  $\text{CsPbI}_3$  perovskites have a 3D orthorhombic structure and rapidly transform into the wide-bandgap 1D orthorhombic phase at RT.  $\text{FAPbI}_3$  perovskites have a pseudocubic structure with relatively better stability, but still transform into the wide-bandgap 1D hexagonal phase in several months.<sup>113</sup>  $\text{CsPbBr}_3$  perovskites are widely used in EL and color-conversion type LEDs, and initial research suggested the structure of  $\text{CsPbBr}_3$  nanocrystals (NCs) as cubic,<sup>71</sup> but further studies revealed that both bulk  $\text{CsPbBr}_3$ <sup>144</sup> and  $\text{CsPbBr}_3$  NCs<sup>145</sup> are actually orthorhombic.

Nanoscale perovskite materials are a little different from bulk perovskites. On the one hand, the high specific surface area might accelerate the decomposition.<sup>53</sup> On the other hand, the nanoscale form of perovskites is helpful to stabilize the cubic phase due to the large contribution of surface energy.<sup>146</sup> For instance, bulk  $\text{CsPbI}_3$  with cubic phase is only stable above

305 °C, and it will transform into a 3D orthorhombic phase with a larger band gap gradually and into a nonperovskite 1D orthorhombic structure in the end. CsPbI<sub>3</sub> in nanodimension can maintain the cubic phase for months in ambient air after appropriate treatment.<sup>146</sup> Recently, Pradhan *et al.*<sup>147</sup> demonstrated that the reaction temperature greatly affected the phase-stability of CsPbI<sub>3</sub> PQDs. The CsPbI<sub>3</sub> PQDs obtained below 200 °C usually lost phase-stability. But increasing the reaction temperature up to 260 °C effectively stabilized the CsPbI<sub>3</sub> PQDs, and the cubic to orthorhombic phase transformation can be restricted.

**2.1.2. 2D perovskites.** When long chain amines are introduced into perovskites, the long chain amines will tailor the infinite 3D PbX<sub>6</sub> octahedral network into a 2D structure, which is also named as the Ruddlesden–Popper phase.<sup>148</sup> 2D perovskites exhibit a unique quantum confinement effect owing to the drastic increase of exciton binding energy.<sup>117,149</sup> The 2D perovskites can be described by L<sub>2</sub>[ABX<sub>3</sub>]<sub>n-1</sub>BX<sub>4</sub>, where L represents a long-chain ligand cation and n is the stacking number of perovskite unit cells (corner-sharing PbX<sub>6</sub> octahedra).<sup>150</sup> In general, when the dimensionality of semiconductors decreases to the exciton Bohr radius, the band gap will be larger, which can be named as the quantum confinement effect. Hence, 2D perovskites exhibit strong quantum confinement when the number of stacked layers is below three, due to the lattice constant of the LHP unit cell of about 0.6 nm, combined with the exciton Bohr radius of about 1.4–2.0 nm.<sup>151</sup> The thickness-dependent PL emission is depicted in Fig. 3A. The PL tunability *via* controlling the stacking layer is helpful for a huge number of applications, compared with the weak quantum confinement of bulk perovskites.<sup>152–154</sup>

The Ruddlesden–Popper phase perovskites have better environmental stability than their 3D analogues, which is attributed to the relatively strong van der Waals interactions among long chain organic molecules resulting in an increased formation energy (Fig. 3B). Density functional theory (DFT) based calculations revealed that the energy of desorbing phenylethyl-ammonium iodide (PEAI) from the perovskite is 0.36 eV higher than that for methylammonium iodide (MAI). Hence, the PEAI<sub>2</sub>PbI<sub>4</sub> films show 1000 times slower decomposition than MAPbI<sub>3</sub> films in ambient conditions.<sup>155</sup>

The long chain amines also result in poor electronic properties compared with 3D analogues.<sup>156</sup> And the poor electronic properties of 2D perovskites impede their applications in solar cells and EL devices. Indeed, (quasi) 2D perovskites based solar cells suffer from a low PCE.<sup>157,158</sup> However, the 2D–3D perovskite compounds fabricated by integrating an appropriate amount of long chain amines into 3D perovskite frameworks present high charge injection efficiency as well as high stability.<sup>159–165</sup> Recently, a significant amount of effort has been devoted to 2D perovskites owing to their attractive characteristics, which are beneficial to develop high performance optoelectronic devices.<sup>166–174</sup>

## 2.2. Interface-induced instability

LHPs are ionic compounds, and their interactions with surface ligands also present ionic characteristics. Rhee<sup>97</sup> *et al.* firstly elaborated the dynamical surface of CsPbBr<sub>3</sub> PQDs by <sup>1</sup>H

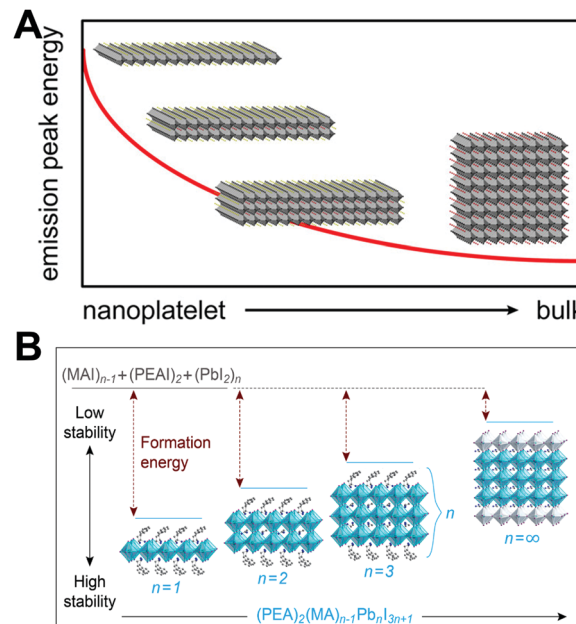


Fig. 3 (A) Representation of the nanplatelet thickness-dependent emission peak energy, where  $n = \infty$  represents the 3D phase LHPs. Reprinted with permission from ref. 154. Copyright 2017, American Chemical Society. (B) Formation energies of (PEA)<sub>2</sub>(MA)<sub>n-1</sub>Pb<sub>n</sub>I<sub>3n+1</sub> perovskites with different  $n$  values: the higher formation energy implies better stability. Reprinted with permission from ref. 155. Copyright 2016, American Chemical Society.

solution nuclear magnetic resonance (NMR) spectroscopy. Briefly, surface ligands, oleic acid (OA) and oleylamine (OLA), are not tightly bound to the surface of CsPbBr<sub>3</sub> PQDs. The dynamic surface is stabilized by oleylammonium bromide when OA as the only ligand for CsPbBr<sub>3</sub> PQDs. While protonated OLA draws OA into the ligand shell, the dynamic surface is stabilized by oleylammonium bromide, oleylammonium oleate and OLA (Fig. 4A). The diffusion coefficient  $D$  was measured to further investigate the dynamic surface *via* Diffusion Ordered NMR Spectroscopy (DOSY). The parameter  $D$  is defined as

$$D = \frac{k_B T}{f} \quad (4)$$

where  $f$ ,  $k_B$  and  $T$  correspond to the friction coefficient, the Boltzmann constant and the absolute temperature, respectively. The value of  $D$  for oleylammonium bromide in the absence of CsPbBr<sub>3</sub> PQDs and in the PQD suspension was measured to be 361 and  $166 \pm 18 \mu\text{m}^2 \text{s}^{-1}$ , respectively. The smaller  $D$  indicates that the surface ligands are not tightly bound to the surface but undergo fast exchange between the bound and free state. Such highly dynamic surface brings in a fast anion exchange reaction during device fabrication, which leads to difficulty in the application of highly luminescent PQDs in pc-LEDs (Fig. 4B).<sup>107,109</sup> However, the anion exchange reaction facilitates tunable fluorescence covering the entire visible spectral region by postsynthetic chemical transformations (Fig. 4C).<sup>106,110,112</sup> Owing to the defect-tolerant characteristics of LHPs, most of their optical properties such as bright PL and narrow emission line widths

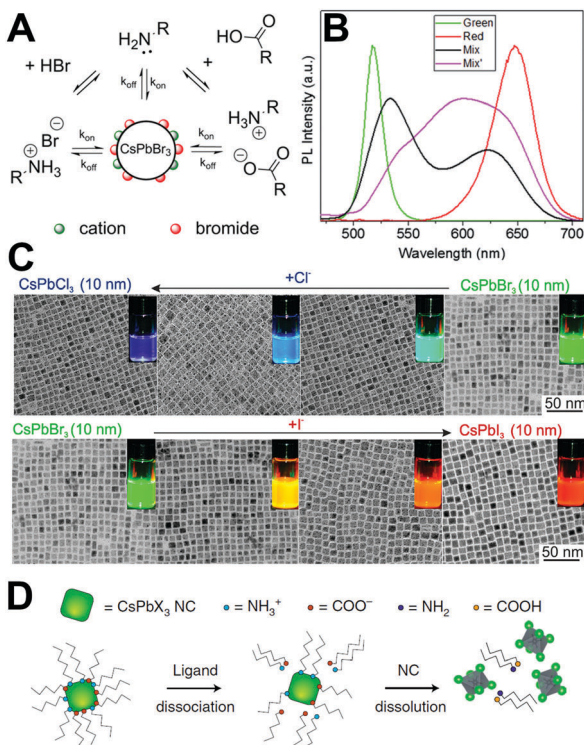


Fig. 4 (A) Schematic representation of the dynamic surface of  $\text{CsPbBr}_3$  PQDs. Reprinted with permission from ref. 97. Copyright 2016, American Chemical Society. (B) PL spectra of green and red emissive PQDs mixed in the silicone resin. Reprinted with permission from ref. 107. Copyright 2016, The Royal Society of Chemistry. (C) Tuning the optical properties by treatment with various quantities of chloride or iodide anions. The figures show the evolution of TEM images and emission colors (under a UV lamp,  $\lambda = 365 \text{ nm}$ ) upon forming mixed-halide  $\text{CsPb}(\text{Br}/\text{Cl})_3$  and  $\text{CsPb}(\text{Br}/\text{I})_3$  to fully exchanged  $\text{CsPbCl}_3$  and  $\text{CsPbI}_3$ . Reprinted with permission from ref. 106. Copyright 2015, American Chemical Society. (D) Schematic illustration that PQDs often lose their colloidal stability, or even structural integrity, due to the desorption of weakly bound ligands. Reprinted with permission from ref. 73. Copyright 2018, Springer Nature.

can be retained after anion exchange.<sup>110</sup> It is necessary to block the ion exchange between varied PQDs in pc-LED applications. Moreover, due to the unstable interface of PQDs, their ligands are easily lost during purification. Especially, when polar solvents are added to isolate the nanocrystals, the  $\text{CsPbX}_3$  PQDs often lose their optical property, colloidal stability and sometimes even structural integrity (Fig. 4D).

### 2.3. Environmental stability

It is widely known that the LHPs suffer from rapid degradation when they are exposed to ambient air. Even when being carefully encapsulated in a resin sealant, perovskite materials are still sensitive to residual oxygen and moisture.<sup>175</sup> An unconventional thorough encapsulation of the device is difficult and costly. Encapsulating them in an inert condition might help to prevent or mitigate degradation. However, as outdoor pc-LED devices, they must function under real-world atmospheric conditions and on a hot LED chip. Therefore, the environmental stability of LHPs has become the prior concern. Gaining insight into the

degradation mechanisms including the degradation due to the effect of light, oxygen, and moisture on the material is crucial for the rational design of stable perovskite composites and for enhancing the duration of perovskite pc-LEDs.

**2.3.1. Light-induced decomposition.** Continuous illumination affects the performance and the long-term stability of devices.<sup>96,176–178</sup> Moreover, as the color conversion layer, PQDs convert blue/UV light into other visible light. In other words, PQDs are long-term exposed to blue/UV irradiation when they are working. Therefore, the understanding of variation of perovskites upon illumination is essential for improving the performance and lifetime of pc-LEDs.

The light soaking effect is a common phenomenon and has attracted wide attention in PV technologies.<sup>179,180</sup> Perovskites as the light-absorbing layer or light-emitting layer also present the light soaking effect.<sup>181–183</sup> In the solar cells, the light soaking effect is associated with ion migration.<sup>184</sup> In the light-emitting aspects, Scheblykin *et al.*<sup>185</sup> found that the PL intensity as well as lifetime would be increased upon light irradiation in surface-deposited  $\text{MAPbI}_3$ . The light-induced PL brightening is reversible enabled by switching off of the excitation light. It is interesting that the PL brightening was more pronounced in oxygen in contrast to nitrogen or vacuum, and a negligible difference was observed in ambient air or in pure oxygen conditions (Fig. 5A).

To further investigate the enhancement of both PL lifetime and intensity upon light irradiation, confocal fluorescence microscopy and time-of-flight secondary ion-mass spectrometry

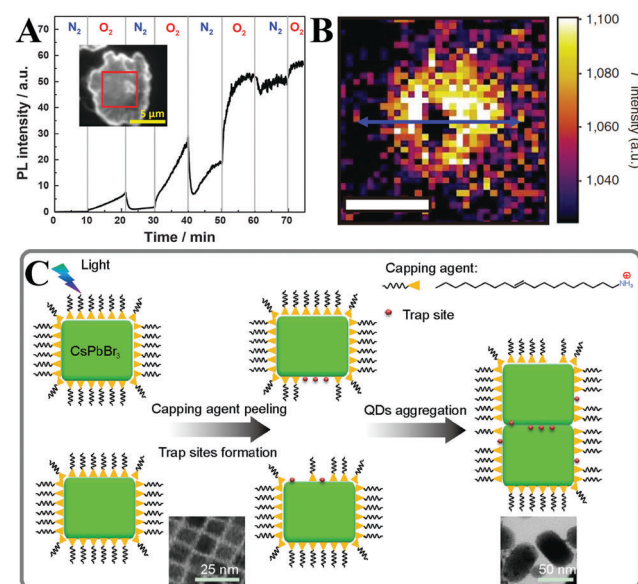


Fig. 5 (A) The atmosphere effect on the PL enhancement of  $\text{MAPbI}_3$ . The inset shows the micrograph of the sample and the selected region (red square) taken for the analysis. Reprinted with permission from ref. 185. Copyright 2015, The Royal Society of Chemistry. (B) ToF-SIMS image of the iodide ( $\text{I}^-$ ) distribution summed through the film depth, and the scale bar is 10 nm. Reprinted with permission from ref. 186. Copyright 2016, Springer Nature. (C) Schematic picture of the light-induced agglomeration of  $\text{CsPbBr}_3$  PQDs. The insets show the light-induced morphological evolution of  $\text{CsPbBr}_3$  PQDs. Reprinted with permission from ref. 189. Copyright 2016, Springer Nature.

(ToF-SIMS) were carried out by Stranks *et al.*<sup>186</sup> According to the ToF-SIMS image of the iodide distribution mapping and line scan, the regions irradiated by the laser show depleted levels of iodide (lower than the background iodide levels), whereas the adjacent regions show iodide-rich levels compared with the background iodide levels (Fig. 5B). The mechanisms of light-induced iodide redistribution resulting in PL brightening are proposed as follows: (1) before illumination, the trap density is high owing to the excess of iodide; (2) upon light irradiation, photo-generated electrons will fill the traps, which induces an electric field in  $\text{MAPbI}_3$  films. The electric field results in iodide migration from the irradiated region to the adjacent iodide vacancies; (3) under continuous illumination, the system attains a stabilized iodide concentration between the illuminated region and the adjacent dark spot. The PL emission reaches a steady level with orders of magnitude reduced trap density; (4) after removing the irradiation sources, some iodide ions are driven back from the dark region to the brightened region by concentration gradients. A similar phenomenon was also observed in  $\text{MAPbI}_{3-x}\text{Br}_x$  films.<sup>187</sup>

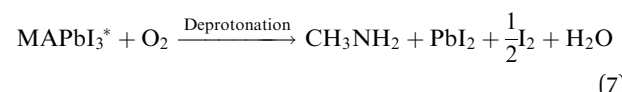
As for the perovskite nanomaterials, the PL intensity enhancement of  $\text{MAPbBr}_3$ <sup>188</sup> and  $\text{CsPbBr}_3$ <sup>77,115</sup> PQDs was monitored by using a fluorescence spectrophotometer. Noticeably, such PL enhancement was only observed at the beginning of illumination by a precious *in situ* test, while the fluorescence intensity would decrease along with the prolonged illumination time even in a dry nitrogen atmosphere.<sup>115</sup> Zheng *et al.* proposed a model (Fig. 5C) for light-induced regrowth based on the morphology evolution.<sup>189</sup> After long-term light irradiation, the photo-generated carriers diffused to the surface of  $\text{CsPbBr}_3$  PQDs and were captured by ionic surface ligands. Some of the surface ligands diffused to the solvent. At the same time, the ligands in free state bound to the surface leading to aggregation of adjacent PQDs. As can be seen from the TEM images (inset of Fig. 5C), the  $\text{CsPbBr}_3$  PQDs with an incipient cubic shape aggregated into larger nanocrystals. The aggregation process brought in the increased trap states owing to the removal of the capping agent, leading to inferior optical performance.

**2.3.2. Oxygen-induced decomposition.** It has been widely accepted that the ground state LHPs are long-term stable in oxygen atmospheres. For example, Park and coworkers<sup>190</sup> demonstrated that the performance of unsealed solar cells fabricated from  $\text{MAPbI}_3$  films as light-harvesting layers did not change after being stored in dry air in the dark for more than 500 h. Similarly, a negligible difference in the optical property of  $\text{CsPbBr}_3$  PQDs was observed in an oxygen or nitrogen atmosphere in the dark.<sup>115</sup>

Not only the inoxidizability of ground state LHPs, but also the PL was enhanced upon exposure to oxygen atmospheres, which has received extensive attention. Such “oxygen-boost” effect has also been found in traditional CdSe/CdS quantum dots<sup>191</sup> and CdSe nanoplates.<sup>192</sup> A full understanding of oxygen-induced PL brightening is helpful for optimizing the device performance and enhancing the short-term stability. A DFT modeling was conducted to reveal that oxygen molecules deactivated the interstitial iodide deep traps by forming moderately

stable oxidized products in  $\text{MAPbI}_3$ . The  $\text{MAPbI}_3$  forms emissive sub-band gap states upon illumination in an inert atmosphere, whereas the oxygen molecules (even in a small amount) could attenuate the trap density.<sup>193</sup> Brovelli and coworkers<sup>194</sup> carried out a spectro-electrochemical (SEC) experiment to investigate the selective carrier trapping and the influence of environmental oxygen on exciton recombination dynamics in  $\text{CsPbBr}_3$  PQDs. It was revealed that the photo-generated holes are captured by trapping states, which leads to severe PL quenching, whereas electron traps are nearly inconsequential to nonradiative decay. Therefore, suppression of hole traps results in brighter PL emission under oxidizing conditions.

In spite of the inoxidizability of ground state LHPs and the temporal “oxygen-boost” effects, the long-term oxidizability is completely different upon continuous light irradiation.<sup>195</sup> The LHPs with photo-generated carriers are susceptible to oxygen molecules.<sup>196</sup> The probable processes of photo-oxidation are as follows (Fig. 6):<sup>197</sup> (1) oxygen molecules diffusing into the lattice and filling the vacancy; (2) photo-generated electrons in the conduction band (CB) and holes in the valence band (VB); (3) superoxide compound ( $\text{O}_2^-$ ) formation from oxygen and  $\text{CH}_3\text{NH}_3\text{PbI}_3$ ; (4) decomposition to  $\text{PbI}_2$ ,  $\text{H}_2\text{O}$ ,  $\text{I}_2$  and  $\text{CH}_3\text{NH}_2$ . The proposed photo-oxidation reactions are



The presence of decomposition products was verified by X-ray diffraction (XRD) and gas chromatography (GC), confirming the reliability of the photo-oxidation mechanism. As for the all-inorganic perovskites, A-sites composed of inorganic ions such as  $\text{Cs}^+$  and  $\text{Rb}^+$  show better chemical stability in comparison to the volatile organic component  $\text{CH}_3\text{NH}_3\text{I}$ . But unlike the specific photo-oxidation mechanism of hybrid  $\text{MAPbI}_3$ , the process of photo-oxidation forming photo-active  $\text{CsPbX}_3^*$  and its reaction with oxygen molecules to form the final products is still ambiguous,

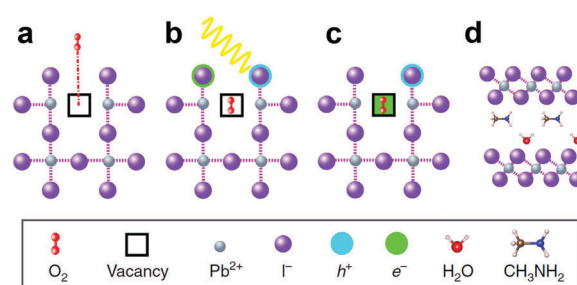


Fig. 6 Schematic representation of the oxygen-induced decomposition. (a) Oxygen diffusion and incorporation into the lattice, (b) photoexcitation of  $\text{CH}_3\text{NH}_3\text{PbI}_3$  to create electrons and holes (c) superoxide formation from  $\text{O}_2$ , and (d) reaction and degradation to  $\text{PbI}_2$ ,  $\text{H}_2\text{O}$ ,  $\text{I}_2$  and  $\text{CH}_3\text{NH}_2$ . Reprinted with permission from ref. 197. Copyright 2016, Springer Nature.

except that some PbO was detected by the X-ray photoelectron spectroscopy (XPS) technique after photo-oxidation.<sup>115</sup>

Li *et al.*<sup>115</sup> have systematically investigated CsPbBr<sub>3</sub> PQDs' photo-oxidation processes according to their morphology, structure, and PL evolutions. Their outstanding optical property can be retained in the first hour of illumination when they are encapsulated in a dry nitrogen atmosphere, whereas an apparent decay of PL intensity was observed upon continuous 450 nm pump illumination. The oxygen-induced fluorescence quenching can be divided into two categories. On the one hand, oxygen accelerates PQDs' agglomeration and regrowth into large crystals with low PL QYs. On the other hand, oxygen molecules etch surface unstable nuclei, which leads to high density of surface defects.

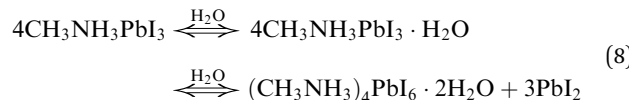
Despite the disadvantage of photo-oxidation, this process is not as severe as we imagine. When they are incorporated in the full solar cell devices, most of the free electrons will be transferred from the CB to the electron acceptors and the free electron density is much lower than in the neat LHPs.<sup>198</sup> When they are incorporated in the pc-LEDs, most excitons combined rapidly due to the direct bandgap in LHPs, the short PL lifetimes, and the high exciton binding energy, which means that the electron rich surface defects are less abundant.<sup>199</sup> Experimentally, the device performance did decrease upon continuous light irradiation.<sup>115,189</sup> But it is clear that photo-oxidation is not the predominant issue, the light-induced agglomeration of PQDs may be more serious in decreasing the performance of pc-LEDs. Therefore, it may be more effective to disperse PQDs preventing their agglomeration than constructing a prohibitively expensive oxygen barrier for improving the device lifetime of pc-LED devices.

**2.3.3. Moisture-induced decomposition.** Another widely recognized stability issue for LHPs is their easy degradation in water and even in moisture conditions owing to their ionic nature.<sup>1,200,201</sup> The instinct vulnerability to water severely impedes their applications and decreases the device performances. Even worse, oxygen-induced decomposition only happens upon illumination, whereas moisture-induced decomposition occurs even in the dark. This common phenomenon has received worldwide attention, and a great number of works have been devoted to elucidating the moisture-induced decomposition mechanism and preventing the decomposition.

Before the detailed decomposition mechanism is given, the material synthesis and device fabrication benefited from the water-assisted process should be discussed. The water-assisted resolvation and recrystallization of LHPs have been demonstrated to be a useful strategy for solar cell fabrication.<sup>202–204</sup> Yang *et al.*<sup>205</sup> systematically investigated the crystallinity, morphology, and carrier lifetime of MAPbBr<sub>3</sub> films affected by postmoisture treatment. The maximum current efficiency of PeLEDs showed near 20-fold enhancement following the optimized postmoisture treatment in comparison with pristine MAPbBr<sub>3</sub> films. Yin and coworkers<sup>206</sup> developed a novel strategy for preparing highly luminescent CsPbX<sub>3</sub> PQDs from non-emissive Cs<sub>4</sub>PbX<sub>6</sub> nanocrystals through water-extraction of CsX. Additionally, the obtained CsPbX<sub>3</sub> PQDs followed by the water-triggered transformation showed enhanced stability

against moisture. Sahin *et al.*<sup>207</sup> synthesized CsPbBr<sub>3</sub> bundles utilizing the water-driven structural transition of CsPbBr<sub>3</sub> nanowires (NWs). And such large bundles present better environmental stability. Rogach and coworkers<sup>208</sup> synthesized shape-controlled and stable CsPbBr<sub>3</sub> nanocrystals by introducing moderate levels of water into the reaction precursor. The crystallization environment was strongly affected by the additive water, which led to the formation of perovskite nanocrystals with varied morphology. Xu *et al.*<sup>209</sup> firstly synthesized fluorescent MAPbX<sub>3</sub> (X = Cl, Br) PQDs in an aqueous solution. The obtained PQDs were stable in ambient conditions and even in polar solvents, which was ascribed to the positively charged surface state of the PQDs and the proper synthetic ionic environment. Kim *et al.*<sup>210</sup> reported a facile aqueous synthesis of rod-shaped luminescent APbX<sub>3</sub> (A = Cs, MA) in acidic or basic media. Some Pb(OH)<sub>2</sub> by-products formed on the surface of perovskites as confirmed by TEM and XRD measurements. Hence, the PL of non-ligand capped APbX<sub>3</sub> nanorods can be retained even when being immersed in water over six months.

Benefited from the tremendous progress made in solar cells based on tri-iodide perovskites, the moisture-induced MAPbI<sub>3</sub> decomposition mechanism has been elucidated by the experimental and theoretical study, which is given below:<sup>211</sup>



Only a small amount of the monohydrate phase primarily formed in the presence of moisture as confirmed by ellipsometry and XRD studies. The formation of the monohydrate compound has been proven to be reversible when placed in the dry conditions. Next, the dihydrate compound formed along with the hydration process (Fig. 7A). The phase separation caused by the formation of PbI<sub>2</sub> results in accelerated hydration. The MA<sup>+</sup> cations are not tightly bonded to the I<sup>-</sup> but interact with water in the dihydrate phase. Thereby, the dihydrate compounds are more likely to decompose into methylammonia (CH<sub>3</sub>NH<sub>2</sub>), HI, and PbI<sub>2</sub>. Walsh *et al.*<sup>212</sup> proposed the decomposition pathway in the presence of water, as shown in Fig. 7B. Both CH<sub>3</sub>NH<sub>2</sub> and HI byproducts are volatile and soluble in water. This pathway results in the formation of a PbI<sub>2</sub> solid, which is in good agreement with the experimental observations.

As for the all-inorganic perovskite, the pathways for moisture-induced degradation are not well-defined. But it is clear that the moisture-induced resolvation and recrystallization produce large crystal grains.<sup>115</sup> Such large crystals might be beneficial to PV technologies but harmful to pc-LEDs because of loss of PL QYs.

The moisture-induced decomposition of perovskite materials results in a severe decline in device performance. And this process would be accelerated upon light irradiation by surface reconstruction.<sup>213,214</sup> Functionalization of water-resisting layers can improve the humidity tolerance of perovskite films as well as passivate the surface defects, which is widely used in the PV and EL technologies.<sup>100,215</sup> The situation is almost completely different for PQDs applied in pc-LEDs. The PQDs synthesized through the typical hot-injection method or the ligand-assisted

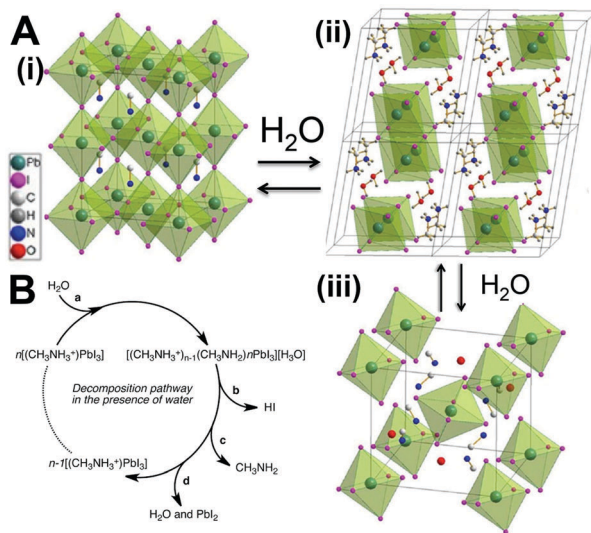
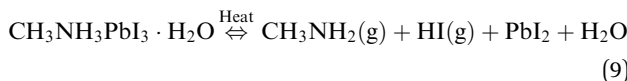


Fig. 7 (A) The two hydrated structures of the MAPbI<sub>3</sub> perovskite and the structural evolutions. Reprinted with permission from ref. 211. Copyright 2015, Wiley-VCH. (B) Possible decomposition pathway of MAPbI<sub>3</sub> in the presence of water. Reprinted with permission from ref. 212. Copyright 2014, American Chemical Society.

reprecipitation (LARP) technique were capped by long-chain OA and OLA (for all-inorganic perovskites) or octylamine (for organic-inorganic hydride perovskites) molecules. In comparison with the bare perovskite films requiring extra passivation by hydrophobic ammonium cations, named the water-resisting layers, the OA molecules with longer carbon chains are more hydrophobic.

#### 2.4. Thermal stability

Thermal degradation at high temperature is the most vital issue with respect to thermal stability. Thermogravimetric analysis (TGA) studies on hybrid LHPs show that the mass loss has two steps. The sublimation of HX and CH<sub>3</sub>NH<sub>2</sub> is around 220 °C for MAPbBr<sub>3</sub><sup>105</sup> and 250 °C for MAPbI<sub>3</sub>.<sup>216</sup> The second step begins at >500 °C owing to the sublimation of the PbX<sub>6</sub> octahedra. This is consistent with the all-inorganic CsPbX<sub>3</sub> that decomposes at >500 °C owing to the collapse of crystal structures.<sup>105</sup> All the results suggest the high thermal stability of both organic-inorganic hybrid and all-inorganic perovskites. However, the oxygen- and moisture-induced decomposition would be accelerated and amplified at high temperature, and the combination of moisture and heat would lead to a more rapid decomposition.<sup>214</sup> Moreover, for the reversible hydration/dehydration reaction, the monohydrate compounds easily decompose according to the following reaction:<sup>94,214</sup>



The formation of volatile HI and CH<sub>3</sub>NH<sub>2</sub> leads to phase separation, which drastically accelerates the hydration.

Besides the decomposition under thermal stress severely affecting the PL property of LHPs, the thermal-induced PL quenching is universal and inevitable for all types of luminescent materials. Even the PL of commercial phosphor K<sub>2</sub>SiF<sub>6</sub>·Mn<sup>4+</sup>

suffers from thermal quenching of ~25% upon heating from 293 to 453 K.<sup>217</sup> Additionally, the core-only traditional CdSe quantum dots (QDs) show about 80% PL loss upon heating from 293 to 400 K.<sup>218</sup> The optical property and stability can be enhanced by inorganic shell coating. Actually, the PL intensity of commercial CdSe/CdS/ZnS QDs still shows a decrease of about 30% of the initial value when heating from 293 to 373 K.<sup>218</sup> The bulk MAPbBr<sub>3</sub> perovskite shows severe PL quenching (nearly 100%) from 300 to 400 K, while the MAPbBr<sub>3</sub> PQDs preserve an intensity of 30% in the same temperature range according to temperature dependent PL measurements.<sup>56</sup> The neat CsPbBr<sub>3</sub> PQDs prepared by the LARP technique show about 85% PL loss from 80 to 273 K,<sup>55</sup> and another 80% (obtained from a similar protocol) from RT to 373 K.<sup>219</sup> It should be noted that the thermal-induced PL quenching might dominantly arise from the agglomeration of PQDs. Schaller *et al.*<sup>220</sup> have systematically studied the temperature dependent fluorescence of CsPbBr<sub>3</sub> PQDs by embedding the CsPbBr<sub>3</sub> PQDs in a polymer matrix to minimize the aggregation-induced PL quenching. After diminishing the interactions of CsPbBr<sub>3</sub> PQDs, the CsPbBr<sub>3</sub>-polymer composites show fluorescence loss of less than 10% when heating from 80 to 273 K, whereas the PL of neat CsPbBr<sub>3</sub> PQDs reduced over 85% in the same condition. They proposed that the PL quenching of CsPbBr<sub>3</sub>-polymer composites corresponds to thermally activated halogen vacancies, supported by time-resolved and transient absorption (TA) measurements as well as DFT calculations. According to thermal cycling measurements (Fig. 8), the PL quenching of CsPbBr<sub>3</sub> PQDs is largely reversible below 450 K. On the other hand, when CsPbBr<sub>3</sub> PQDs are heated at higher temperature, they exhibit irreversible quenching. The irreversible loss is likely associated with the desorption and decomposition of organic ligands above 450 K. A similar PL resilience was also observed in the MAPbBr<sub>3</sub> PQDs embedded in polymer hosts.<sup>75</sup>

The reversible PL allows for device encapsulation at a relatively high temperature. It is easily seen that the PL persistence of PQDs at high temperatures is close to that of the core-only CdSe QDs, and the device performance may be affected at high operating temperatures. Some thermal barriers or appropriate heat sinks are highly expected for perovskite pc-LEDs at this stage. Maybe an inorganic shell protecting like a CdSe/CdS/ZnS core/shell structure holds great promise in further improving the thermal stability of PQDs.

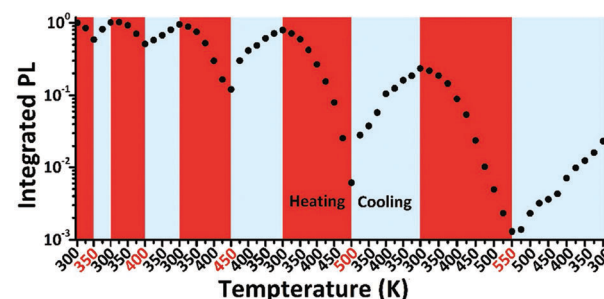


Fig. 8 Thermal cycling measurements of CsPbBr<sub>3</sub> PL. Reprinted with permission from ref. 220. Copyright 2017, Wiley-VCH.

As discussed above, light, oxygen, moisture, and heat, and their synergistic effects affect the stability of PQDs. Both photo-oxidation and moisture-induced decomposition take up a little proportion of the total perovskite materials in normal conditions. The chemical stability of PQDs is much higher than we imagine. But it does not mean that the encapsulations are no more necessary for PQDs. On the contrary, PQDs grow into large crystal grains with low PL QYs under moisture conditions and light irradiation. And such crystal-regrowth can be accelerated in the presence of oxygen. The formation of large perovskite crystals is the primary culprit for PL quenching rather than the material decomposition in normal conditions. Thermal-induced PL quenching also brings great difficulties in applying them for pc-LEDs. Although PQDs show high PL resilience, most PL quenched on the hot LED chip owing to their intrinsic poor PL thermal resistance. Additionally, it is well known that a chemical reaction can be accelerated at a higher temperature. The decomposition and crystal-regrowth can be accelerated at higher temperatures, which results in amplified PL quenching. Hence, designing thermally stable perovskite materials and better encapsulation to eliminate their agglomeration and regrowth are highly desired for pc-LED application.

### 3. Strategies toward improving the stability of PQDs

A great effort has been devoted to stabilize PQDs. Within several years, numerous strategies have been developed. Herein, we review the recent studies on enhancing the stability of PQDs (Fig. 9).

It is worth noting that we mainly summarize the strategies for improving the stability of PQDs. Some of the methods used to stabilize perovskite films or perovskite crystal grains might be effective to improve the stability of PQDs, which are also included in this section.

#### 3.1. Compositional engineering

**3.1.1. A-Site doping.** Doping is an effective tool that not only affects junction formation but also improves the transport properties for semiconductors.<sup>221,222</sup> An appropriate doping contributes to enhancing the stability of perovskites. For example, the stability can be enhanced by replacement of  $\text{MA}^+$  by  $\text{FA}^+$  or thermally stable  $\text{Cs}^+$  cations even by partial substitution.<sup>116,146,223,224</sup> In detail, the  $\text{FA}^+$  cations with a larger ionic radius (2.79 Å; 2.70 and 1.81 Å for  $\text{MA}^+$  and  $\text{Cs}^+$  cations, respectively) in the interstice of the  $\text{PbBr}_6$  octahedral 3D framework affect the Pb–Br–Pb bond causing deviation from their ideal angles up by 15° by the chemical pressure. Such chemical pressure results in the tilting of the  $\text{PbBr}_6$  octahedra and the enlargement of the space filling density, which might be the origin of the better stability of the FA-based perovskite structure.<sup>224</sup>  $\text{FAPbBr}_3$  in the form of quantum dots also presents a higher stability than  $\text{MAPbBr}_3$  PQDs.  $\text{FAPbBr}_3$  PQDs maintain their high PL QYs after 3 times purification by using acetonitrile/toluene mixed solvents, while  $\text{MAPbBr}_3$  PQDs quickly decompose following the same treatment.<sup>224</sup>

All inorganic  $\text{CsPbBr}_3$  shows much higher thermal stability which could effectively suppress decomposition caused by the heat of LED chips, and its environmental stability is also superior to the hybrid perovskites.<sup>105</sup> Due to the high chemical stability and high PL brightness (PL QYs up to 90% in solution)

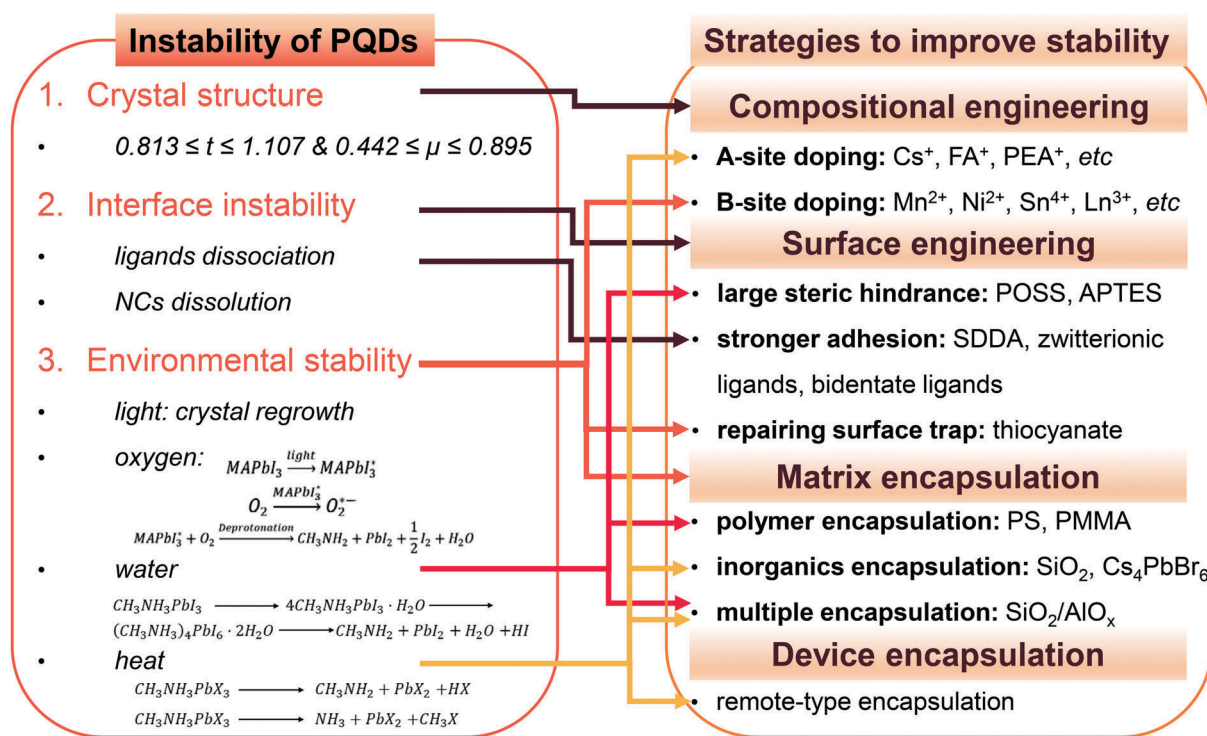


Fig. 9 Schematic diagram summarizing the representative instability of PQDs and the corresponding solutions.

of  $\text{CsPbBr}_3$  PQDs, employing  $\text{CsPbBr}_3$  as a color converter in pc-LEDs has attracted great interest.

The red-emitting lead iodide perovskites are thermodynamically unstable compared with their bromide analogues.  $\text{FAPbI}_3$ <sup>4</sup> and  $\text{CsPbI}_3$ <sup>71</sup> with 3D perovskite structure crystallize into 1D hexagonal and 1D orthorhombic structures, respectively, because the  $\text{FA}^+$  ions are too large and the  $\text{Cs}^+$  ions are too small for 3D polymorphs.  $\text{MAPbI}_3$  PQDs with suitable ionic radii suffer from a rapid PL loss due to the poor chemical stability.<sup>104</sup> This challenge which is faced when preparing stable red and near-infrared (NIR) nanoemitters, termed the “perovskite red wall”, could be addressed by a rational doping of  $\text{FA}^+$  into the  $\text{CsPbI}_3$  lattice.<sup>225</sup> The as-designed  $\text{FA}_{0.1}\text{Cs}_{0.9}\text{PbI}_3$  PQDs show stable and bright red-emission with PL QYs over 70% because of the compensating inadaptable anion (Fig. 10A). Similarly, PeLEDs fabricated from the mixed cation  $\text{FA}_{0.8}\text{Cs}_{0.2}\text{PbBr}_3$  PQDs present significant enhancement of device performance that is most likely associated with the entropic stabilization.<sup>226</sup> Etgar *et al.*<sup>227</sup> synthesized  $\text{Rb}_x\text{Cs}_{1-x}\text{PbX}_3$  PQDs with tunable fluorescence and high PLQEs up to 60%.  $\text{Rb}_x\text{Cs}_{1-x}\text{PbX}_3$  PQDs retain the structural integrity and show a slight difference upon doping  $\text{Rb}^+$  cations into the lattice. A further stability test revealed that the mixed Rb/Cs bromide PQDs present a slight red-shift in absorption over months, but the chloride analogues show limited stability.

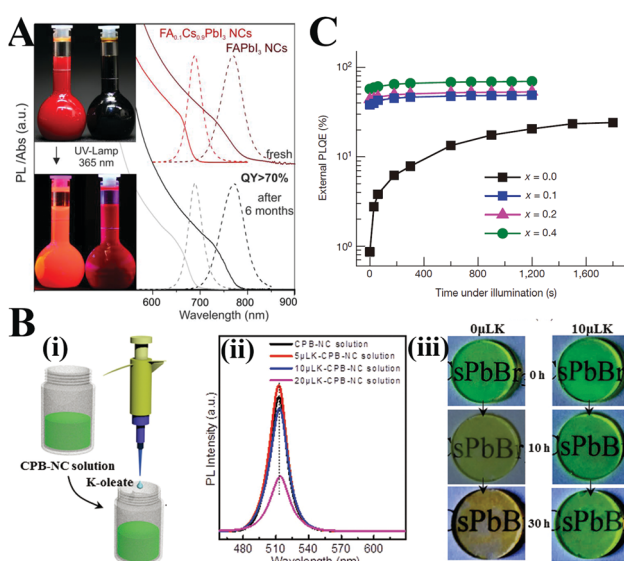


Fig. 10 (A) Optical absorption and PL spectra of  $\text{FAPbI}_3$  and  $\text{FA}_{0.1}\text{Cs}_{0.9}\text{PbI}_3$  PQDs before and after 6 months of storage. The insets are photographs of the  $\text{FAPbI}_3$  and  $\text{FA}_{0.1}\text{Cs}_{0.9}\text{PbI}_3$  PQDs’ colloidal solutions under daylight (upper image) and under UV lamp ( $\lambda = 365 \text{ nm}$ ; lower image) excitation. Reprinted with permission from ref. 225. Copyright 2017, American Chemical Society. (B)  $\text{K}_x\text{Cs}_{1-x}\text{PbBr}_3$ : (i) schematic of the addition of the K-oleate precursor into the as-prepared  $\text{CsPbBr}_3$  toluene solutions. (ii) PL emission spectra of the  $\text{CsPbBr}_3$  and K-modified  $\text{CsPbBr}_3$  PQDs. (iii) Optical images of the  $\text{CsPbBr}_3$  and K-modified  $\text{CsPbBr}_3$  PQD films as a function of the treatment time in the dark environment ( $50^\circ\text{C}$ , relative humidity 60%). Reprinted with permission from ref. 228. Copyright 2018, Wiley-VCH. (C) PLQE time course of perovskites illustrating that the K-doped perovskites are stable to light exposure. Reprinted with permission from ref. 230. Copyright 2018, Springer Nature.

Incorporation of  $\text{K}^+$  into  $\text{CsPbBr}_3$  PQDs by the postmodification method improves PL QYs from 65% to 83% (Fig. 10B).<sup>228</sup> Similarly, the incorporation of  $\text{K}^+$  into  $\text{CsPbCl}_3$  PQDs brings in the improvement of PL QYs from 3.2% to 10.3%.<sup>229</sup> Moreover, the introduction of  $\text{K}^+$  greatly enhanced the photostability and environmental stability. Especially, the deposited films composed of  $\text{K}_x\text{Cs}_{1-x}\text{PbBr}_3$  PQDs maintain the initial brightness even after 153 h irradiation, whereas the PL intensity of pristine PQD films decreases to half of the initial value after 45 h. The incorporation of  $\text{K}^+$  leads to a K-rich phase at the interface, which is also demonstrated to be useful in the film applications. The “photobrightening” phenomenon caused by halide migration has been discussed before. Surprisingly, the PL intensity of K-incorporated perovskite films is found to be stable to light exposure (Fig. 10C). The K-rich phase effectively inhibited the halide migration and suppressed the non-radiative decay.<sup>230</sup> Multi A sites such as RbCsMAFA co-doping results in a high entropy system, which has been considered as an effective way to improve the device lifetime in the film applications.<sup>134,231</sup> Nevertheless, the high entropy PQDs are rarely prepared and investigated, which might be attributed to self-purification effects of quantum dots.<sup>232</sup>

2D perovskites developed by introducing long chain amines such as oleylamine into perovskite structures have been introduced above. Owing to the relatively strong van der Waals interaction force, 2D perovskites show increased stability than their 3D polymorphs.<sup>155</sup> Because the rich organic cations can be adapted into the perovskite lattice, abundant 2D perovskites have been synthesized so far. Among them, some 2D hybrid perovskites show broadband white light emission, which is related to the self-trapped excited states created by lattice deformation.<sup>233–242</sup> These 2D LHPs can serve as a single-component, broadband white light emitter for pc-LEDs; however, the low PLQYs limit their applications in lighting devices. Zhang *et al.*<sup>243</sup> synthesized highly luminescent 2D  $(\text{PEA})_2\text{PbX}_4$  ( $\text{PEA} = \text{phenylethylamine}$ ,  $\text{C}_8\text{H}_9\text{NH}_3$ ) nanosheets (NSs). The obtained  $(\text{PEA})_2\text{PbBr}_4$  NSs shows the highest PLQY of 46.5% among the  $(\text{PEA})_2\text{PbX}_4$  family. The PL intensity of  $(\text{PEA})_2\text{PbI}_4$  NS solutions preserved a value of 53% under illumination for 60 minutes, while 22% of the original intensity was sustained for  $\text{MAPbI}_3$  QD solution. Formation of 2D–3D perovskite films by rationally introducing long chain amines leads to a decent device performance and long device lifetime for PV and EL applications, which has attracted intense attention.<sup>160–163</sup> However, such research on multidimensional PQD structures has little been done so far. Mathews *et al.*<sup>244</sup> prepared highly luminescent PQDs with an assumed 2D–3D core–shell structure. The core–shell PQDs show intriguing optical characteristics and enhanced environmental stability, which will be discussed in Section 3.3.2.

**3.1.2. B-Site doping.** Zhu *et al.*<sup>245</sup> proposed that the A-site cations might not so greatly affect the characteristics of band edge carriers by comparing the band edge carrier dynamics in  $\text{MAPbBr}_3$ ,  $\text{FAPbBr}_3$ , and  $\text{CsPbBr}_3$  single crystals. And B-site doping has been regarded as an essential technique that can not only adjust the optoelectronic characteristics and endow novel functionalities to LHPs but also enhance their robustness.<sup>246–248</sup>

Among the numerous reports on this issue, doping Mn<sup>2+</sup> into PQDs has received the most intention.<sup>102,249–262</sup> Owing to the internal transition of the Mn<sup>2+</sup> impurity from <sup>4</sup>T<sub>1</sub> to <sup>6</sup>A<sub>1</sub>, the as-prepared CsPbCl<sub>3</sub>:Mn PQDs showed a second emission at the channel of ~2.15 eV (Fig. 11A).<sup>249</sup> The optimized Mn<sup>2+</sup> doped CsPbCl<sub>3</sub> PQDs showed an increased PL QY up to 27%, whereas the undoped PQDs had relatively low fluorescence brightness (PL QY < 5%). Zhang *et al.*<sup>251</sup> prepared high Mn doped CsPb<sub>x</sub>Mn<sub>1-x</sub>Cl<sub>3</sub> PQDs. The obtained PQDs retained the original tetragonal structure of the CsPbCl<sub>3</sub> host even when 46% Pb<sup>2+</sup> were replaced by Mn<sup>2+</sup>. The PL QYs of CsPb<sub>x</sub>Mn<sub>1-x</sub>Cl<sub>3</sub> PQDs increased from 5 to 54% along with the increasing Mn substitution ratio. The crystal structures and the enhanced PL properties can be retained after being replaced under ambient air for over 3 months. Moreover, the bright orange-red light emitted by pc-LEDs fabricated from CsPb<sub>0.73</sub>Mn<sub>0.27</sub>Cl<sub>3</sub> PQDs did not change even after continuous working for 200 h, which indicates the prolonged device lifetime of Mn-doped lead chloride PQDs. Chen and coworkers<sup>102</sup> reported a Mn<sup>2+</sup>-doped strategy to improve the environmental stability and PL properties of PQDs. CsPbBr<sub>3</sub>:Mn PQDs preserved about 60% of the initial PL brightness upon exposure to ambient air for 120 days (Fig. 11B). In contrast, the PL of undoped CsPbBr<sub>3</sub> QDs quenched within 30 days in ambient air. First-principle calculations corroborated that the enhanced stability and PL performance are ascribed to the increased formation energies by Mn<sup>2+</sup> doping. Similarly, the  $\alpha$ -CsPbI<sub>3</sub> PQDs with metastable phase can be stabilized by incorporating Mn ions into the lattice.<sup>263</sup> The highly luminescent CsPb<sub>x</sub>Mn<sub>1-x</sub>I<sub>3</sub> quantum dot films retain their initial  $\alpha$ -phase and strong PL emission after one-month storage, whereas the

luminescent film drop-cast from  $\alpha$ -CsPbI<sub>3</sub> PQDs completely degrade to nonemissive  $\delta$ -CsPbI<sub>3</sub> within 5 days (Fig. 11C). The calculations based on the DFT revealed that the enhanced robustness of  $\alpha$ -CsPbI<sub>3</sub> PQDs was associated with the increased Goldsmith tolerance factor and the cohesive energy through Mn<sup>2+</sup> doping.

Böhm *et al.*<sup>264</sup> synthesized lead-free CsSnX<sub>3</sub> PQDs with tunable emission spanning from 442 nm to the NIR regions. Nevertheless, the bivalent Sn<sup>2+</sup> ions are sensitive to oxygen and will be easily oxidized to Sn<sup>4+</sup>, which results in decreasing PL QYs to nondetectable values. Deng *et al.*<sup>265</sup> fabricated CsSnBr<sub>3</sub> hollow nanocages with better environmental stability by using stannous 2-ethylhexanoate as the tin source at a higher temperature (Fig. 12A). The absorbance spectra of CsSnBr<sub>3</sub> nanocages show a few changes after 3 hour exposure to ambient air, whereas the CsSnBr<sub>3</sub> nanocubes undergo a visible decomposition within 2 h. Surface modification with perfluorooctanoic acid (PFOA) can further improve the stability of CsSnBr<sub>3</sub> nanocages. No obvious changes in the absorption spectra of PFOA treated CsSnBr<sub>3</sub> nanocage films were observed after 16 h of storage in ambient air. The enhanced robustness might be attributed to the stronger interaction between Sn<sup>2+</sup> and the electron-withdrawing F<sup>-</sup> in contrast to Br<sup>-</sup>. SnBr<sub>2</sub><sup>266</sup> and SnF<sub>2</sub><sup>267</sup> surface treatments were also demonstrated to be efficient strategies to improve the oxygen-stability of CsSnX<sub>3</sub>. Although these methods aim at protecting CsSnX<sub>3</sub>, the environmental stability of tin-based perovskites is still lower than that of lead-based perovskites. Deng and coworkers<sup>268</sup> synthesized Cs<sub>2</sub>SnI<sub>6</sub> NCs with variable shapes such as QDs, nanorods, nanowires, nanobelts and

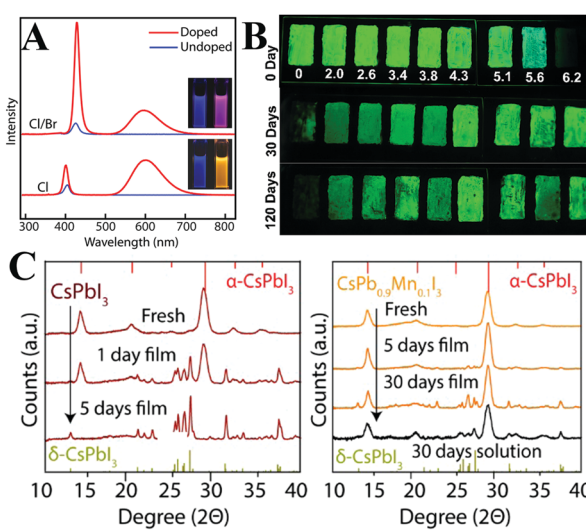


Fig. 11 (A) PL spectra of Mn-doped and undoped CsPbCl<sub>3</sub> and CsPb(Cl/Br)<sub>3</sub> PQDs. The insets are photographs of the sample under UV excitation. Reprinted with permission from ref. 249. Copyright 2016, American Chemical Society. (B) PL emission photographs of CsPbBr<sub>3</sub>:Mn QDs coated on the surface of a glass slide with different Mn<sup>2+</sup> contents from 0 to 6.2 mol% taken under UV irradiation at the indicated time periods. (C) XRD patterns of CsPbI<sub>3</sub> and CsPb<sub>x</sub>Mn<sub>1-x</sub>I<sub>3</sub> PQD films before and after 5/30 days of storage. (B and C) Reprinted with permission from ref. 102 and 263, respectively. Copyright 2017, American Chemical Society.

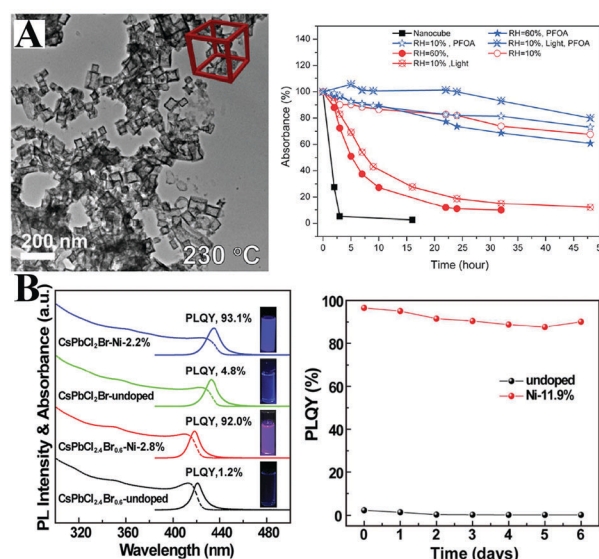


Fig. 12 (A) TEM images of CsSnBr<sub>3</sub> nanocages (left) and relative absorbance intensity at 620 nm as a function of time under various conditions (right). Reprinted with permission from ref. 265. Copyright 2017, American Chemical Society. (B) Absorption and PL spectra of undoped and doped CsPb(Cl/Br)<sub>3</sub> PQDs. The inset shows the photographs of an QD solution under UV (365 nm) illumination. PL stability of pristine PQDs and Ni-doped PQDs (right). Reprinted with permission from ref. 274. Copyright 2017, American Chemical Society.

nanoplates by using  $\text{SnI}_4$  as precursor. The unoxidizable tetravalent tin ions impart ultrahigh stability to  $\text{Cs}_2\text{SnI}_6$  NCs. It is worthy to note that the measured PL QYs of Sn-based perovskites are much lower (0.14% for  $\text{CsSnBr}_3$  nanocubes,<sup>264</sup> 2.1% for  $\text{CsSnBr}_3$  nanocages,<sup>265</sup> 0.48% for  $\text{Cs}_2\text{SnI}_6$  QDs<sup>268</sup>) than those of Pb-based analogues. Overall, the optical properties of tin halide perovskites are far from the requirements of pc-LEDs.

Although a total substitution of Pb by Sn seems to be not reliable at the current stage, partial replacement may retain the outstanding optical properties of LHPs and reduce the toxicity of lead content.<sup>269</sup> As expected, doping Sn into LHP films leads to a red-shift in absorption, which is attributed to the smaller bandgap of tin halide perovskites.<sup>270</sup> However, doping Sn into  $\text{CsPbBr}_3$  NCs (synthesized at a low temperature) leads to an abnormal blueshift that is likely associated with the tilting of the  $\text{PbBr}_6$  octahedra.<sup>271,272</sup> The PL QYs of the Sn(II)-doped NCs decreased due to the gradual oxidation of  $\text{Sn}^{2+}$ . Liu and coworkers<sup>273</sup> prepared  $\text{CsPb}_{1-x}\text{Sn}_x\text{Br}_3$  PQDs at a higher temperature. The  $\text{Sn}^{2+}$  was oxidized to  $\text{Sn}^{4+}$  during synthesis and the tetravalent Sn ions doped into the  $\text{CsPbBr}_3$  hosts as confirmed by X-ray absorption near-edge spectroscopy (XANES). Hence, the  $\text{CsPb}_{1-x}\text{Sn}_x\text{Br}_3$  PQDs with partial  $\text{Sn}^{4+}$  substitution present high environmental stability, unlike the  $\text{Sn}^{2+}$ -substitution. Additionally, Sn(IV)-doping leads to increased PL QYs from 45% to 85%.

Despite the ultrahigh PL QYs of PQDs in the green and red region, the PLQYs of violet-emitting  $\text{CsPbCl}_x\text{Br}_{1-x}$  PQDs are much lower. Recently, Sun *et al.*<sup>274</sup> found that the poor PL properties of violet-emitting PQDs derive from halide vacancy-induced short-range disorder of the lattice. They prepared  $\text{Ni}^{2+}$ -doped  $\text{CsPbCl}_x\text{Br}_{1-x}\text{:Ni}$  PQDs with near-unity PL QYs in the violet spectral range (Fig. 12B). Ni-Doping led to improved local structural order of the lattice and deactivated structural defects. DFT calculations revealed that the defect formation energy increased by Ni-doping. Hence, highly violet emissive  $\text{CsPbCl}_x\text{Br}_{1-x}\text{:Ni}$  PQDs show promise in violet-emitting perovskite-based devices. Meng *et al.*<sup>247</sup> prepared stable blue emitters by doping  $\text{Al}^{3+}$  into  $\text{CsPbBr}_3$  PQDs. Due to the similar bond energy between Al-Br and Pb-Br, the  $\text{Al}^{3+}$  impurity can easily incorporate into the  $\text{CsPbBr}_3$  lattice.

Tang and coworkers<sup>275</sup> firstly synthesized  $\text{MA}_3\text{Bi}_2\text{Br}_9$  PQDs with a PL QY of 12%. Through anion exchange reaction, the emission wavelength can be tuned from 360 to 540 nm. The PL QY of  $\text{MA}_3\text{Bi}_2\text{Br}_9$  PQDs can be further improved up to 54.1% by Cl-passivation.<sup>276</sup> Beyond the improved PL, the Cl-treated  $\text{MA}_3\text{Bi}_2\text{Br}_9$  PQDs also show enhanced photostability as shown in Fig. 13A. They also synthesized blue emissive all-inorganic  $\text{Cs}_3\text{Bi}_2\text{Br}_9$  PQDs with a PL QY of 19.4% by utilizing ethanol as the antisolvent.<sup>277</sup> The PL peaks can be tuned from 380 to 526 nm by anion exchange.<sup>278</sup> Unlike the unstable  $\text{CsPbI}_3$ ,  $\text{Cs}_3\text{Bi}_2\text{I}_9$  PQDs manifest outstanding robustness in ambient air over months.<sup>279</sup> Han *et al.*<sup>280</sup> also fabricated all-inorganic  $\text{Cs}_3\text{Bi}_2\text{X}_9$  PQDs with the PL peak ranging from 400 to 560 nm. The obtained  $\text{Cs}_3\text{Bi}_2\text{X}_9$  PQDs retained the initial phase even after being stored in ambient air over 30 days, which indicates their high stability. Begum *et al.*<sup>281</sup> reported  $\text{CsPbBr}_3$  NCs with

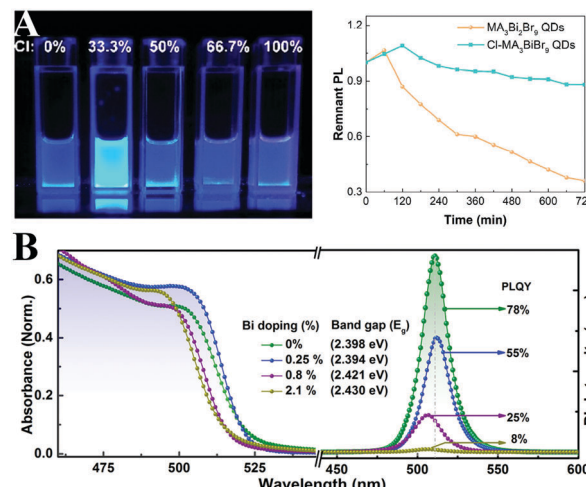


Fig. 13 (A) Photographs of  $\text{MA}_3\text{Bi}_2\text{Br}_9$  QD solutions under 325 nm UV lamp excitation (left), and PL stability of pristine QDs and Cl-passivated QDs (right). Reprinted with permission. Copyright 2018 from ref. 276, American Chemical Society. (B) Absorption and PL spectra of  $\text{CsPbBr}_3$  with varied Bi-doping ratios. Reprinted with permission. Copyright 2016 from ref. 281, American Chemical Society.

$\text{Bi}^{3+}$  substitution *via* an *in situ* doping approach. The PL QYs of  $\text{CsPb}_{1-x}\text{Bi}_x\text{Br}_3$  ( $0 \leq x \leq 2.1\%$ ) NCs decreased from 78% to 8% along with the increasing replacement by  $\text{Bi}^{3+}$  (Fig. 13B). Further research shows that substitution of  $\text{Bi}^{3+}$  remarkably increased the sub-band gap density of states, which also results in increased nonradiative recombination centers.<sup>282</sup> Song and coworkers<sup>283</sup> introduced  $\text{Bi}^{3+}$  and  $\text{Mn}^{2+}$  into the  $\text{CsPbCl}_3$  NCs to expand the emission spectra. The  $\text{Bi}^{3+}/\text{Mn}^{2+}$  codoped NCs achieved single-component white emission by tuning the concentration of  $\text{Bi}^{3+}$  and  $\text{Mn}^{2+}$  under UV light excitation.

Antimony and bismuth belong to one family, and they exhibit similar properties in some respects. All-inorganic  $\text{Cs}_3\text{Sb}_2\text{Br}_9$  PQDs with high bright blue emission can be synthesized by the similar LARP method.<sup>284</sup> The measured PL QY is 46%, which is superior to that of blue-emitting  $\text{CsPbCl}_3$  PQDs.  $\text{Cs}_3\text{Sb}_2\text{Br}_9$  PQDs retained 70% of original PL intensity after stored in air for 35 days (Fig. 14A). In addition, by halide exchange reactions, the PL emission of  $\text{Cs}_3\text{Sb}_2\text{X}_9$  PQDs can be tuned from 370 to 560 nm. The  $\text{Sb}^{3+}$ -doped  $\text{CsPb}_{1-x}\text{Sb}_{2x/3}\text{I}_3$  perovskite films were prepared by Chen and coworkers.<sup>285</sup> The phase stability and film morphology are enhanced after  $\text{Sb}^{3+}$ -doping. However, to the best of our knowledge,  $\text{Sb}^{3+}$ -doped LHP nanomaterials have not been investigated yet. Sb-Doping may show promise in designing stable perovskite nanomaterials.

Recently,  $\text{A}_2\text{B}(\text{i})\text{B}'(\text{III})\text{X}_6$ -type double perovskites have attracted great attention, especially  $\text{Cs}_2\text{AgBiX}_6$ .<sup>286–289</sup> Although the quantum efficiencies for  $\text{Cs}_2\text{AgBiX}_6$  PQDs are rather low at the current stage, the environmental stability is much better than other lead-less halide perovskites. More research should be devoted to this issue.

Rare earth (RE) ion activated luminescent materials are widely used in lighting and display devices. Owing to the abundant energy level of the RE ion, the obtained RE-doped PQDs achieved

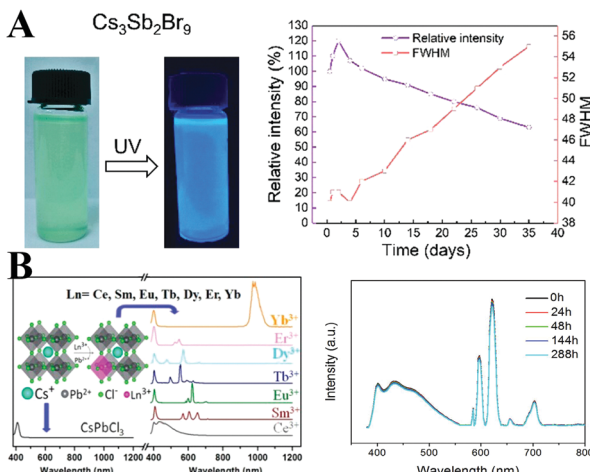


**Fig. 14** (A) Photographs of  $\text{Cs}_3\text{Sb}_2\text{Br}_9$  PQDs under UV lamp excitation (left), and environmental stability of  $\text{Cs}_3\text{Sb}_2\text{Br}_9$  PQDs (right). Reprinted with permission from ref. 284. Copyright 2018, American Chemical Society. (B) PL spectra of  $\text{CsPbCl}_3$  doped with different lanthanide ions (left) and the emission spectra of the white LED device fabricated from  $\text{Ce}^{3+}$  and  $\text{Eu}^{3+}$  ion codoped  $\text{CsPbCl}_3$  PQDs acquired at different working times at a bias of 3.0 V (right). Reprinted with permission from ref. 292. Copyright 2017, American Chemical Society.

multiple color emissions by energy transfer from the  $\text{CsPbBr}_3$  host to the RE impurities.<sup>290</sup> McLeod *et al.*<sup>291</sup> prepared Eu-doped  $\text{MAPb}_{1-x}\text{Eu}_x\text{Br}_3$  PQDs by the LARP method. The Eu is demonstrated to be a suitable element for substituting Pb without the change of crystal structure. At high Eu-substitution, blue luminescence originating from  $\text{Eu}^{2+}$  was observed in  $\text{MAPb}_{1-x}\text{Eu}_x\text{Br}_3$  PQDs, revealing their potential in optoelectronics. Song and coworkers<sup>292</sup> incorporated diversified RE ions including  $\text{Ce}^{3+}$ ,  $\text{Sm}^{3+}$ ,  $\text{Eu}^{3+}$ ,  $\text{Tb}^{3+}$ ,  $\text{Dy}^{3+}$ ,  $\text{Er}^{3+}$ , and  $\text{Yb}^{3+}$  into the wider band gap  $\text{CsPbCl}_3$  PQDs at a higher reaction synthetic temperature. The as-prepared  $\text{CsPbCl}_3:\text{RE}$  PQDs exhibit unique RE emissions ranging from visible to NIR regions together with high PL QYs and high stability (Fig. 14B). Interestingly, the  $\text{Yb}^{3+}$ -doped  $\text{CsPbCl}_3$  PQDs with a NIR emission centered at  $\sim 1000$  nm present a high PL QY of 170%, which is attributed to the quantum cutting of excitonic transition of  $\text{CsPbCl}_3$  hosts.<sup>293</sup> The  $\text{Yb}^{3+}/\text{Er}^{3+}$  co-doped  $\text{CsPbCl}_3$  PQDs emit 1533 nm NIR light. The co-doped PQDs present better stability than the undoped  $\text{CsPbCl}_3$  PQDs.<sup>294</sup> Such materials can serve as optically active layers for silicon solar cells to improve the performance.<sup>295</sup> The  $\text{Ce}^{3+}$  cation with a similar ionic radius and higher energy level located in the CB of the perovskite hosts has been regarded as a favorite dopant for  $\text{CsPbBr}_3$  PQDs. The  $\text{CsPbBr}_3:\text{Ce}$  PQDs sustain the structural integrity of the perovskite and exhibit a PL enhancement from 41% to 89% owing to the modulation of PL kinetics by  $\text{Ce}^{3+}$ -doping.<sup>296</sup> The co-doping of  $\text{Ce}^{3+}$  and  $\text{Eu}^{3+}$  ions into  $\text{CsPbCl}_3$  hosts produces a cool white emission.<sup>292</sup> And white light pc-LEDs fabricated by combining them on a 365 nm LED chip show a high luminous efficiency of  $24 \text{ lm W}^{-1}$  and a long device lifetime.

Overall, doping has been widely accepted as an effective strategy for tailoring and enhancing the optical performance

and improving the stability of PQDs. The optical properties and the stability assessments of some promising PQDs are summarized in Table 1.

### 3.2. Surface engineering

The surface of semiconductors plays a significant role in carrier recombination processes, and the surface defects result in severe PL quenching.<sup>297</sup> The surface defects are more crucial for colloidal QDs owing to the large surface-to-volume ratio.<sup>298</sup> Although numerous theoretical<sup>299–301</sup> and experimental<sup>302,303</sup> research studies have revealed that the LHPs exhibit a high defect tolerance, they are not defect impervious. Moreover, the ill-passivated surfaces are highly susceptible to moisture.<sup>53</sup> Therefore, it is essential to seek suitable surface ligands that not only enhance the PL performance but also improve the stability.

Generally, PQDs are capped by long alkyl OA and OLA (octylamine for  $\text{MAPbX}_3$  PQDs) molecules. Jasieniak *et al.*<sup>304</sup> proposed that the phase instability of  $\text{CsPbI}_3$  PQDs originates from the interaction between the ion-pairs of OA ligands and the surface of  $\text{CsPbI}_3$  PQDs. They stabilized  $\text{CsPbI}_3$  PQDs by replacing conventional OA with bis-(2,2,4-trimethylpentyl)phosphinic acid (TMPPA). The PL performance of OLA and TMPPA passivated  $\text{CsPbI}_3$  PQDs (denoted as  $\text{CsPbI}_3-\text{TMPPA}$ ) is similar to that of conventional OLA and OA capped  $\text{CsPbI}_3$  PQDs (denoted as  $\text{CsPbI}_3-\text{OA}$ ). Compared with  $\text{CsPbI}_3-\text{OA}$  decomposing within 3 days, the PL intensity of  $\text{CsPbI}_3-\text{TMPPA}$  nearly preserved the initial value upon storage over 20 days (Fig. 15A). Replacing OA with TMPPA effectively slows down the  $\alpha$ -to- $\delta$  phase transformation of  $\text{CsPbI}_3$ .

The molecules with large steric hindrance such as highly branched (3-aminopropyl)triethoxysilane (APTES),<sup>305,306</sup> polyhedral silsesquioxane-[3-(2-aminoethyl)amino]propylheptaisobutyl substituted ( $\text{NH}_2\text{-POSS}$ ),<sup>305</sup> 1-tetradecylphosphonic acid (TDPA),<sup>307</sup> 2-adamantylammonium bromide (ADBr),<sup>308</sup> trioctylphosphine oxide (TOPO),<sup>309</sup> mercapto- $\beta$ -cyclodextrin (SH- $\beta$ -CD),<sup>310</sup> poly(lactic acid) (PLA),<sup>311</sup> and cage-like polyhedral oligomeric silsesquioxane (POSS)<sup>107</sup> could bestow high protic solvent resistance to perovskites. From the stability test, such branched ligands could effectively prevent the protic solvents from penetrating into the PQDs' surface, in contrast to the OA and OLA capped PQDs transforming into a non-luminescent state or decomposing directly in the same condition. Moreover, the light-induced agglomeration is impeded by the large steric hindrance, which ensures high photostability. For example, by using ADBr as the unique surface ligand, the PL QYs of  $\text{MAPbBr}_3$  quasi-spherical nanoparticles reach almost unity.<sup>308</sup> The special ligands form cucurbit[7]-uril-adamantyl ammonium host-guest complexes upon illumination in humid conditions, which can avoid the photodarkening effect and improve the water stability (Fig. 15B). However, immoderate incorporation of branched ligands like APTES results in an ill-passivated surface.<sup>305</sup>

Ligand passivation always relates to the deactivated quenching defects. Trioctylphosphine (TOP),<sup>312–314</sup> diphenylphosphinic acid (DPPA),<sup>315</sup> di-dodecyl dimethyl ammonium bromide (DDAB),<sup>302,316</sup> didodecyl dimethylammonium sulfide (SDDA),<sup>317</sup> PEA,<sup>318</sup> benzyl

Table 1 Summary of PL properties and stability of PQDs

PQDs	Synthetic method	Emission peak (nm)	FWHM (nm)	PL QYs (%)	Stability	Ref.
CsPbCl <sub>3</sub>	LARP	405	12	10		55
	Ultrasonication			10	8% (4 months, air)	45
	Microwave irradiation	410	14	7		80
K <sub>x</sub> Cs <sub>1-x</sub> PbCl <sub>3</sub> :Eu	Hot-injection (185 °C)	408	12.1	31.2		229
CsPbCl <sub>3</sub> :Ni	Hot-injection (210 °C)	407		96.5	>90% (6 d, air)	274
Cs <sub>2</sub> AgBiCl <sub>6</sub>	LARP	395	68	6.7		287
Cs <sub>3</sub> Bi <sub>2</sub> Br <sub>9</sub>	LARP	468	40	4.5	77% (400 min, UV)	280
MA <sub>3</sub> Bi <sub>2</sub> Br <sub>9</sub>	LARP	430	62	12	92% (25 h, UV)	275
Cl-MA <sub>3</sub> Bi <sub>2</sub> Br <sub>9</sub>	LARP	422	41	54.1	89% (12 h, UV)	276
Cs <sub>3</sub> Sb <sub>2</sub> Br <sub>9</sub>	LARP	410	41	46	70% (35 d, air) 50% (108 h, UV)	284
CsPbBr <sub>1.5</sub> Cl <sub>1.5</sub>	LARP	455	16	37		55
CsPbBr <sub>3</sub> :Al	Hot-injection (150 °C)	456	16	42		247
CsPb(Br/I) <sub>3</sub> :Al	Hot-injection (150 °C)	536		40		247
CsPbBr <sub>3</sub>	LARP	513	20	95	90% (30 d, air) 89% (4 months, air)	55
	Ultrasonication			92		45
	Microwave irradiation	517	17	90		80
	Hot-injection (160 °C)	509	16	~92 ± 2		322
	Hot-injection (180 °C)	507	27	90	91% (30 d, air)	55
MAPbBr <sub>3</sub>	LARP	505	21	70		56
	Spray synthesis	511	22	~100	91% (2 months, air)	81
FAPbBr <sub>3</sub>	LARP	530	22	75	38% (1 h, 100 °C)	82
	Modified hot-injection (130 °C)	530	22	85	Retain PL after 2–3 cycles of purification	224
(K/Cs)PbBr <sub>3</sub>	Post-synthesis	512	20	83	100% (153 h, blue light)	228
CsPb <sub>1-x</sub> Sn <sub>x</sub> Br <sub>3</sub> (0 ≤ x ≤ 0.1)	Post-synthesis	479–512		62		272
CsPbBr <sub>3</sub> :Sn(IV)	Hot-injection (180 °C)	517	20	83		273
CsPbBr <sub>3</sub> :Ce	Hot-injection (185 °C)	510		89	60% (30 d, air)	296
CsPbBr <sub>3</sub> :Mn	Hot-injection (150 °C)	514–517	20	90	60% (120 d, air)	102
CsPbCl <sub>3</sub> :Mn	Hot-injection (150 °C)	589		27		249
CsPb <sub>0.73</sub> Mn <sub>0.27</sub> Cl <sub>3</sub>	Hot-injection (170 °C)	580		54	40% (60 min, UV)	251
(C <sub>4</sub> H <sub>9</sub> NH <sub>3</sub> ) <sub>2</sub> PbBr <sub>4</sub> :Mn	Annealing at 125 °C	600		37	80% (8 d, air)	259
CsPbBr <sub>1.5</sub> I <sub>1.5</sub>	LARP	600	38	72		55
CsPbI <sub>3</sub>	Ultrasonication			90	0% (2 months, air)	45
	Microwave irradiation	691	35	70		80
CsPbI <sub>3</sub> :Mn	Hot-injection (150 °C)	680	40	82 ± 9	Stable over a month	263
FA <sub>0.1</sub> Cs <sub>0.9</sub> PbI <sub>3</sub>	Modified hot-injection (80 °C)	685		>70	>95% for month	225

alcohol ( $\text{BnOH}$ ),<sup>319</sup>  $\text{YCl}_3$ <sup>320</sup> and  $\text{ZnX}_2$  salts<sup>321</sup> can control the ligand binding motifs, and enhance the PL QYs and phase duration. For instance, Shen *et al.*<sup>312</sup> synthesized CsPbI<sub>3</sub> PQDs with PL QYs of near unity by using TOP-PbI<sub>2</sub> as precursor (Fig. 16A). Time-resolved TA spectroscopy revealed negligible electron or hole trapping pathways for TOP-CsPbI<sub>3</sub> PQDs, which implies that the TOP molecules well passivate the CsPbI<sub>3</sub> surface. TOP-CsPbI<sub>3</sub> samples retain ~85% of the original PL intensity after being stored for 30 days. In comparison, the PL QYs of the non-TOP capped sample decreased from 86% to 60% within 1 month. The enhanced environmental stability is likely associated with the improved crystalline quality combined with less quenching defects in TOP-CsPbI<sub>3</sub>. Beyond the enhanced stability by TOP passivation, the PL intensity of aged CsPbI<sub>3</sub> PQDs can recover to their initial value (Fig. 16B). This is attributed to the fact that some ions migrate to the surface of PQDs and repair the surface defects in the presence of TOP.<sup>313</sup>

Post-synthetic treatment can also effectively eliminate the surface trap. Alivisatos *et al.*<sup>322</sup> proposed that the surface trapping originates from the lead-rich surface of perovskites due to the lead-rich synthetic environments. Hence, they developed a postsynthetic thiocyanate surface treatment strategy to repair

the lead-rich surface. As expected, the surface trap of both fresh (with PLQYs of ~92%) and aged (with PLQYs of ~63%) CsPbBr<sub>3</sub> PQDs deactivated by thiocyanate treatment, and the treated samples showed near-unity PLQYs together with high stability (Fig. 17A). Samanta *et al.*<sup>323</sup> reported a more general strategy to enhance the PL of CsPbX<sub>3</sub> PQDs by treating them with tetrafluoroborate salts. The PL QYs of the green emissive CsPbBr<sub>3</sub> and blue emissive CsPbBr<sub>x</sub>Cl<sub>3-x</sub> could reach near unity. However, these two strategies seemed to make little success with CsPbBr<sub>x</sub>I<sub>3-x</sub>. CsPbBr<sub>x</sub>I<sub>3-x</sub> PQDs suffer from a faster degradation and PL quenching than their bromide counterparts.<sup>324</sup> Therefore, a CsPbBr<sub>3</sub> layer like CsPbI<sub>3</sub>@CsPbBr<sub>3</sub> core-shell structures might protect CsPbI<sub>3</sub>. Ethanol or acetone could selectively etch the surface of iodine-containing CsPbBr<sub>x</sub>I<sub>3-x</sub> PQDs and result in a bromine-rich protective self-passivation layer. Consequently, the protective layer improves the stability of the CsPbBr<sub>x</sub>I<sub>3-x</sub> PQDs by three orders of magnitude (Fig. 17B). As for blue emissive perovskite NCs, Feldmann and coworkers<sup>325</sup> found that dispersing CsPbBr<sub>3</sub> nanoplates in PbBr<sub>2</sub>-ligand (OA and oleylamine) solutions can boost their PL QYs from 7% to 42%. The PbBr<sub>2</sub>-ligands could effectively repair the surface trap, which leads to PL enhancement. Moreover, the CsPbBr<sub>3</sub>

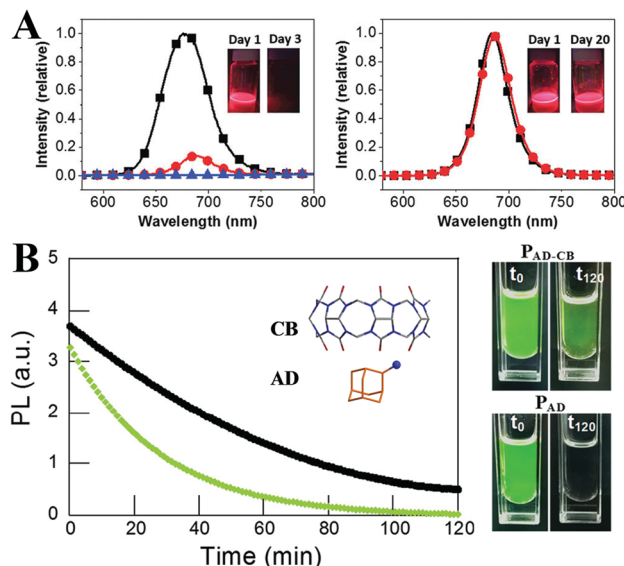


**Fig. 15** (A) PL spectra of  $\text{CsPbI}_3\text{-OA}$  (left) and  $\text{CsPbI}_3\text{-TMPPA}$  (right), respectively. The insets are the solutions of the respective PQDs under UV light at different times following synthesis. Reprinted with permission from ref. 304. Copyright 2017, The Royal Society of Chemistry. (B) PL of  $P_{\text{AD-CB}}$  (black line) and  $P_{\text{AD}}$  (green line) dispersed in toluene and in contact with water as a function of the irradiation time; the inset shows the molecular structures of CB and AD ligands. The right images are the colloidal dispersions immediately after the addition (left) of water and 120 min later (right). Reprinted with permission from ref. 308. Copyright 2016, Wiley-VCH.

nanoplates show improved colloidal stability and photostability after  $\text{PbBr}_2$ -ligands treatment (Fig. 17C).

Zhong *et al.*<sup>326</sup> proposed that the decomposition of  $\text{MAPbI}_3$  is attributed to the defective surface interacting with coordinated solvents and/or iodine vacancies. The noncoordinated acetonitrile (ACN) was chosen to dissolve the perovskite precursors. The obtained  $\text{MAPbI}_3$  PQDs manifest high air stability owing to the defect-less surface. Deng and coworkers<sup>327</sup> made an X-type ligand to fix the surface defects of  $\text{CsPbBr}_3$  PQDs. The additive  $\text{Pb}^{2+}$  sites could fill the  $\text{Cs}^+$  terminated traps. The formation of  $\text{PbBr}_2$ -terminated PQDs led to slight PL enhancement. Moreover, the compact ligand layer ensures stability in polar solvents.

The OA and OLA molecules are not tightly bound to the surface of PQDs but undergo fast exchange between their bound and free state. The dynamic surface might be the origin of the color lability. And the ligands are easily lost during purification, which leads to poor colloidal stability.<sup>97</sup> Brutchey *et al.*<sup>328</sup> firstly quantified the ligands binding to the PQDs. Acid- and amine-based ligands undergo exchange between their bound and free state, whereas the phosphonic acid ligands can tightly bind to the surface. Hence, employing phosphonic acid ligands can minimize the ligand loss. Besides phosphonic acid ligands, Sun and coworkers<sup>329</sup> employed stearic acid (SA) and octadecylamine (ODA) with a similar long alkyl chain but a higher melting-point around 50–70 °C to cap  $\text{FAPbBr}_3$  PQDs. As a result, the ligand adsorption-desorption is eliminated in contrast to the PQDs capped by the liquid OA and OLA with a melting-point around 15–25 °C. The highly luminescent

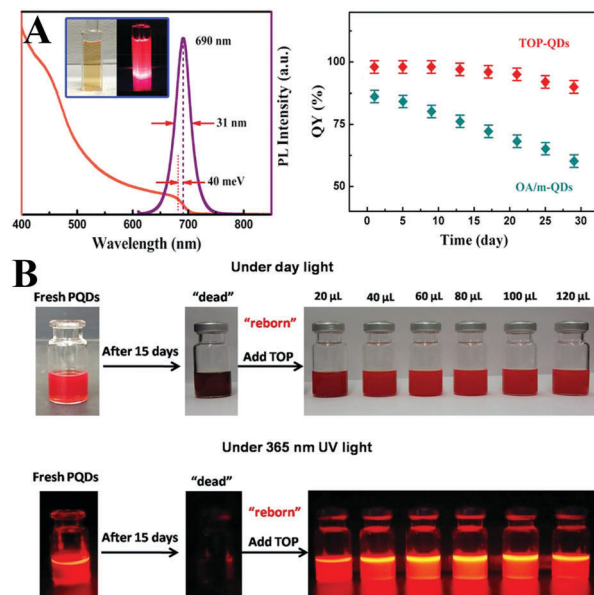


**Fig. 16** (A) UV-vis absorption and PL spectra of  $\text{CsPbI}_3$  PQDs. The inset shows the photos of the  $\text{CsPbI}_3$  solution under the room light (left) and UV lamp ( $\lambda = 365 \text{ nm}$ ) (right) excitation. The right images are the PL QYs of the OA/m- and TOP- $\text{CsPbI}_3$  PQDs over 30 days of storage. Reprinted with permission from ref. 312. Copyright 2017, American Chemical Society. (B) Photos of fresh/aged PQDs and aged PQDs with different amounts of TOP under daylight (top) and UV light (bottom). Reprinted with permission from ref. 313. Copyright 2018, American Chemical Society.

$\text{FAPbBr}_3$  PQDs capped by solid ligands maintain 80% of the initial brightness in ambient air over 30 days, whereas the PL of liquid ligand capped PQDs decreases to 40% in the same condition (Fig. 18A). The improved stability can be attributed to the minimal dynamic-surface-induced ligand loss. Similarly, ligands with stronger adhesion can tightly bind to the surface of perovskites and avoid ligand loss during purification. In this respect, SDDA,<sup>317</sup> long chain zwitterionic ligands,<sup>330</sup> and bidentate ligands<sup>331</sup> are employed to passivate the  $\text{CsPbX}_3$  PQDs. The ligands with strong adhesion allow for obtaining clean PQDs with high PL QYs above 90% following multi-purification.<sup>330</sup> The SDDA capped samples show high PL after 34 hours of high-intensity pulsed laser irradiation.<sup>317</sup> And the bidentate ligands can well-stabilize the cubic phase of  $\text{CsPbI}_3$  PQDs.<sup>331</sup>

Crosslinking surface ligands could strengthen the interactions of PQDs and minimize ligand loss. Seferos and coworkers<sup>332</sup> employed a thermally crosslinkable molecule 4-vinylbenzyl-dimethyloctadecylammonium chloride (V18) to passivate the  $\text{MAPbBr}_3$  PQDs. Tan and coworkers<sup>333</sup> explored a trimethylaluminum (TMA) vapor crosslinking method and made  $\text{CsPbX}_3$  PQDs insoluble in solvents. Manna *et al.*<sup>334,335</sup> deposited OA and OLA capped  $\text{CsPbX}_3$  PQDs on a silicon substrate. The intra- and intermolecular C=C bonds form upon X-ray irradiation. The intermolecular C=C bonds link the adjacent PQDs (Fig. 18B). Overall, based on the various crosslinking protocols, the obtained samples could retain high PL QYs in ambient air for a long period of time, because the ligand-crosslinking could minimize the ligand loss.

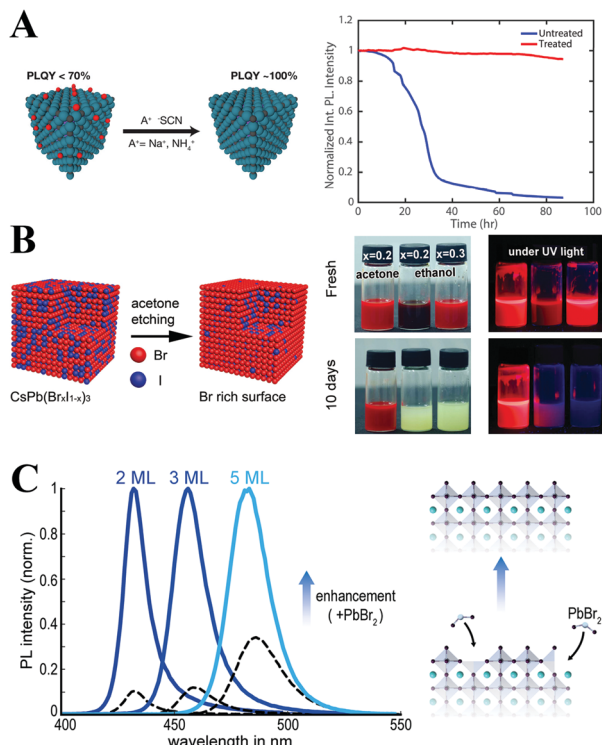


**Fig. 17** (A) Schematic of thiocyanate surface treatment on CsPbBr<sub>3</sub> PQDs. Test of the optical stability of a dilute colloidal sample of treated and untreated particles under continuous illumination with ~100 mW of 365 nm UV light (right). Reprinted with permission from ref. 322. Copyright 2017, American Chemical Society. (B) Schematic of acetone surface treatment on CsPb(BrI)<sub>3</sub> PQDs. Colloidal solution of CsPb(Br<sub>x</sub>I<sub>1-x</sub>)<sub>3</sub> ( $x = 0.1\text{--}0.3$ ) samples in cyclohexane under daylight and UV light illumination. Reprinted with permission from ref. 324. Copyright 2017, The Royal Society of Chemistry. (C) PL spectra of initial CsPbBr<sub>3</sub> nanoplates' colloidal dispersions (black dashed lines) and enhanced dispersions (normalized, solid lines), and scheme for the repair process of surface defects initiated by a chemical post-treatment with a PbBr<sub>2</sub> solution. Reprinted with permission from ref. 325. Copyright 2018, American Chemical Society.

### 3.3. Matrix encapsulation

**3.3.1. Polymer encapsulation.** Polymer matrices with compact molecular chains could effectively encapsulate PQDs and protect them from contact with the environment. Hence, the perovskite–polymer composites exhibit high environment stability especially superior water resistance. Apart from the stability, some polymers could passivate the PQDs and result in enhanced PL performances. Owing to the good compatibility between polymers and perovskites, various perovskite–polymer composites in bulk, film, and monodisperse microsphere forms are fabricated and investigated. In all the cases, polymer coating has been regarded as a powerful strategy for protecting PQDs.

Among the various forms of perovskite–polymer composites, perovskite–polymer films have received a significant attention. On the one hand, numerous strategies have been developed for fabricating high-quality films. On the other hand, the luminescent films can be used as the backlight sources for LCDs. Sargent *et al.*<sup>99</sup> cast highly luminescent CsPbBr<sub>3</sub> quantum dot films by a centrifugal casting process without any matrix additives.

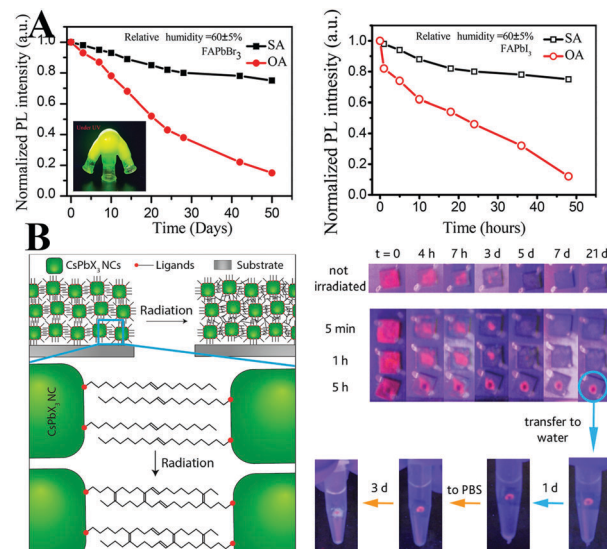


**Fig. 18** (A) Change of PL intensity as a function of storage time of FAPbBr<sub>3</sub> (left) and of FAPbI<sub>3</sub> (right) PQDs. The inset of the left image is the photograph of SA capped FAPbBr<sub>3</sub> solutions under UV light illumination. Reprinted with permission from ref. 329. Copyright 2017, American Chemical Society. (B) Scheme illustrating that intermolecular C=C bonding appears as a consequence of irradiation, linking adjacent NCs in the film (left), and water stability of pristine CsPbI<sub>3</sub> QD films and irradiated films. Reprinted with permission from ref. 335. Copyright 2016, American Chemical Society.

Snaith *et al.*<sup>336</sup> blended the as-prepared PQDs with polystyrene (PS) or polymethyl methacrylate (PMMA) beads, and then the mixture was cast onto a glass substrate and spin-coated to form a dry film (Fig. 19A). The polymer films can prevent anion exchange, which demonstrates their potential in pc-LEDs. Chen *et al.*<sup>337</sup> employed a microfluidic spinning technique to embed CsPbBr<sub>3</sub> PQDs into PMMA fiber films. Yoon and coworkers<sup>338</sup> fabricated ethyl cellulose (EC) with CsPbBr<sub>3</sub> QD films by coating the mixed EC and CsPbBr<sub>3</sub> PQDs toluene solutions on a PET substrate *via* the doctor blade method. Kang *et al.*<sup>339</sup> fabricated perovskite nanoparticle films by size exclusion lithography. Kim *et al.*<sup>340</sup> blended polydimethylsiloxane (PDMS) and Au nanoparticles (NPs) in toluene and cast AuNP/PDMS films firstly. Then the Au NPs can be removed by aqua regia etching, resulting in porous PDMS films. The porous films can be employed as the template for growth of MAPbBr<sub>3</sub> PQDs (Fig. 19B). The emission wavelength of MAPbBr<sub>3</sub> PQDs can be tuned by controlling the size of Au NP templates. Kuo *et al.*<sup>341</sup> encapsulated CsPbX<sub>3</sub> PQDs in stretchable poly(styrene-butadiene-styrene) (SBS) fibers by an electrospinning strategy. The obtained fiber membranes can serve as water-proof multicolor converters for pc-LEDs. Chen and coworkers<sup>342</sup> prepared uniform CsPbX<sub>3</sub>/PAN (polyacrylonitrile) nanofibers by an electrospinning technique. The hydrophobic PAN provides superior resistance towards humidity and water. Yang and coworkers<sup>343</sup> synthesized CsPbX<sub>3</sub>/polymer fibers by *in situ* growth of PQDs in polymer fibers. PQDs with uniform size can be homogeneously encapsulated in the polymer fibers. Dong and coworkers<sup>75</sup> dissolved the perovskite precursor in dimethyl formamide (DMF) solution and deposited

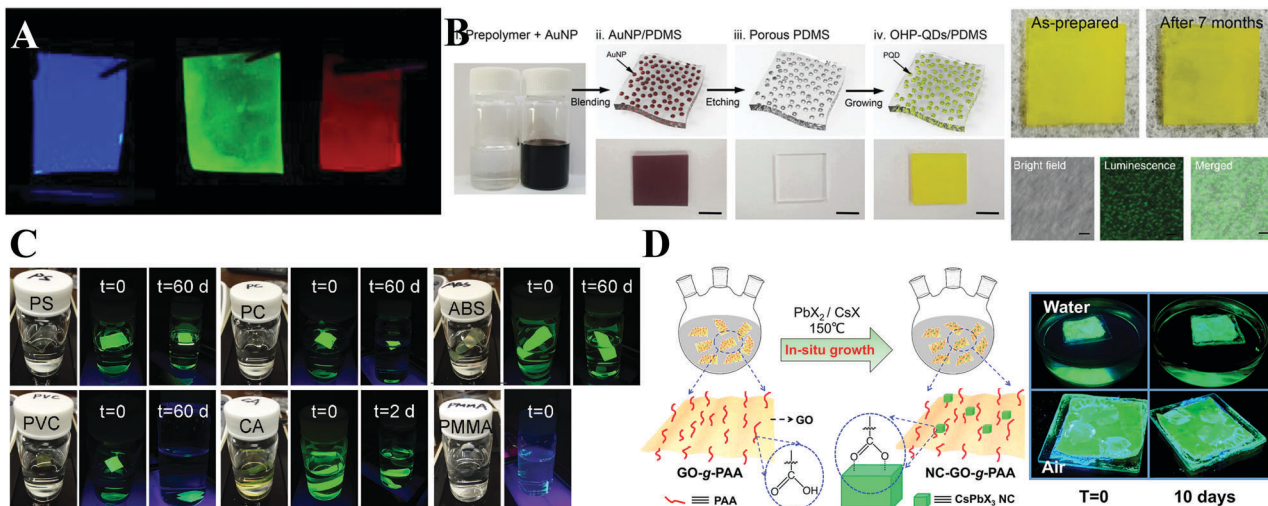


**Fig. 19** (A) Images of the perovskite crystal/polymer composite films emitting blue ( $(\text{OA/MA})\text{PbCl}_3$ ), green ( $(\text{OA/MA})\text{PbBr}_3$ ), and red ( $(\text{OA/MA})\text{PbI}_3$ ) light under UV lamp excitation. Reprinted with permission from ref. 336. Copyright 2015, American Chemical Society. (B) Schematic illustration of MAPbBr<sub>3</sub>-QDs/PDMS film synthesis. The accompanying photographs show the resulting films at each stage. Scale bar = 1 cm. On the right side are photographs of the MAPbBr<sub>3</sub>/PDMS films before and after 7 months of storage together with their bright field and luminescence images. Scale bar = 4 mm. Reprinted with permission from ref. 340. Copyright 2017, The Royal Society of Chemistry. (C) Photographs taken under white light or UV irradiation at the indicated time period. The composite film samples immersed in water are MAPbBr<sub>3</sub>-PS, MAPbBr<sub>3</sub>-PC, MAPbBr<sub>3</sub>-ABS, MAPbBr<sub>3</sub>-PVC, MAPbBr<sub>3</sub>-CA, and MAPbBr<sub>3</sub>-PMMA. Reprinted with permission from ref. 75. Copyright 2016, Wiley-VCH. (D) Illustration of the synthesis of the ternary NC-GO-g-PAA hybrid (left) and the photographs of glass slides coated with NC-GO-g-PAA nanorod films after soaking in water or exposure to air for 0 and 10 days. Reprinted with permission from ref. 346. Copyright 2017, American Chemical Society.

the solution on as-prepared polymer films (PS, PMMA, polycarbonate (PC), acrylonitrile butadiene styrene (ABS), cellulose acetate (CA), and polyvinyl chloride (PVC) were used here). The polymer chains will swell when in contact with good solvents and take in the precursor solutions. After the baking process, the solvents are evaporated, and meanwhile the MAPbBr<sub>3</sub> PQDs are formed in the polymer matrices. As a result, the MAPbBr<sub>3</sub>-PS, MAPbBr<sub>3</sub>-PC, MAPbBr<sub>3</sub>-ABS, MAPbBr<sub>3</sub>-PVC, and MAPbBr<sub>3</sub>-CA films retain high luminescence even when immersed in water over 60 days, whereas the luminescence of MAPbBr<sub>3</sub>-PMMA is quenched rapidly (Fig. 19C). The rapid PL loss is attributed to the low swelling ratio of PMMA in DMF solvent and thus the PQDs only form on the surface of PMMA films. Chen *et al.*<sup>344</sup> prepared flexible CsPbBr<sub>3</sub>/ethylene vinyl acetate (EVA) composite films by crystallization of PQDs and dissolution of EVA in toluene. Their PL intensity did not change even after bending the films over 1000 cycles. Zhong *et al.*<sup>76</sup> reported an *in situ* preparation of MAPbBr<sub>3</sub>/polyvinylidene fluoride (PVDF) composite films. Due to the strong interactions between the  $-\text{NH}_3^+$  group in MAPbBr<sub>3</sub> and the  $-\text{CF}_2-$  groups in PVDF, the obtained MAPbBr<sub>3</sub>/PVDF films show increased PL QYs up to  $94.6 \pm 1\%$ .

When referring to the interactions between polymers and perovskites, poly(maleic anhydride-*alt*-1-octadecene) (PMA)<sup>345</sup> was employed to tighten the ligand binding. The color converter composed of CsPbX<sub>3</sub>-PMA composites shows a prolonged lifetime in comparison with pristine PQDs. Liu and coworkers<sup>346</sup> synthesized polyacrylic acid-grafted graphene oxide (GO-g-PAA), and the hybrid composites were used as ligands for the uptake of the perovskite precursors by coordinating PbBr<sub>2</sub>, forming a

kinetically favorable nucleation point for *in situ* crystal growth (Fig. 19D). Note that such a carboxylate-group-rich polymer can minimize the ligand loss, which improves the colloidal stability of PQDs, but the environmental stability is still limited since the PQDs only lie on the polymer surface instead of being encapsulated. But the addition of the CsPbBr<sub>3</sub>-GO-g-PAA toluene solution into hexane can form self-assembled nanorod-shaped hierarchical superstructures. Thus, self-assembled nanorods provide favorable encapsulation of PQDs, which imparts superior environmental stability to PQDs. Quan *et al.*<sup>347</sup> employed an amphiphilic block copolymer with a hydrophobic PS block and a coordinatable poly-2-vinylpyridine (P2VP) block as a confined nanoreactor for synthesizing CsPbBr<sub>3</sub> PQDs. The PbBr<sub>2</sub> precursors were uptaken by the P2VP block. After the addition of CsBr, a strong PL under UV excitation was observed, indicating the formation of CsPbBr<sub>3</sub> PQDs in the nanoreactors. Liu and coworkers<sup>348</sup> synthesized polystyrene-*b*-poly(ethyl oxide) (PS-*b*-PEO) grafted MAPbBr<sub>3</sub> PQDs. After rehydrating the precipitate in water, the MAPbBr<sub>3</sub> PQDs self-assembled into well-defined vesicular nanostructures, which suggests their great potential for cell imaging (Fig. 20A).

Carboxybenzene (CB) microcrystals with high transparencies, low toxicities, and low refractive index are regarded as a desired matrix for stabilizing perovskites. Chen *et al.*<sup>349</sup> prepared highly stable macroscopic needle-shaped MAPbBr<sub>3</sub>-CB crystals through slow-cooling of the hot toluene solution containing dissolved CB and MAPbBr<sub>3</sub> PQDs. Alivisatos *et al.*<sup>350</sup> encapsulated PQDs in a macroscale polymer including PS, poly(lauryl methacrylate) (PLMA), and poly(styrene-ethylene-butlenestyrene) (SEBS) matrices. The further stability tests revealed that PQDs-PS is the most water resistant, and the photostability of PQDs-PLMA is the

most prominent. Among the three kinds of perovskite–polymer composites, PQDs–SEBS shows high water and photo stability. Yu and coworkers<sup>351</sup> prepared white-emitting composites by encapsulating CsPb(Br/I)<sub>3</sub> PQDs with anthracene. The anthracene can work as a blue-emitting component upon UV light excitation, and simultaneously, it can protect PQDs against environmental-induced decomposition. The polymerizable V18 ligands make it possible to incorporate the PQDs into a polymer matrix by copolymerization.<sup>332</sup> A PQDs–polymer bulk composite was obtained by blending 2,2-azobisisobutyronitrile (AIBN) as the radical initiator with monomers in V18–PQDs solutions. A negligible difference in PL spectra was observed when the bulk composites were immersed in water over 90 days, which demonstrated the ultrahigh stability towards superior water resistance (Fig. 20B). Kovalenko *et al.*<sup>71</sup> conducted photo-induced polymerization by employing bis(2,4,6-trimethylbenzoyl)-phenylphosphineoxide (Irgacure 819) as the photoinitiator and the obtained CsPbX<sub>3</sub> NCs–PMMA polymer monoliths exhibited high luminescence.

Tüysüz *et al.*<sup>352</sup> regarded CsPbI<sub>3</sub> PQDs as a photocatalyst that could produce radicals under light irradiation and polymerize monomers. 2,2',5',2''-ter-3,4-Ethylenedioxothiophene (TerEDOT) was polymerized over CsPbI<sub>3</sub> PQDs with the help of 1,4-benzoquinone as the electron acceptor upon visible light

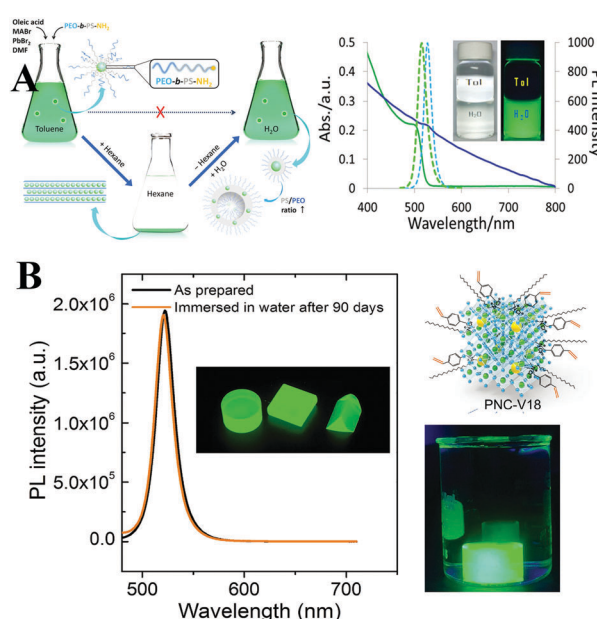


Fig. 20 (A, i) Schematic illustration of the synthesis and toluene-to-water phase transfer of PEO-*b*-PS-NH<sub>2</sub> grafted MAPbBr<sub>3</sub> QDs. (ii) UV-Vis absorption (solid line) and PL emission spectra (dashed line) of PQD@PS<sub>106</sub>-*b*-PEO<sub>45</sub> in toluene (green) and in water (blue). Inset: Photographs of an aqueous solution of PQD@PS<sub>58</sub>-*b*-PEO<sub>45</sub> in a glass vial filled with toluene (left) and the same vial illuminated with a 365 nm UV lamp (right). Reprinted with permission from ref. 348. Copyright 2018, The Royal Society of Chemistry. (B) PL spectra of MAPbBr<sub>3</sub>-V18-polymer composites before and after being immersed in water for 90 d. The insets are the photo of bulk material under UV light excitation and the illustration of V18 modified MAPbBr<sub>3</sub> PQDs, respectively. Reprinted with permission from ref. 332. Copyright 2017, Wiley-VCH.

irradiation. As a result, CsPbI<sub>3</sub> PQDs are encapsulated in the poly(3,4-ethylenedioxothiophene) (PEDOT) networks, and simultaneously the initial cubic structure is retained. Recently, Tan *et al.*<sup>353</sup> used CsPbBr<sub>3</sub> PQDs as the photoinitiator in the polymerization of vinyl monomers. Upon white light illumination, polymer chains grow on the surface of PQDs directly, which results in the individually encapsulated PQDs@polymer nanoparticles with monodisperse core–shell structure (Fig. 21A).

Aside from the perovskite–polymer films and monoliths, perovskite–polymer nanocomposites also contribute to the enhanced stability owing to the compact encapsulation. Moreover, the monodisperse nanocomposites offer the possibility for cell imaging which is not feasible with bulk materials. In this respect, Fu and co-workers<sup>354</sup> developed a room-temperature solution self-assembly approach to synthesize polyvinylpyrrolidone (PVP)-capped colloidal CsPbX<sub>3</sub> nanocrystals (NCs) and embedded the NCs in polystyrene microhemispheres (MHSs) by assembling PS chains on NCs. The obtained luminescent NCs@MHSs with diameters of  $4 \pm 1 \mu\text{m}$  exhibit high water stability and nontoxicity, and can be employed as probes for

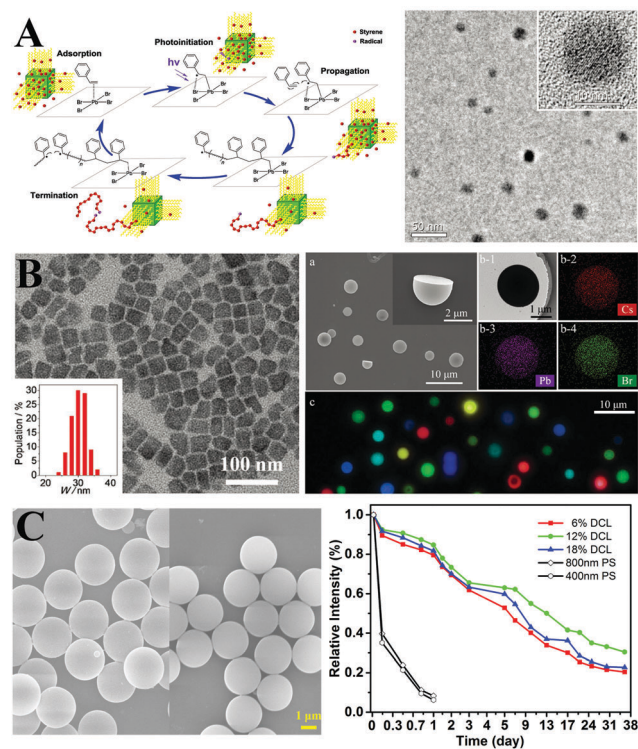


Fig. 21 (A) Proposed reaction mechanism (left) of the perovskite photo-activated polymerization of styrene and TEM and HRTEM images (right) of perovskite–polystyrene nanocomposites. Reprinted with permission from ref. 353. Copyright 2018, Wiley-VCH. (B) TEM images of PVP-capped PQDs (left), and (right) SEM images of CsPbBr<sub>3</sub> NCs@MHSs, elemental mapping of single CsPbBr<sub>3</sub> NCs@MHSs, and the fluorescence image of a mixture of neat and mixed-halide NC-tagged beads emitting single-color signals at 429, 455, 490, 512, 543, 581, and 642 nm. (C) SEM image of pure polymer spheres (left) with a size of  $3 \mu\text{m}$  and PQDs@PS (right) composites. And PL spectra of CsPbBr<sub>3</sub> NCs packed into PS spheres with different degrees of crosslinking and different diameters. (B and C) Reprinted with permission from ref. 354 and 356. Copyright 2017, Wiley-VCH.

cell imaging (Fig. 21B). Li and coworkers<sup>355</sup> prepared monodisperse  $\text{CsPbBr}_3@\text{PS}$  microspheres by electrospraying methods. PS encapsulation leads to the improved stability against anion exchange and water. Lin and coworkers<sup>356</sup> synthesized PQDs@PS composite beads *via* swelling the crosslinked beads in PQDs toluene solution and then shrinking in hexane. Further studies revealed that most PQDs might lie on the periphery of PS beads, and the small size (400 and 800 nm) of PS beads results in insufficient protection and limited water stability. The relatively large size (about 3  $\mu\text{m}$ ) of PS beads significantly enhanced the stability, especially, the PS beads with a hydrophobic surface well resisted aqueous, acid, and alkali solutions (Fig. 21C). The PQDs@PS retains a relatively high PL efficacy in such harsh environments, which can be applied as a cellular labelling agent and down-converter for pc-LEDs.

**3.3.2. Inorganics protection.** Although polymer encapsulation leads to a superior water resistance property, the poor thermal stability limits the further applications. Particularly, the polymer matrices degrade together with the loss of organic ligands of the perovskite surface under a relatively high temperature, which leads to irreversible PL quenching. By contrast, inorganics are generally mechanically robust and highly thermal resistant. Encapsulation of PQDs in inorganic matrices can be an effective strategy to protect PQDs.

**Silica coating.** Silica is chemically stable and transparent in the whole visible region that does not bring in changes in the optical properties of luminescent materials but can protect materials against moisture-induced damage. Silica-coating has been widely used in the lanthanide-doped upconversion nanoparticles,<sup>357</sup> traditional QDs,<sup>358</sup> magnetic nanoparticles,<sup>359</sup> etc. However, one primary problem with the silica coating for PQDs is that in a typical silica coating process *via* Stöber<sup>360</sup> or reverse microemulsion methods,<sup>361</sup> one inevitably uses tetraethyl orthosilicate (TEOS) as the precursor which decomposes in a strong alkaline alcohol solution. The coating of silica layers on PQDs is nearly impossible since the perovskite decomposes under such conditions before silica formation. There are three alternative methods available to overcome this problem: (1) using a pre-synthesized porous silica material; (2) selecting other precursors as silica sources; (3) altering the synthetic conditions for silica formation.

Liu *et al.*<sup>109</sup> firstly blended pre-synthesized  $\text{CsPbBr}_3$  PQDs with silica spheres with a pore size of 12–15 nm. After integrating PQDs into mesoporous silica, the obtained composites show enhanced thermal stability and photostability (Fig. 22A). Kovalenko *et al.*<sup>362</sup> infiltrated  $\text{CsPbBr}_3$  precursor solutions into mesoporous silica, and removal of solvents by baking resulted in the formation of PQDs in the silica pores. Yamauchi *et al.*<sup>363</sup> prepared  $\text{MAPbBr}_x\text{I}_{x-3}$  PQDs inside the mesoporous silica. Quantum confinement was observed by tuning the size of the QDs by altering the pore size of the silica templates (Fig. 22B). They further used gyroidal mesoporous silica<sup>364</sup> and mesoporous silica films<sup>365</sup> as templates for  $\text{MAPbX}_3$  growth. The 3D gyroidal template promotes the formation of monodispersed larger structures such as nanowires or nanorods due to the

easier escaping of solvents. On the other hand, by utilizing mesoporous silica films as the template,  $\text{CsPbBr}_3$  PQDs with 3.1 nm of average size formed within the pores. Owing to the strong quantum confinement effects, the composite films show blue-shift in PL emission together with increased PL QYs in comparison with the bulk materials.

Li *et al.*<sup>188</sup> employed tetramethyl orthosilicate (TMOS) as the silica precursor, which is more sensitive to water and easily hydrolyzed in a moisture condition than TEOS. The silica barriers formed on the  $\text{MAPbBr}_3$  PQDs in the waterless toluene (with a  $\text{H}_2\text{O}$  content of 0.0184%), protecting  $\text{MAPbBr}_3$  PQDs against moisture-induced degradation (Fig. 22C). Yin and coworkers<sup>77</sup> prepared isolated  $\text{CsPbX}_3/\text{SiO}_2$  Janus nanoparticles *via* a water-triggered transformation process combined with a sol-gel protocol (Fig. 22D). The PL intensity of PQDs declined to 85% upon continuous illumination, whereas the  $\text{CsPbX}_3/\text{SiO}_2$  Janus nanoparticles preserve the value of 98%. Jang *et al.*<sup>366</sup> employed perhydropolysilazane (PHPS) as a silica precursor. The silica formed on the  $\text{CsPbX}_3$  PQDs by curing in a moisture condition. The formation of silica barriers provides good thermal stability and chemical stability for PQDs. Leng and coworkers<sup>367</sup> constructed an amorphous silica layer by inserting TEOS into freshly synthesized  $\text{CsPbBr}_3$  PQDs. The silica layer formed on the PQDs rapidly under high temperature. The obtained  $\text{CsPbBr}_3-\text{SiO}_2$  composites present enhanced photostability, nonblinking optical properties, and improved PL performance. Recently, monodisperse  $\text{CsPbBr}_3@\text{SiO}_2$  core-shell nanoparticles have been synthesized by manipulating synthetic conditions such as temperature, precursors, and pH.<sup>368,369</sup> Compared with the large-sized aggregates, the ultrastable  $\text{CsPbBr}_3@\text{SiO}_2$  nanoparticles show potential in high-quality film applications, cell imaging, etc.

Zeng and coworkers<sup>370</sup> reported that, in addition to silica coating, anchoring PQDs on silica surface can also improve the stability. The anchoring-induced isolation prevents the PQDs contacting each other, which limits the possibility of crystal regrowth (Fig. 22E). The obtained PQDs-SiO<sub>2</sub> composites show excellent stability against light irradiation and air damage. After 40 d storage in ambient air, the PL intensity did not change as revealed by fluorescence spectrophotometric detection.

When referring to the anchoring effects, some reports comment that the nanoparticle anchoring on PQDs also contributes to the stability. Zhou *et al.*<sup>371</sup> synthesized  $\text{CsPbX}_3/\text{ZnS}$  heterostructures by anchoring ZnS nanoparticles on the PQDs' surface. ZnS anchoring results in rich electronic properties as confirmed by DFT calculations, which enhanced the chemical stability. Kamat *et al.*<sup>372</sup> prepared a Au- $\text{CsPbBr}_3$  hybrid nanosystem by anchoring Au nanoparticles on  $\text{CsPbBr}_3$ . An excess of Au anchoring leads to ePL quenching, whereas an appropriate Au-anchoring can improve the brightness of PQDs.<sup>373</sup>

**Porous materials coating.** As can be seen from the silica coating, many efforts have been devoted into integrating PQDs into as-prepared mesoporous SiO<sub>2</sub>. Direct growth of SiO<sub>2</sub> protecting layers on PQDs is somewhat challenging, because the optical performance would be deteriorated due to the harsh synthetic

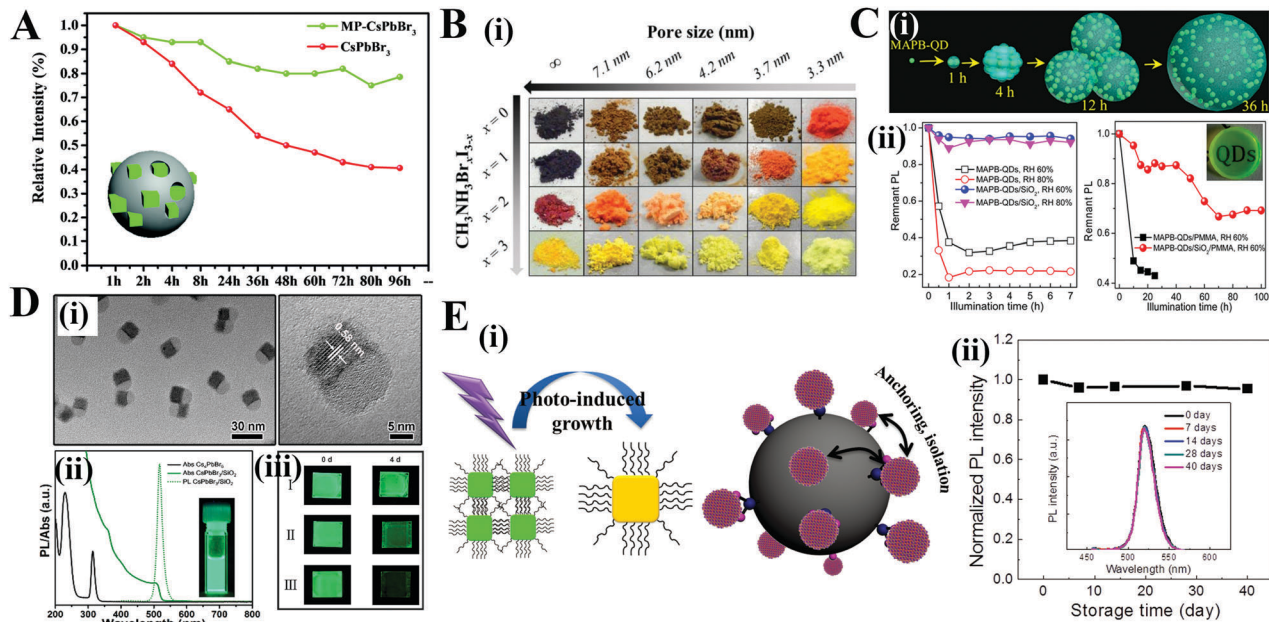


**Fig. 22** (A) Change of PL intensity as a function of UV illumination time of CsPbBr<sub>3</sub>-SiO<sub>2</sub> and CsPbBr<sub>3</sub>. The inset is the illustration of mesoporous silica spheres embedded with CsPbBr<sub>3</sub> PQDs. Reprinted with permission from ref. 109. Copyright 2016, Wiley-VCH. (B) Photographs of the mesoporous silica powders after impregnation and crystallization. Reprinted with permission from ref. 363. Copyright 2016, American Chemical Society. (C) MAPbBr<sub>3</sub>-SiO<sub>2</sub>: (i) schematic of the MAPbBr<sub>3</sub>-SiO<sub>2</sub> nanocomposites' formation process with increasing reaction time. (ii) Photostability of the MAPbBr<sub>3</sub> (left) and MAPbBr<sub>3</sub>-SiO<sub>2</sub> powders and their films with different RH values (right) under 470 nm LED light illumination. Inset: Optical image of the MAPbBr<sub>3</sub>-SiO<sub>2</sub>-PMMA film. Reprinted with permission from ref. 188. Copyright 2016, American Chemical Society. (D) CsPbBr<sub>3</sub>/SiO<sub>2</sub> Janus: (i) TEM image of the obtained CsPbBr<sub>3</sub>/SiO<sub>2</sub> Janus NCs. (ii) Absorption and PL spectra ( $\lambda_{\text{exc}} = 380$  nm) of pristine Cs<sub>4</sub>PbBr<sub>6</sub> NCs (black solid line) and CsPbBr<sub>3</sub>/SiO<sub>2</sub> NCs. The inset photograph shows a strong green PL emission under UV light ( $\lambda = 365$  nm). Reprinted with permission from ref. 77. Copyright 2017, American Chemical Society. (E) CsPbBr<sub>3</sub> QDs/A-SiO<sub>2</sub> composites: (i) schematic illustration of photo-induced regrowth of PQDs (left) and the isolation effect of PQDs on silica sphere surface (right). (ii) Material stability after storage without any protection. Reprinted with permission from ref. 370. Copyright 2017, Wiley-VCH.

environment and time-consuming formation process for the protective layer. And a fast formation of the protective layer leads to strong phase separation between the perovskite and the protective layer. Accordingly, introducing PQDs into pre-synthesized porous materials is relatively attainable.

The idea of embedding perovskites into mesoporous Al<sub>2</sub>O<sub>3</sub><sup>374</sup> and TiO<sub>2</sub><sup>375</sup> to enhance their stability has been investigated in the PV technology. Ye *et al.*<sup>376</sup> infused Cs<sup>+</sup> into zeolites to substitute Na<sup>+</sup> in the pore by ion-exchange reaction. Then, Cs<sup>+</sup> cations react with PbBr<sub>2</sub>, and form PQDs inside the zeolite pores (Fig. 23A). Hierarchical CaF<sub>2</sub> matrices also can be used to encapsulate PQDs.<sup>377</sup> The outstanding PL performance of pristine PQDs such as high brightness, high color purity, and quantum confinement effects is well preserved. Additionally, the co-doping of Ce<sup>3+</sup>/Tb<sup>3+</sup> into CaF<sub>2</sub> exhibits strong green light upon UV excitation. Thus, the luminescent CaF<sub>2</sub> matrices not only protect PQDs against environment-induced decomposition but also enrich their emitting colors (Fig. 23B). Hou and coworkers<sup>378</sup> utilized magnesium silicate hollow porous spheres to encapsulate MAPbX<sub>3</sub> PQDs. The strategy was demonstrated to be useful for multicolor displays, for which the obtained composites show tunable emission and enhanced thermal- and photo-stability.

As one of the famous porous material families, metal-organic frameworks (MOFs) with tunable pore size hold great potential for encapsulation of perovskites. Zhang and coworkers<sup>379</sup>

firstly employed oriented MOF films as template for the growth of MAPbI<sub>2</sub>X PQDs. The ultrasmall PQDs formed on introducing perovskite precursors into MOF pores. Further studies revealed that the PQDs in MOF films are environmentally stable and insensitive to air exposure. Li *et al.*<sup>380</sup> synthesized invisible and printable Pb-MOF. By MAX-triggering, luminescent MAPbX<sub>3</sub> formed in the Pb-MOF matrix. Interestingly, the PL of the MAPbX<sub>3</sub>@MOF is reversible by environmental stimuli in response to encryption and decryption processes, which indicates that MAPbX<sub>3</sub>@MOF composites can act as a smart luminescent system for application regarding confidential information (Fig. 23C).

**Salt coating.** Encapsulation in a dense inorganic ionic salt matrix also provides a robust surrounding for PQDs, which could greatly enhance the stability. Zhong *et al.*<sup>381</sup> proposed a one-step reprecipitation process for fabrication of MAPbBr<sub>3</sub>/NaNO<sub>3</sub> nanocomposites. The PL intensity of pristine PQDs dropped to a value of 10% after 14 h UV excitation, whereas the MAPbBr<sub>3</sub>/NaNO<sub>3</sub> composites preserved 80% of the initial value. Gaponik *et al.*<sup>112</sup> incorporated CsPbBr<sub>3</sub> PQDs into different KX salts under a high pressure (2.2 GPa) and showed that the CsPbX<sub>3</sub>/KX pellets with bright emission can be tuned covering the whole visible spectra. Li and coworkers<sup>382</sup> conducted an ion exchange of CsPbCl<sub>3</sub> PQDs to prepare CsPbBr<sub>3</sub>@NH<sub>4</sub>Br composites. The rich-bromide environments led to a sufficiently passivated surface of CsPbBr<sub>3</sub> PQDs, resulting in the decreased

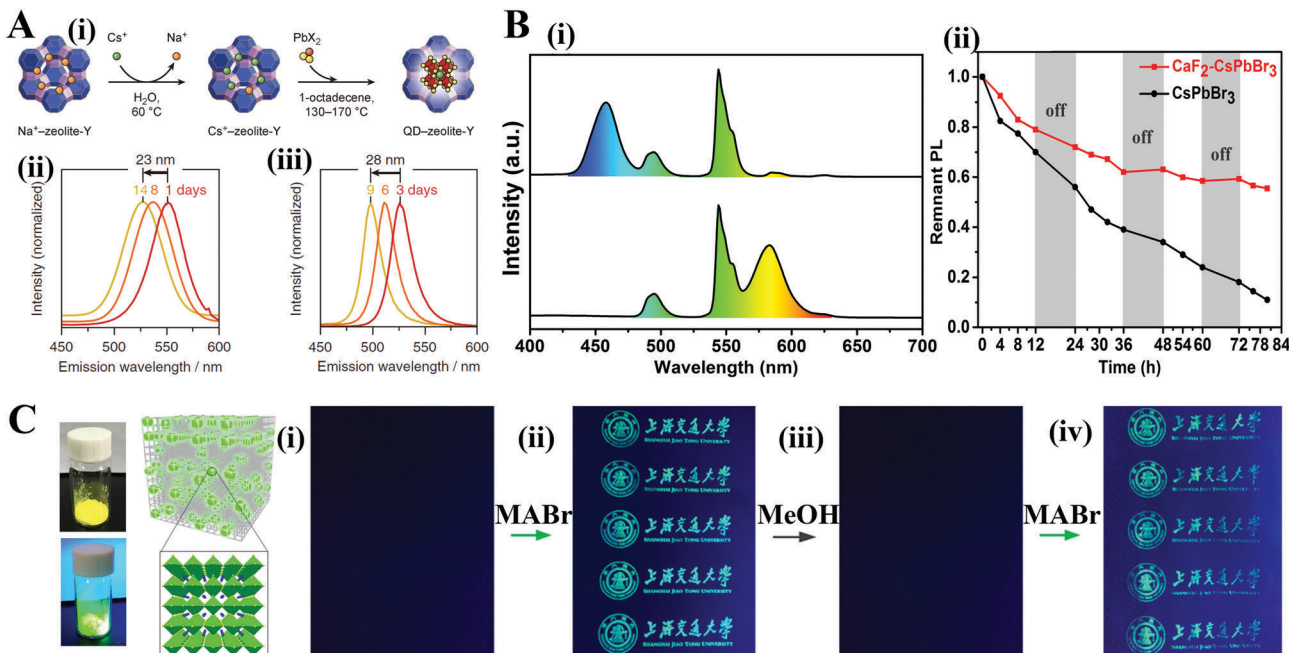


**Fig. 23** (A) CsPbX<sub>3</sub>-zeolite-Y: (i) schematic illustration of the two-step synthesis of CsPbX<sub>3</sub>-zeolite-Y composites. Spontaneous decomposition of CsPb(Br<sub>0.5</sub>I<sub>0.5</sub>)<sub>3</sub> evidenced by an emission blueshift over the course of multiple days for QDs embedded in zeolite-Y (ii) and bare QDs (iii). Reprinted with permission from ref. 376. Copyright 2017, Wiley-VCH. (B) CsPbX<sub>3</sub>-CaF<sub>2</sub>: (i) PL spectra of as-prepared CaF<sub>2</sub>:Ce/Tb-CsPbCl<sub>1.5</sub>Br<sub>1.5</sub> (top) and CaF<sub>2</sub>:Ce/Tb-CsPbBr<sub>1.5</sub>I<sub>1.5</sub> (bottom) excited at 306 nm. (ii) Photostability test of CaF<sub>2</sub>-CsPbBr<sub>3</sub> composites and pristine CsPbBr<sub>3</sub> PQDs. Reprinted with permission from ref. 377. Copyright 2018, Wiley-VCH. (C) MAPbX<sub>3</sub>@MOF: (A) schematic illustrations of the reversible on/off switching of the luminescence signal. (i) As-printed Pb-MOF on a commercial parchment paper. (ii) MABr treatment leads to the formation of luminescent MAPbBr<sub>3</sub>@Pb-MOF. (iii) The luminescence quenched after MeOH treatment. (iv) The luminescence can be recovered after MABr treatment. The left images are the illustration of MAPbBr<sub>3</sub> formed in the Pb-MOF matrix and their optical images under sunlight and UV lamp illumination. Reprinted with permission from ref. 380. Copyright 2017, Springer Nature.

surface trapping as well as enhanced stability towards water resistance (Fig. 24A). Upon water contact with the CsPbBr<sub>3</sub>@NH<sub>4</sub>Br composites, the NH<sub>4</sub>Br framework firstly dissolved in water and then released NH<sub>4</sub><sup>+</sup> and Br<sup>-</sup> ions, which cap the PQDs and make the perovskite isolated from water.

**Oxide coating.** Most inorganic oxides are highly robust. Oxides have been regarded as a practical alternative for coating PQDs. Buonsanti *et al.*<sup>383</sup> prepared CsPbBr<sub>3</sub>/AlO<sub>x</sub> composites *via* an atomic layer deposition (ALD) technique. By virtue of the low-temperature and fast ALD process, the amorphous alumina (AlO<sub>x</sub>) matrix grew on the perovskite directly, which forms a tight protection for CsPbBr<sub>3</sub> PQDs. The obtained CsPbBr<sub>3</sub>/AlO<sub>x</sub> composites show exceptional stability towards air, high-energy light irradiation, and thermal and water treatment (Fig. 24B). Zheng *et al.*<sup>384</sup> coated the TiO<sub>2</sub> shell on CsPbBr<sub>3</sub> PQDs by calcining the titanium precursor with CsPbBr<sub>3</sub> PQDs at 300 °C. The monodispersed CsPbBr<sub>3</sub>/TiO<sub>2</sub> nanocomposites preserve the initial characteristic including size, structure, and PL intensity even being immersed in water over three months (Fig. 24C).

**Core-shell structure.** Despite the fact that various strategies such as halide-rich surfaces, passivated ligands, polymer frameworks, and inorganic matrices have been developed as the protective shells for encapsulating PQDs, an ideal core-shell PQD structure similar to the monodisperse CdSe@ZnS

architecture is still highly expected. On the one hand, the compact shell seals the PQDs and prevents oxygen and water molecules from permeating into the perovskite cores, which ensures stability. On the other hand, the shell passivates the surface and reduces the nonradiative recombination at the surface defects. Moreover, such a thin shell minimizes the nonluminescent protective materials, which maximizes the PL performance.

Despite the fact that monodisperse perovskite-polymer core-shell structural nanocomposites (CsPbBr<sub>3</sub>@PS,<sup>353</sup> CsPbBr<sub>3</sub>@PS-*b*-P2VP<sup>347</sup>) at a single-particle level have been achieved, the thermal stability is still limited. The monodisperse CsPbBr<sub>3</sub>/TiO<sub>2</sub> nanocomposites seem to provide perfect protection, but most optical property is sacrificed during TiO<sub>2</sub> shell formation (calcination at 300 °C). Mathews *et al.*<sup>244</sup> prepared core-shell type MA-octylammonium lead bromide perovskite nanoparticles. Although it is difficult to obtain the direct evidence of the presence of the 2D perovskite shell, the improved stability implies the successful shell formation (Fig. 25A). Tian *et al.*<sup>385</sup> synthesized CsPbBr<sub>3</sub>@amorphous CsPbBr<sub>x</sub> (denoted as CsPbBr<sub>3</sub>@A-CsPbBr<sub>x</sub>) core-shell-type QDs (Fig. 25B). After A-CsPbBr<sub>x</sub> coating, the QDs show strong blue emission with PL QYs above 80%. Simultaneously, the A-CsPbBr<sub>x</sub> shell protects the CsPbBr<sub>3</sub> core against photooxidation. Recently, Li *et al.*<sup>386</sup> reported a controllable phase transformation from CsPbBr<sub>3</sub> to the CsPbBr<sub>3</sub>/Rb<sub>4</sub>PbBr<sub>6</sub> core/shell structure by postsynthetic rubidium oleate treatment of CsPbBr<sub>3</sub> PQDs. The robust Rb<sub>4</sub>PbBr<sub>6</sub> shells render

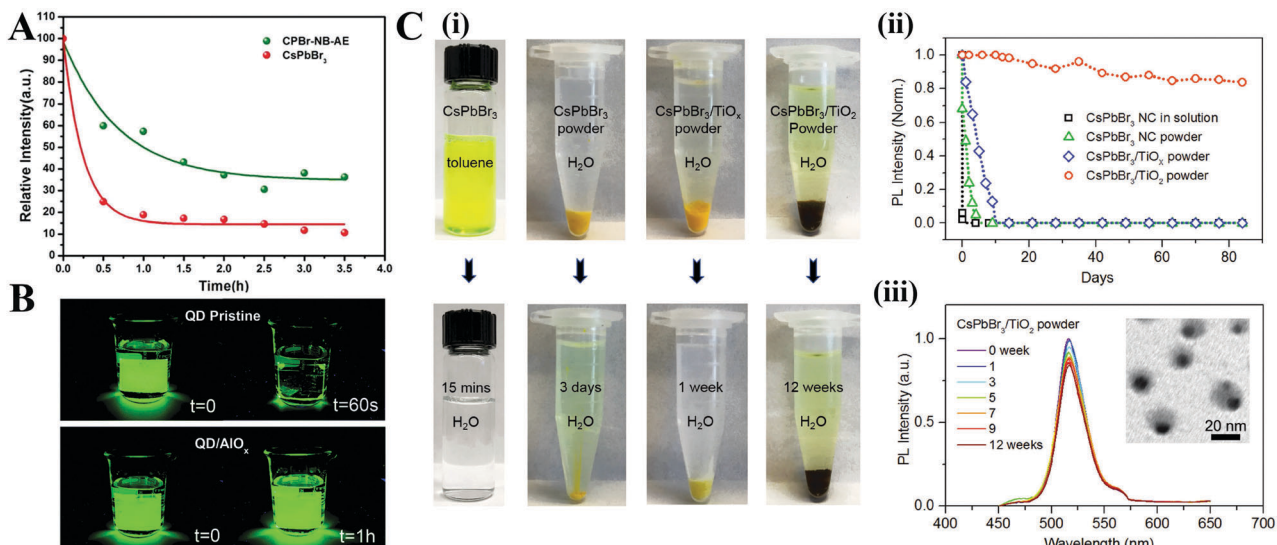


**Fig. 24** Water resistance test of (A) pristine CsPbBr<sub>3</sub>, CsPbBr<sub>3</sub>@NH<sub>4</sub>Br, and (B) pristine CsPbBr<sub>3</sub> QD films, and CsPbBr<sub>3</sub>/AlO<sub>x</sub>. (C) CsPbBr<sub>3</sub>/TiO<sub>2</sub>: (i) optical images of the fresh CsPbBr<sub>3</sub> PQDs in toluene, dried CsPbBr<sub>3</sub> powder in Milli-Q water, CsPbBr<sub>3</sub>/TiO<sub>x</sub> composite in water, and CsPbBr<sub>3</sub>/TiO<sub>2</sub> NCs in water (top) and those samples in water with different extended time under ambient conditions (bottom); (ii) the relative PL intensity of CsPbBr<sub>3</sub> NCs (without precipitation), dried CsPbBr<sub>3</sub> powder, CsPbBr<sub>3</sub>/TiO<sub>x</sub> powder, and CsPbBr<sub>3</sub>/TiO<sub>2</sub> powder after immersing in water; (iii) the relative PL intensity of CsPbBr<sub>3</sub>/TiO<sub>2</sub> NCs after immersing in water (0–12 weeks), the inset shows a TEM image of CsPbBr<sub>3</sub>/TiO<sub>2</sub> NCs after immersing in water for 12 weeks. (A) Reprinted with permission from ref. 382. Copyright 2017, The Royal Society of Chemistry. (B and C) Reprinted with permission from ref. 383 and 384. Copyright 2017, Wiley-VCH.

ultrahigh stability to CsPbBr<sub>3</sub> cores. The PL intensity of CsPbBr<sub>3</sub>/Rb<sub>4</sub>PbBr<sub>6</sub> nanocrystals remains above 90% of the original emission after 42 h of light illumination, which is superior to that of the commercial CdSe/CdS QDs (Fig. 25C).

**Endotaxial systems.** Inspired by the successful synthesis of endotaxial systems,<sup>387</sup> endotaxy with the same chemical elements but in a different crystal structure could cover the PQDs and prevent their agglomeration. Cs<sub>4</sub>PbBr<sub>6</sub> and CsPb<sub>2</sub>Br<sub>5</sub> composed of the same chemical elements as the CsPbBr<sub>3</sub> perovskite could provide endotaxy to CsPbBr<sub>3</sub>. Among them, the tetragonal phase CsPb<sub>2</sub>Br<sub>5</sub> with a sandwich structure consists of Cs<sup>+</sup> and (Pb<sub>2</sub>Br<sub>5</sub>)<sup>−</sup> layers, which is quite different from the 3D structure of CsPbBr<sub>3</sub> perovskites.<sup>23,388</sup> Nevertheless, their optical properties are similar: narrow bandwidth, high bright green fluorescence, tunable bandgap, etc. The fabrication of binary CsPbBr<sub>3</sub>–CsPb<sub>2</sub>Br<sub>5</sub> perovskites has attracted extensive interest.<sup>389–392</sup> The presence of CsPb<sub>2</sub>Br<sub>5</sub> can increase the PL lifetime of CsPbBr<sub>3</sub> by decreasing nonradiative energy transfer to the trap states.<sup>389</sup>

As for the Cs<sub>4</sub>PbBr<sub>6</sub>, the PbBr<sub>6</sub><sup>4−</sup> octahedra are completely decoupled in all dimensions, which is often referred as the zero-dimensional (0D) perovskite.<sup>393–395</sup> The rhombic prism hexabromide Cs<sub>4</sub>PbBr<sub>6</sub> with individual PbBr<sub>6</sub><sup>4−</sup> clusters has a wide band gap of 3.95 eV.<sup>393</sup> Additionally, the 0D perovskites present much better stability than the 3D perovskites. It is known that the 3D CsPbI<sub>3</sub> rapidly degrades into a 1D orthorhombic structure within several days, while Cs<sub>4</sub>PbI<sub>6</sub> maintains the original hexagonal phase under ambient conditions over one month without any sign of variation.<sup>393</sup> Hence, the 0D Cs<sub>4</sub>PbX<sub>6</sub> can be regarded as the best host for perovskite endotaxial systems.

Interestingly, obtaining pure phase Cs<sub>4</sub>PbBr<sub>6</sub> is always difficult since it usually coexists with CsPbBr<sub>3</sub>. And at an early stage, a stable green light of Cs<sub>4</sub>PbBr<sub>6</sub> under UV excitation was observed. Therefore, the 0D Cs<sub>4</sub>PbBr<sub>6</sub> has been regarded as a highly efficient, highly stable luminescent phosphor and superior to its 3D polymorphs. Recent studies revealed that the green PL in Cs<sub>4</sub>PbBr<sub>6</sub> is attributed to the presence of a small amount of CsPbBr<sub>3</sub> NCs, but the content of CsPbBr<sub>3</sub> was too low to be detected by the XRD technique.<sup>396</sup>

Sargent *et al.*<sup>397</sup> developed a theoretical model showing that the lattice of cubic-phase CsPbBr<sub>3</sub> PQDs can well match the hexagonal-phase Cs<sub>4</sub>PbBr<sub>6</sub> matrix. They further synthesized the CsPbBr<sub>3</sub>–Cs<sub>4</sub>PbBr<sub>6</sub> endotaxial system as confirmed by XRD and high resolution transmission electron microscopy (HRTEM) studies. The bulk CsPbBr<sub>3</sub>–Cs<sub>4</sub>PbBr<sub>6</sub> composites have reached PL QYs of 90% owing to the improved passivation and well dispersibility in the Cs<sub>4</sub>PbBr<sub>6</sub> matrix (Fig. 26A). Further research revealed that embedding CsPbBr<sub>3</sub> PQDs into the Cs<sub>4</sub>PbBr<sub>6</sub> matrix could effectively enhance the oscillator strength, which may help radiative decay which competes with the Auger process and improve the performance of PeLED devices.<sup>398</sup> Sun and coworkers<sup>399</sup> demonstrated that the ligand-free CsPbBr<sub>3</sub>–Cs<sub>4</sub>PbBr<sub>6</sub> composites ensure thermal stability and high temperature operation, which enable temperature-insensitive two-photon lasers. Zhong *et al.*<sup>400</sup> synthesized centimeter-sized CsPbBr<sub>3</sub>–Cs<sub>4</sub>PbBr<sub>6</sub> composites via an HBr-assisted slow cooling strategy. The obtained composites show PL QYs as high as 97%, and can be used as high-efficiency phosphors in wide color gamut pe-LEDs. Wang *et al.*<sup>401</sup> prepared CsPbBr<sub>3</sub>–Cs<sub>4</sub>PbBr<sub>6</sub> nanocrystals with PL QYs of 83%. The CsPbBr<sub>3</sub> PQDs were homogeneously embedded in the Cs<sub>4</sub>PbBr<sub>6</sub>

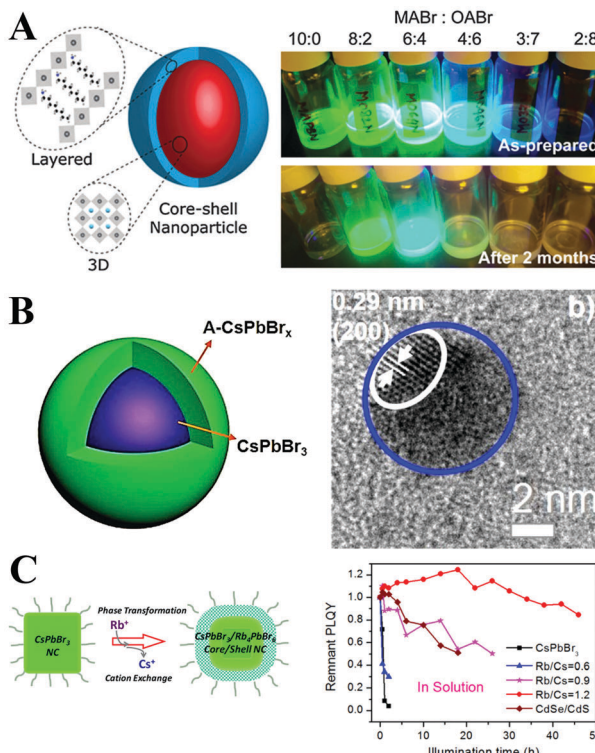


Fig. 25 (A) Schematic showing the core–shell type layer growth of octylammonium lead bromide nanomaterials over MAPbBr<sub>3</sub> NPs (left) and photographic images of mixed organolead bromide perovskite NPs with different MABr:OABr ratios in toluene solution under UV exposure over different time intervals (right). Reprinted with permission from ref. 244. Copyright 2016, The Royal Society of Chemistry. (B) Diagrammatic sketch of CsPbBr<sub>3</sub>@A-CsPbBr<sub>x</sub> QDs (left) and their corresponding HRTEM (right) figures. Reprinted with permission from ref. 385. Copyright 2017, American Chemical Society. (C) Diagrammatic sketch of CsPbBr<sub>3</sub>@Rb<sub>4</sub>PbBr<sub>6</sub> NCs (left) and their photostability (right). Reprinted with permission from ref. 386. Copyright 2018, American Chemical Society.

matrix, which ensures the PL property and stability. Li *et al.*<sup>402</sup> further optimized the synthesis and achieved the preparation of CsPbX<sub>3</sub>/Cs<sub>4</sub>PbX<sub>6</sub> nanocrystals with core–shell structure in a single particle level. Sun *et al.*<sup>403</sup> developed a scalable and high-yield recipe for the synthesis of Cs<sub>4</sub>PbBr<sub>6</sub>/CsPbBr<sub>3</sub> composites with PLQYs of 95% (Fig. 26B). Overall, CsPbX<sub>3</sub>–Cs<sub>4</sub>PbX<sub>6</sub> endotaxial systems hold great promise for photonic applications due to the superior optical property and stability.

### 3.3.3. Multiple protections

**Multi-step treatment.** The stability of PQDs can be further enhanced by applying multiple protections. Liu *et al.*<sup>404</sup> reported a three-step treatment of CsPbBr<sub>3</sub> PQDs to improve the stability including (1) SDDA passivation, (2) mesoporous silica integration, and (3) PMMA coating. The final products present a high PLQY of 63% as well as high thermal and water resistance. Li *et al.*<sup>405</sup> synthesized CsPbBr<sub>3</sub>–silica/alumina monoliths by employing compact SiO<sub>2</sub> and Al<sub>2</sub>O<sub>3</sub> layers to coat CsPbBr<sub>3</sub> PQDs. Incorporation of silica and alumina layers greatly decreases the pinhole of films and minimizes water and oxygen permeability (Fig. 27A). Zeng and coworkers<sup>406</sup> proposed a double-protection for CsPbBr<sub>3</sub> PQDs by Cs<sub>4</sub>PbBr<sub>6</sub>

crystalline structures and SiO<sub>2</sub> microspheres. The CsPbBr<sub>3</sub>@Cs<sub>4</sub>PbBr<sub>6</sub>@SiO<sub>2</sub> composites show reversible fluorescence response between 30 and 150 °C. The thermal-modulated PL on/off function indicates their potential in thermal anti-counterfeiting. Recently, Xia *et al.*<sup>407</sup> found that the surface defective layer of CsPbX<sub>3</sub> PQDs can be dissolved in water by postsynthetic water treatment. Therefore, after separating the supernatant CsPbX<sub>3</sub> PQDs hexane solution from water, their PL QYs are drastically improved. A small fraction of water still dissolved in the hexane solution, hence, they further used TMOS to run out of the residual water and form silica shell on the PQDs (Fig. 27B).

**Single-step treatment.** A multi-step protection process can further improve the stability of PQDs. However, some stabilization processes can also damage luminescent PQDs. As a result, the stability is enhanced but the PL efficiency is sacrificed after tedious multi-step treatments. It is necessary to highlight some studies of applying protection materials as a function of both surface passivation and encapsulation by a single-step treatment. The synergistic effects could maintain the optical property and endow PQDs with high stability, indicating the superiority than a single protection process.

Zhang *et al.*<sup>74</sup> used APTES to passivate the surface of PQDs, and simultaneously, the ligand layer formed a cross-linked silica layer over the CsPbX<sub>3</sub> PQDs (Fig. 28A). The single protection material enables highly stable and efficient perovskite composites by passivating the surface and covering PQDs from contacting the environment directly. Combined with XPS and <sup>1</sup>H NMR results, it is reasonable to speculate that the Pb(II) on the surface of QDs covalently coordinated with the amine group of APTES molecules.<sup>306</sup> González-Pedro and coworkers<sup>408</sup> found that the PL of PQDs can be recovered after postsynthetic treatment with APTES. Further investigations revealed that the recovered PL originated from the ligands preferentially attached to the PQD surface through hydrogen bonds formed between silanol groups and bromide dangling bonds. Liu and coworkers<sup>409</sup> employed reactive methacrylic acid (MAA) to passivate the CsPbX<sub>3</sub> surface. UV-induced polymerization was conducted based on the free double bonds on the perovskite surface with POSS-appended methacrylate (MA-POSS), methyl methacrylate (MMA) monomer, and AIBN initiator. The copolymerization products can serve as luminescent inks and water-resistant films for pc-LEDs (Fig. 28B). Do *et al.*<sup>410</sup> employed a novel inorganic polymer matrix, a dual-silicon nitride and silicon oxide nitride polymer, polysilazane (PSZ), to passivate the surface of PQDs and encapsulate CsPbBr<sub>3</sub>. The bifunctional inorganic PSZ layer can improve the thermal stability and maintain the PL efficiency of PQDs.

### 3.4. Device encapsulation

LED device encapsulation is a process of combining the InGaN chip and other packaging materials including phosphors and encapsulants to fabricate the final devices.<sup>66,70</sup> Device encapsulation not only plays a crucial role in mechanical protection but also greatly affects the device performance.<sup>411</sup>

**3.4.1. Encapsulants.** Generally, silicone based materials are used for encapsulating pc-LEDs owing to the high optical

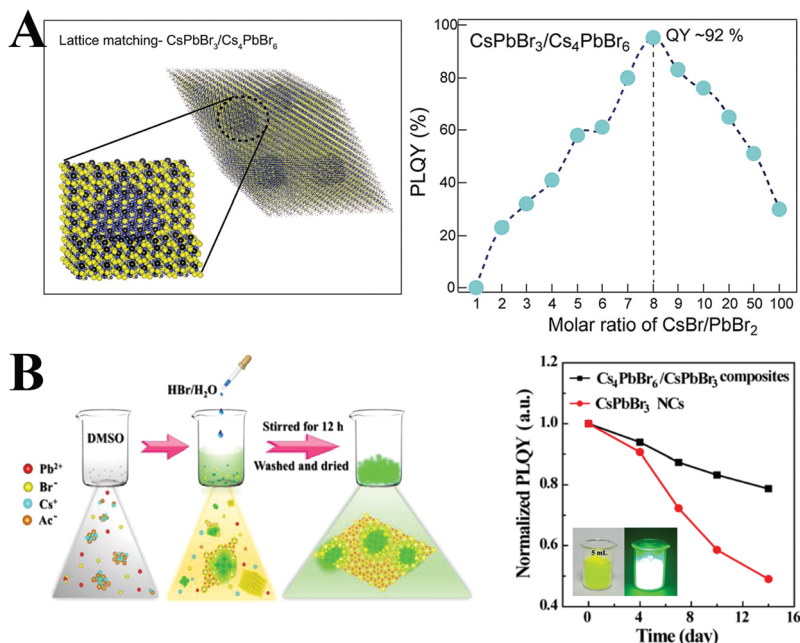


**Fig. 26** (A) Theoretical model for the material with various cubic perovskite inclusions in each rhombic prism matrix (left), and PLQYs of materials resulting from different ratios of CsBr and PbBr<sub>2</sub> (right). Reprinted with permission from ref. 397. Copyright 2017, Wiley-VCH. (B) Schematic illustration of the room-temperature self-assembly process for the product of the Cs<sub>4</sub>PbBr<sub>6</sub>/CsPbBr<sub>3</sub> composites (left), and PLQYs of Cs<sub>4</sub>PbBr<sub>6</sub>/CsPbBr<sub>3</sub> composites and CsPbBr<sub>3</sub> NCs exposed to air for different times (right). Reprinted with permission from ref. 403. Copyright 2018, American Chemical Society.

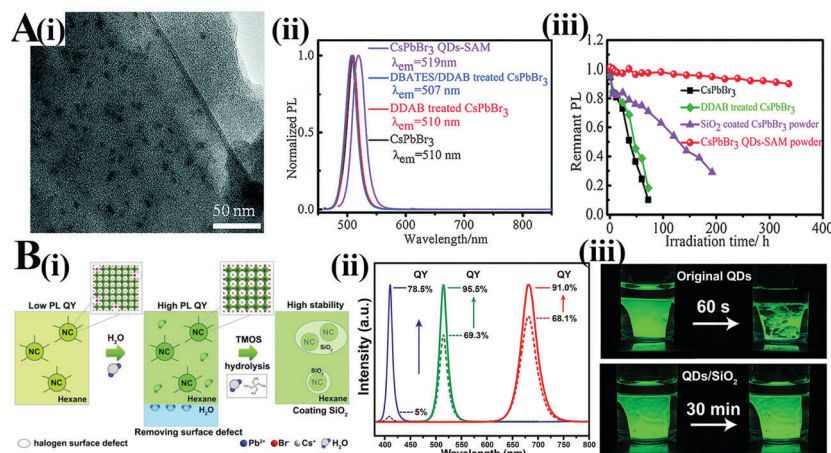


**Fig. 27** (A) CsPbBr<sub>3</sub> QDs-SAM: (i) The TEM image of CsPbBr<sub>3</sub> QDs-SAM. (ii) Evolution of PL spectra of CsPbBr<sub>3</sub> PQDs after adding DDAB and DBATES. (iii) Photostability of the CsPbBr<sub>3</sub> QDs-SAM powder, SiO<sub>2</sub> coated CsPbBr<sub>3</sub> PQDs powder, DDAB treated CsPbBr<sub>3</sub> PQDs, and bare PQDs under illumination with a 470 nm LED light. Reprinted with permission from ref. 405. Copyright 2017, Wiley-VCH. (B, i) Illustration of the water treatment and silica encapsulation process of CsPbBr<sub>3</sub> PQDs. (ii) PL emission spectra of the untreated (dashed line) and water treated (solid line) CsPbCl<sub>3</sub> (blue), CsPbBr<sub>3</sub> (green), and CsPbI<sub>3</sub> (red) PQDs. (iii) Optical images of pristine CsPbBr<sub>3</sub> and CsPbBr<sub>3</sub>/SiO<sub>2</sub> films under UV illumination ( $\lambda = 365$  nm) after 30 min of soaking in water. Reprinted with permission from ref. 407. Copyright 2018, American Chemical Society.

transmittance in the visible region, water and thermal resistance, and a variety of cure and processing chemistry.<sup>412</sup> Silicone materials such as silicone resin [A and B (OE-6630,<sup>366</sup> OE-6631,<sup>109,356,377,404</sup> OE-6550,<sup>341</sup> and OE-6551<sup>107,305</sup>), Dow Corning Co.] and PDMS<sup>405</sup> are also widely used for encapsulating PQDs and perovskite nanocomposites in pc-LEDs device fabrication. It is worth noting that although free-standing perovskite composite films can be coated on the LED chips directly without additional device

encapsulation, additional coating of a silicone resin protective layer can significantly prolong the durability of light emitters under ambient air conditions due to the hydrophobic surface of silicone resin.<sup>413</sup> Nevertheless, the silicone resin encapsulants suffer from several shortcomings: (1) thermal stability; (2) anion exchange; (3) reabsorption; (4) compatibility.

As described above, thermal-induced PL quenching may arise from agglomeration and ligand loss. Homogeneously dispersing

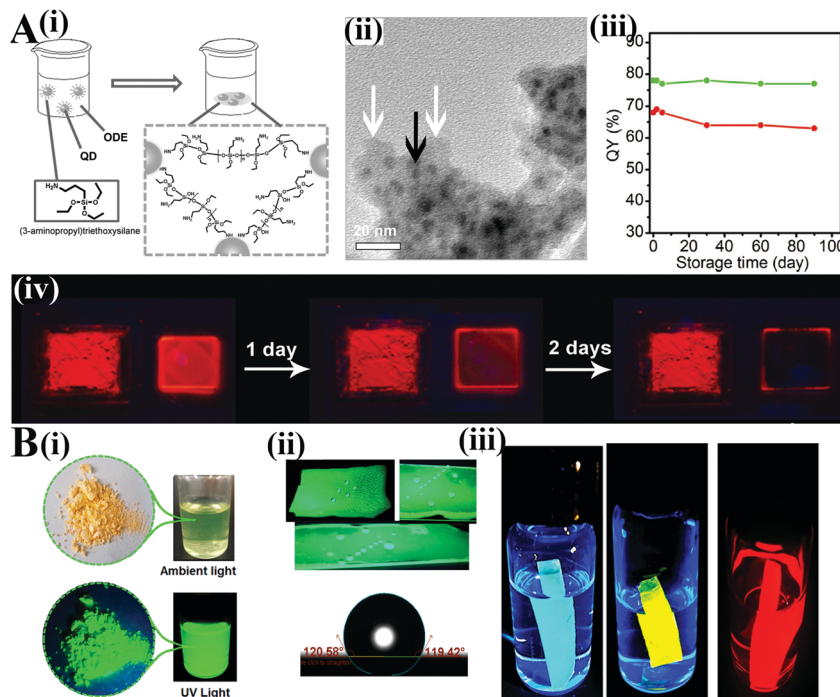


**Fig. 28** (A) QD/silica composites: (i) schematic illustration of formation of QD/silica composites. (ii) TEM images of CsPbBr<sub>3</sub>/silica composites. (iii) The PL QY stability of CsPbBr<sub>3</sub>/silica composites. (iv) The photographs of red QD/silica powder and the red OLA–QD film under UV light. Reprinted with permission from ref. 74. Copyright 2016, Wiley-VCH. (B) Characterization of PMPOPNC: (i) as-prepared powder of PMPOPNC under ambient light and UV light, respectively. (ii) Photos showing the hydrophobicity of the PMPOPNC film. (iii) Photographs of films of PMPOPNC–CsPb(Br/Cl)<sub>3</sub>, PMPOPNC–CsPb(Br/I)<sub>3</sub>, and PMPOPNC–CsPbI<sub>3</sub> taken under UV irradiation after immersion in water for 60 days. Reprinted with permission from ref. 409. Copyright 2018, American Chemical Society.

PQDs into some kinds of matrices can mitigate agglomeration. After separating PQDs from each other, the PL quenching is largely reversible below 450 K owing to the undamaged ligands, as confirmed by thermal cycling tests.<sup>220</sup> The recoverable PL allows for high temperature processing such as the thermal curing of silicone resin. However, most thermal curing of silicone resin occurs at ~420 K, which is close to the ligand loss temperature.

To minimize the thermal silicone curing-induced PL loss, some polymer matrices such as PMMA<sup>56</sup> with high transmittance as well as a lower curing temperature (about 350 K) or UV curable optical adhesives<sup>76,175</sup> hold great promise for perovskite-based device encapsulation. Employing transparent ceramics or glass ceramics to integrate phosphors, *i.e.* phosphor-in-glass (PiG), can be an effective strategy for device encapsulation.<sup>414</sup> PiG could provide excellent heat and moisture resistance for phosphors. Recently, stable PQDs-glass emitters were prepared by the melt-growth PiG technique.<sup>415–419</sup> The surrounded amorphous phosphate or borosilicate glass matrices greatly enhanced the stability towards water and oxygen exposure.

The fast ion-exchange takes place between two LHPs with varied halide components, which leads to the severe emission shift. Mixing green-emitting and red-emitting PQDs directly in the soft resin gel bring in the strong yellow-emitting PQDs.<sup>109</sup> To block the anion exchange, changing surface ligands or embedding PQDs in matrices is necessary. Additionally, individually cast thin films with different color emitting PQDs could also effectively block the ion exchange.<sup>336</sup>

Reabsorption is a common issue for all kinds of QDs. The narrow bandwidth leads to a low color rendering index (CRI) value; hence encapsulating various color-emitting QDs is imperative to improve the CRI value. However, owing to the relatively small Stokes shift (20–80 meV for CsPbBr<sub>3</sub>)<sup>420</sup>, these different color-emitting QDs suffer from severe reabsorption. Owing to the absorption spectra of red-emitting QDs covering the whole PL emission spectra of green-emitting QDs, the emitted green light would be reabsorbed by red-emitting QDs, which decreases the device performance. A multi-layer encapsulation technique was carried out to overcome the reabsorption. The red-emitting QDs/encapsulant were cast on the LED chips firstly, followed by the casting of green-emitting QDs/encapsulant. Thus the device performance can be significantly improved.<sup>164,400</sup>

Hydrophobic OA and OLA capped PQDs can homogeneously disperse in silicone resin due to the similar surface property, but PQDs with hydrophilic ligands such as PVP–PQDs cannot well disperse in silicone resin.<sup>413</sup> A similar agglomeration was observed when embedding TOP capped QDs into the PMMA matrix owing to the poor compatibility, which accelerates the PL quenching.<sup>421</sup> Thereby, selecting an appropriate encapsulant is important for improving device performance and duration.

**3.4.2. Encapsulation type.** Apart from the device encapsulant, one device-related instability should be pointed out: a large amount of heat generated from the p–n junction of the LED chip. About 40% of electrical energy is converted into thermal energy,

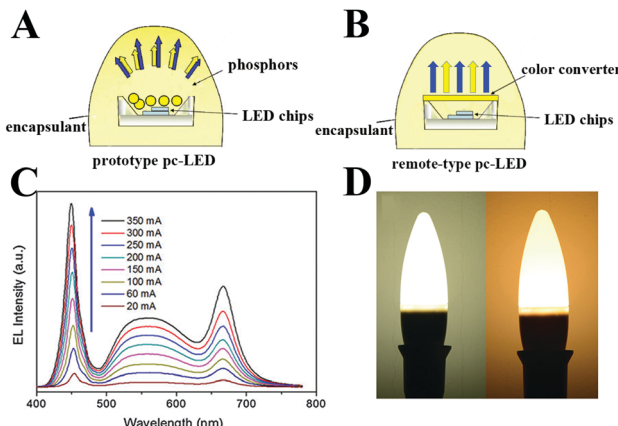


**Fig. 29** Schematic structure of prototype (A) and remote-type (B) pc-LEDs. (C) EL spectra of  $\text{CsPbBrI}_2$  PQD-modified pc-LEDs under various operational currents. (D) Photographs of pc-LEDs with and without the  $\text{CsPbBrI}_2$  QD film. (C and D) Reprinted with permission from ref. 422. Copyright 2016, The Royal Society of Chemistry.

which leads to a high chip junction temperature when working. In addition, a portion of heat generated from the absorbed light energy is lost through a nonradiative recombination process. An excessive high-temperature affects the light output of LED chips. Moreover, the PQDs are sensitive to heat, which further leads to an inferior device performance. Development of an efficient heat dissipation technology such as heat radiation fins and fins can decrease the working temperature for the LED device. In addition, the construction of a novel encapsulation approach can mitigate the thermal-induced decrease in device performance.

A typical device architecture of pc-LED is shown in Fig. 29A. As can be seen from prototype pc-LEDs, the heat is easily transferred from the chip to the color converter, and accumulated in the converter layer due to the low thermal conductivity as well as the poor heat dissipation of the encapsulant-air interface. In this respect, a remote-type device was constructed to mitigate the thermal-induced PL quenching. Wang and coworkers<sup>422</sup> prepared the red  $\text{CsPbBrI}_2/\text{PMMA}$  film and stocked on a  $\text{Y}_3\text{Al}_5\text{O}_{12}\text{:Ce}$  (YAG)-based PiG. The obtained bi-layered color converters were coupled with the blue chips to construct the remote-type white LEDs (wLEDs) (Fig. 29B). As expected, the luminescence intensity of PQDs increased along with the driven current increasing from 20 mA to 300 mA, which demonstrates the minimum thermal quenching by remote encapsulation (Fig. 29C and D). Zhang *et al.*<sup>74</sup> synthesized small sized PQDs and embedded them in the silica matrix. The high temperature spectra show that the PQDs/silica composites lost nearly all emission upon heating to 350 K due to the easily reuniting small PQDs. They adopted a remote phosphor configuration to separate them from the hot LED chips. The remote-type wLEDs show preferable stability. The PL intensity presented a slight change after the wLED functioned for 10 h.

#### 4. Application in pc-LEDs

Pc-LEDs are promising solid-state light sources and widely used in the fields of lighting and backlight down-converters for

liquid crystal displays (LCDs) owing to their low cost, high electro-optical conversion efficiency, and environmentally friendly characteristics.<sup>66,68,69</sup> The LED chip is a crucial component that can convert electricity into near UV or visible light. Owing to the highly reliable and low-cost InGaN chip, the LED chip has been widely recognized as an optimal light excitation source. Hence, utilizing an appropriate phosphor to convert the chip light greatly determines the performance of pc-LEDs.

Luminous efficacy (LE) is a quantitative measure of the ability of how well a light source produces visible light, which has been considered to be the foremost index for pc-LEDs. The luminous flux reflects the varying sensitivity of human eyes to different wavelengths of light, which is different from radiant flux, the measure of the total power of electromagnetic radiation (including infrared, ultraviolet, and visible light). The luminous efficacy is defined as

$$\phi_{\text{lum}} = \frac{\phi_V}{\phi_e} = \frac{\int_0^{\infty} K(\lambda) \phi_{V,\lambda} d\lambda}{\int_0^{\infty} \phi_{V,\lambda} d\lambda} \quad (10)$$

where  $\phi_V$ ,  $\phi_e$ ,  $\phi_{V,\lambda}$  and  $K(\lambda)$  correspond to the luminous flux, radiant flux, spectral radiant flux and spectral luminous efficacy, respectively. The standard luminosity function is normalized to a peak value of unity at 555 nm. Thereby, the combination of blue chip and yellowish phosphors usually results in an outstanding LE.

The CRI refers to the ability of a light source to reveal the colors of various objects faithfully in comparison with an ideal or natural light source. The color of objects is more faithful under a high CRI light source illumination. The CRI is associated with the spectrum of the light source. The CRI of sunlight is defined as 100, and the CRI of an incandescent lamp is close to 100, whereas the CRI of most pc-LEDs is around 80.<sup>423</sup> The CRI and LE are two independent parameters to evaluate the device performance, but a high CRI usually brings in a low LE.<sup>424</sup>

Correlated color temperature (CCT) is the temperature of an ideal black-body radiator that radiates light of a color comparable to that of the light source. As the temperature rises, the black body radiates from reddish, orange, white, and bluish white light. Therefore, the color of a black body can be simply described by absolute temperature. By analogy, the color of nearly Planckian light sources including a tungsten lamp and sunlight can be judged by their temperature. But for the light source spectra that are not Planckian, such as pc-LEDs, color temperature is not a well-defined attribute; the concept of CCT was developed to map such light sources. CCT over 5000 K is called cool white light, while lower CCT is called warm white light. In general, a warm white light can promote relaxation, which is more useful for lighting applications.

Optimizing the LE, CRI, and CCT is crucial for promoting their applications in lighting and displays. Incorporating an appropriate phosphor can greatly adjust these parameters of pc-LEDs. Fig. 30 demonstrates the evolution of general pc-LEDs for five generations. Most types of commercial LEDs consist of blue chips and yellow-emitting YAG:Ce<sup>3+</sup> phosphors, which are also named as the first generation of white-LEDs. However, excitation of the YAG:Ce<sup>3+</sup> phosphor produces a cold white light

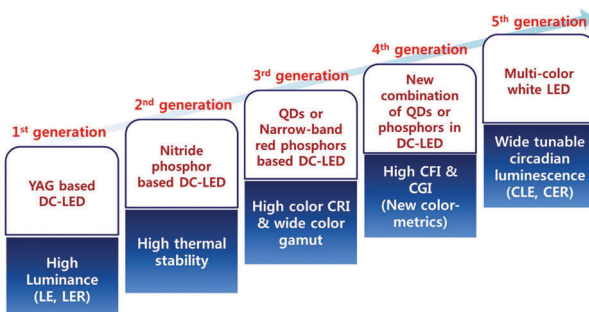


Fig. 30 Schematic diagram of the development approaches for the first through fifth generations for general WLED lighting devices. Reproduced with permission from ref. 87. Copyright 2017, Springer Nature.

with CCT above 5000 K and CRI below 80. To obtain warmer white light, red-emitting nitride phosphors with high thermal stability were explored. As a result, a warm white light with higher CRI can be obtained but the LE of the LED is slightly sacrificed. To meet the requirements for high-quality display applications, narrow-band  $K_2SiF_6:Mn^{4+}$  (KSF) was developed. KSF-based devices show wide color gamut in contrast to earlier generations of pc-LEDs. Recently, the Illuminating Engineering Society of North America proposed a new measurement system, a color fidelity index ( $CFI, R_f$ ) and a color gamut index ( $CGI, R_g$ ) as technical memorandum TM-30-2015 to accurately assess the color rendition and the color performances of fourth-generation pc-LEDs. However, it is found that trichromatic (blue, green, and red) warm white-light LEDs with a Ra score exceeding 90 are hard to reach a preferable  $R_f$  value over 90.<sup>86</sup> High-quality pc-LEDs should be able to produce white colors in the range of warm to cool. Recently, color-reproducible and healthy white-light LEDs were developed for next-generation lighting.<sup>87</sup> These smart white-light LEDs show tunable capability for the circadian effect, which is used for controlling melatonin secretion and more suitable for bio- and medical-related applications. The spectrum of QDs containing white-light LEDs should match daily variations in sunlight under a natural circadian rhythm.

Overall, PQDs can be employed as promising phosphors in pc-LEDs. But the poor stability limits their application. To enhance the stability of PQDs, the strategies including compositional engineering, surface engineering, matrix encapsulation and device encapsulation enable stable perovskite-based color converters for pc-LEDs. The reported improved stability and device performance are summarized in Table 2.

## 5. Conclusion and perspective

Lead halide perovskite quantum dots with intriguing optoelectronic properties have shown potential in a wide range of optoelectronic and photonic applications. Applying PQDs as phosphors for pc-LEDs to obtain excellent luminous efficacy and wide color gamut is very promising for next-generation high-quality lighting and vivid color display applications. At present, the poor stability is the major obstacle. There has been

tremendous progress in the past few years in understanding the degradation mechanisms and enhancing the stability of PQDs.

In this review, we summarized the degradation mechanism of perovskites in different conditions and tried to correlate the exterior-environment-induced factors with pc-LED device working mechanisms. Overall, ground-state PQDs are chemically stable, and only a small amount of the perovskite hydrated in normal conditions. The fluorescence loss is mainly ascribed to the agglomeration together with the increased surface trap. A better understanding of PL quenching promotes the development of various strategies for enhancing the stability of PQDs. According to the principle of these strategies, we can categorize them into four types.

The ionic radius plays a crucial role in the structural stability of perovskites. A large A cation cannot be accommodated into the interstice of the  $PbX_6$  framework, whereas a small A cation filling in the interstice will lead to the collapse of the 3D perovskite structure. Selecting appropriate or rationally mixing different A ions effectively stabilizes the 3D perovskite structure. Additionally, plenty of studies have shown that B-site doping can not only adjust the optoelectronic property but can also contribute to their stability. Although substitution of  $Pb^{2+}$  with some metal ions is possible to yield new deep defect states, an appropriate doping leads to improved optical performance and stability. Manipulating the perovskite composition can enhance the intrinsic stability of perovskites without sacrificing the photonic and electronic characteristics. At this stage, a full understanding of structural reorganization through component engineering at the atom level is highly expected.

The ill-passivated surface not only leads to the carriers' nonradiative recombination through surface localized states but is also susceptible to water and oxygen molecules. Moreover, conventional OA and OLA ligands are easily lost during purification. Hence, incorporation of suitable surface ligands to replace OA/OLA can increase the PL and stability of PQDs. In this respect, using branched molecules with large steric hindrance or strengthening the interactions between the surface and ligands has made a huge success.

Matrix encapsulation is the most widely used strategy to enhance the perovskite stability. Particularly, a compact protective layer covering PQDs could endow them with superior water resistance. Some polymer matrices with carboxyl or amine groups can passivate their surface and result in enhanced PL performances, but their thermal stability is still limited. Most inorganics are dense and thermally stable, but a controllable formation of an inorganic layer to cover PQDs is difficult because of the high synthetic temperature and relatively complicated synthetic conditions. Hence, more efforts should be devoted in this direction.

Device encapsulation is a process of integrating luminescent powders with LED chips. In addition to the powders, employing free-standing perovskite films is a more convenient strategy. Additional deposition of encapsulant over perovskite-polymer films can further improve the duration. Furthermore, adopting a suitable encapsulant can homogeneously disperse PQDs and prevent the agglomeration-induced PL quenching. Meanwhile, encapsulants

**Table 2** Summary of the PL properties and stability of perovskite composites, performance in p-WELEDs, and device lifetimes

Composites	PL QYs	Stability	Device structure	Luminous efficacy and device lifetime	Other index	Ref.
MAPbBr <sub>3</sub>	70%	40% (35 h, UV)	Blue chip/KSF (silicone)/MAPbBr <sub>3</sub> (PMMA)	48 lm W <sup>-1</sup> (4.9 mA) 24 lm W <sup>-1</sup>	130% NTSC (0.33, 0.27) (0.32, 0.26)	56
CsPbCl <sub>3</sub> :Ce,Eu			UV chip (365 nm)/CsPbCl <sub>3</sub> :Ce, Eu (PMMA)	Unchanged (working over 288 h)		292
MAPbBr <sub>3</sub>	72%	85% (120 h, UV)	Blue chip (455 nm)/MAPbBr <sub>3</sub> @POSS, KSF (silicone resin)	38 lm W <sup>-1</sup>	(0.30, 0.30)	83
CsPbX <sub>3</sub> @POSS	62% (green) 45% (red)	Stable in water over 10 weeks	Blue chip (455 nm)/CsPbBr <sub>3</sub> @POSS, CsPbBr <sub>1.2</sub> I <sub>1.8</sub> (silicone resin)	14.1 lm W <sup>-1</sup>	(0.349, 0.383)	107
MAPbX <sub>3</sub> /SiO <sub>2</sub>	56% (blue) 95% (green) 70% (red)	96% (72 h, air) 66% (30 min, 60 °C)	Blue chip (447 nm)/CsPbBr <sub>3</sub> /SiO <sub>2</sub> CsPbI <sub>1.5</sub> B <sub>3</sub> SiO <sub>2</sub> (PS)	54 lm W <sup>-1</sup>	(0.31, 0.34) CCT: 6581 K CRI: 85	306
CsPbBr <sub>3</sub> -TDDA	68%	80% (300 min, water)	Blue chip (453 nm)/CsPbBr <sub>3</sub> -TDDA, KSF (silicone resin)	63 lm W <sup>-1</sup> (20 mA) 57 lm W <sup>-1</sup>	121% NTSC (0.31, 0.29) CCT: 7072 K CRI: 83	307
CsPbX <sub>3</sub> -PLA	33-90%	80% (50h, working on LED)	Blue chip/CsPbBr <sub>3</sub> -PLA (PMMA)/(Ba, Ca, Sr <sub>3</sub> SiO <sub>5</sub> )Eu	62.93 lm W <sup>-1</sup> (Working for 15 h)	(0.38, 0.37)	311
CsPbX <sub>3</sub> /PMMA	45%	75% (3 d, 30 °C air with 70% humidity)	Blue chip (460 nm)/CsPbX <sub>3</sub> /PMMA, CdSe QDs (silicone resin)	50 lm W <sup>-1</sup> (Working for 50 h)	(0.34, 0.33)	337
CsPbBr <sub>3</sub> /EC	37.2%	95% (150 h, air)	Blue chip/CsPbBr <sub>3</sub> /EC, Sr <sub>2</sub> Si <sub>5</sub> N <sub>8</sub> :Eu <sup>2+</sup> (silicone)	65.78 lm W <sup>-1</sup> (20 mA)	CRI: 89.2 CCT: 7540 K CRI: 67.93	338
CsPbX <sub>3</sub> @SBS	1.1% (blue) 2.3% (green) 12.2% (red)	100% (10 min, water)	Blue chip (450 nm)/CsPb(Br/I) <sub>3</sub> @SBS/CsPbBr <sub>3</sub> @SBS	9 lm W <sup>-1</sup> (10 mA)	105% NTSC	341
MAPbBr <sub>3</sub> @APS	48%	95% (60 d, water) 65% (5 h, 100 °C)	Blue chip (450 nm)/red QDs@APS/MAPbBr <sub>3</sub> @APS (remote-type)	95% rec. 2020	75	
CsPbX <sub>3</sub> /PS	48% (green)	70% (192 h, water) 50% (2 h, 80 °C)	Blue chip (410 nm)/CdSe QDs (ethoxyline resin)/CsPbBr <sub>3</sub> /PS fiber	(0.34, 0.33) CCT: 5376 K	343	
CsPbBr <sub>3</sub> /EVA	40.5%	100% (192 h, air) ~100% (720 h, water)	Blue chip (460 nm)/CsPbBr <sub>3</sub> /EVA/ (Sr,Ca)AlSiN <sub>3</sub> :Eu <sup>2+</sup>	37.7 lm W <sup>-1</sup> (20 mA)	CRI: 74.7 CCT: 2347 K	344
MAPbX <sub>3</sub> /PVDF	38.4% (blue) 95% (green) 11% (red)	92% (400 h, UV)	Blue chip/KSF (adhesive)/MAPbBr <sub>3</sub> /PVDF	109 lm W <sup>-1</sup>	121% NTSC	76
CsPbX <sub>3</sub> -CB		80% (30 min, UV)	Blue chip/CsPbBr <sub>3</sub> -CB, CsPb(Br <sub>0.4</sub> I <sub>0.6</sub> ) <sub>3</sub> -CB	(20 mA)	(0.272, 0.278) (0.41, 0.37)	349
CsPb(Br/I) <sub>3</sub> @anthracene	41.9%	50% (100 °C)	UV chip (385 nm)/CsPb(Br <sub>0.6</sub> I <sub>0.4</sub> ) <sub>3</sub> @anthracene (PMMA)		(0.35, 0.30)	351
CsPbX <sub>3</sub> -PS	44% (green) 68% (green)	82% (24 h, water) 60% (16 d, UV)	Blue chip/CsPbBr <sub>1.2</sub> I <sub>1.8</sub> -PS/CsPbBr <sub>3</sub> -PS		(0.31, 0.30)	353
CsPbX <sub>3</sub> @PS		30% (30 d, water)	Blue chip (450 nm)/CsPbBr <sub>3</sub> @SiO <sub>2</sub> , CsPb(Br <sub>0.4</sub> I <sub>0.6</sub> ) <sub>3</sub> (silicone resin)		(0.31, 0.30)	356
CsPbBr <sub>3</sub> -SiO <sub>2</sub>		~100% (cooling from 100 °C to RT) 80% (96 h, UV)	Blue chip (450 nm)/CsPbBr <sub>3</sub> -SiO <sub>2</sub> , CsPb(Br <sub>0.4</sub> I <sub>0.6</sub> ) <sub>3</sub> (silicone resin)		113% NTSC (0.24, 0.28)	109

Table 2 (continued)

Composites	PL QY <sub>S</sub>	Stability	Device structure	Luminous efficacy and device lifetime	Other index	Ref.
CsPbBr <sub>3</sub> /SiO <sub>2</sub>	80%	98% (10 h, UV)	Blue chip/CdSe NCs (PMMA)/CsPbBr <sub>3</sub> /SiO <sub>2</sub> (PMMA)	56 lm W <sup>-1</sup> (5 mA) Unchanged after working for 1 h (1 mA)	138% NTSC (0.30, 0.32)	77
CsPbBr <sub>3</sub> –SiO <sub>2</sub>	71.8%	63.5% (80 °C)	Blue chip (450 nm)/CsPbBr <sub>3</sub> –SiO <sub>2</sub> , CsPbBr <sub>1.2</sub> I <sub>1.8</sub> (silicone resin)	35.4 lm W <sup>-1</sup> (20 mA)	126% NTSC (0.33, 0.36)	366
CsPbX <sub>3</sub> /SiO <sub>2</sub>	85% (green) 88% (red)	95% (90 d, air) Stable (5 d, UV)	Blue chip (458 nm)/CsPbBr <sub>3</sub> /SiO <sub>2</sub> , red QDs (PMMA) (remote-type)	61.2 lm W <sup>-1</sup> (20 mA)	120% NTSC (0.33, 0.33)	74
CsPbX <sub>3</sub> /SiO <sub>2</sub>	11.2% (blue) 82% (green)	93% (30 d, air)	Blue chip (441 nm)/CsPbBr <sub>3</sub> /SiO <sub>2</sub> , CsPb(Br <sub>0.3</sub> I <sub>0.7</sub> ) <sub>3</sub> /SiO <sub>2</sub> (PMMA)	Little variation after working for 10 h 35.32 lm W <sup>-1</sup>	(0.30, 0.31)	369
CsPbX <sub>3</sub> –zeolites	7.3% (red)	50% (80 °C)	Blue chip (460 nm)/CsPb(Br <sub>0.4</sub> I <sub>0.6</sub> ) <sub>3</sub> , CsPbBr <sub>3</sub> –zeolites (silicone resin)	2 lm W <sup>-1</sup> (20 mA)	127% NTSC (0.33, 0.36)	376
CsPbX <sub>3</sub> –CaF <sub>2</sub>	50% (blue) 82% (green)	56% (80 h, UV) 60% (2 d, air with 100% humidity)	Blue chip (460 nm)/KSF (silicone resin)/CsPbBr <sub>3</sub> –CaF <sub>2</sub> (PMMA)	62.7 lm W <sup>-1</sup> (20 mA)	CCT: 5623 K 122% NTSC (0.33, 0.30)	377
MAPbBr <sub>3</sub> /NaNO <sub>3</sub>	66% (red)		Blue chip (445 nm)/KSF, MAPbBr <sub>3</sub> /NaNO <sub>3</sub> (silicone resin)	56.3 lm W <sup>-1</sup> (Working for 8 h) 22.39 lm W <sup>-1</sup> (20 mA)	127% NTSC (0.28, 0.32)	381
MAPbBr <sub>3</sub> /NaNO <sub>3</sub>	42%	80% (14 h, UV) 36% (300 min, 100 °C)	Blue chip (450 nm)/KSF, MAPbBr <sub>3</sub> /NaNO <sub>3</sub> (silicone resin)	~11 lm W <sup>-1</sup> (Working for 4 h, 20 mA)	CRI: 86.6	381
CsPbBr <sub>3</sub> @NH <sub>4</sub> Br	64.21%	40% (3.5 h, water) 96% (cooling from 100 °C to RT)	Blue chip/CsPbBr <sub>3</sub> @NH <sub>4</sub> Br, KSF (silicone resin)	151 lm W <sup>-1</sup> (20 mA)	90.6% rec. 2020 (0.331, 0.331)	382
CsPbBr <sub>3</sub> /Cs <sub>4</sub> PbBr <sub>6</sub>	97%		Blue chip/KSF (silicone resin)/CsPbBr <sub>3</sub> /Cs <sub>4</sub> PbBr <sub>6</sub>	151 lm W <sup>-1</sup> (20 mA)	95% rec. 2020	400
CsPbBr <sub>3</sub> /Cs <sub>4</sub> PbBr <sub>6</sub>	95%	93% (80 min, blue light irradiation) 80% (14 d, air)	CsPbBr <sub>3</sub> /Cs <sub>4</sub> PbBr <sub>6</sub> , KSF	73.8 lm W <sup>-1</sup> (5 mA)	(0.331, 0.331)	403
CsPbBr <sub>3</sub> –SDDDA/SiO <sub>2</sub> /PMMA	6.3%		Blue chip (458 nm)/CsPbBr <sub>3</sub> –SDDDA/SiO <sub>2</sub> /PMMA, KSF (silicone resin)	102% NTSC (0.271, 0.232)	404	
CsPbBr <sub>3</sub> /SiO <sub>2</sub> –Al <sub>2</sub> O <sub>3</sub>	90%		Blue chip (455 nm)/CsPbBr <sub>3</sub> , CsPbBr <sub>3</sub> /SiO <sub>2</sub> –Al <sub>2</sub> O <sub>3</sub> (PDMS)	80.77	405	
CsPbX <sub>3</sub> –PMPOPNC	67% (blue) 85% (green) 69% (red)	70% (1 h, 100 °C) >80% (120 °C) >80% (156 h, UV) >60% (70 d, UV) ~100% (60 d, air) 52% (100 °C) 85% (5 d, UV)	Blue chip (460 nm)/red YAG (silicone resin)/CsPbX <sub>3</sub> –PMPOPNC (silicone resin)	26.3 (20 mA)	(0.35, 0.32) CCT: 4325 K CRI: 70.5	409
CsPbBr <sub>3</sub> /PSZ	81.7%		Blue chip (455 nm)/CsPbBr <sub>3</sub> /PSZ, KSF (PMMA)	138.6 (60 mA)	111% NTSC (0.34, 0.33)	410
CsPbBr <sub>3</sub> –phospho-silicate glass	63%		Blue chip (460 nm)/CsPbBr <sub>3</sub> glass/CaAlSiN <sub>3</sub> :Eu <sup>2+</sup> (epoxy resin)	50.5 (20 mA)	CCT: 6762 K CRI: 83.4 (0.33, 0.32)	415
CsPbBr <sub>12</sub>	65%		Blue chip (460 nm)/YAG:Ce PiG/CsPbBr <sub>12</sub> (PMMA) (remote-type)	58 (20 mA)	CCT: 5907 K CRI: 90	422

form a mechanical protection, which mitigates the damage by oxygen and moisture. The most difficult issue in this regard is the limited thermal stability of PQD-based phosphors. Although some methods are developed such as the PiG technique or a remote-type device architecture can relieve the thermal-induced degradation, the thermal stability should be further improved.

In summary, the poor stability of PQDs has aroused a wide concern, and simultaneously, many strategies have been developed to overcome this problem in the past few years. As a result, the stability of PQDs and the corresponding device lifetime of pc-LEDs have been improved; however, they are still far away from the commercial requirements. Further stabilizing perovskites and preventing their decomposition are needed. Among the various protection methods, the outstanding photoluminescence property can be retained through compositional or surface engineering routes, which show promise in the applications of photonic as well as optoelectronic devices. However, the electroconductivity is sacrificed after compact polymer or inorganics coating. Thus, the obtained composites are no longer suitable for optoelectronic devices. Although immense progress has been made in enhancing the stability against water and oxygen damage, their thermal stability is still limited. This situation is quiet like the core-only CdSe QDs. Therefore, a compact and monodispersed shell shielding that ensures thermal stability and simultaneously electroconductivity is more favorable. Our review on understanding of the origins of instability and the corresponding strategies for enhancing the stability is helpful to design stable perovskite light emitters. We hope that this review could encourage more researchers to devote additional efforts to address the stability of PQDs. And we are convinced that a highly luminescent and stable color-converter together with a high optical performance and long device lifetime pc-LED will come out in the near future.

## List of acronyms and abbreviations

ABS	Acrylonitrile butadiene styrene	EVA	Ethylene vinyl acetate
ACN	Acetonitrile	FA	Formamidinium, $\text{CH}(\text{NH}_2)_2^+$
ADBr	2-Adamantylammonium bromide	FWHM	Full width at half maximum
AIBN	2,2-Azobisisobutyronitrile	GC	Gas chromatography
ALD	Atomic layer deposition	GO-g-PAA	Polyacrylic acid-grafted graphene oxide
APTES	(3-Aminopropyl)triethoxysilane	HRTEM	High resolution transmission electron microscopy
BnOH	Benzyl alcohol	Irgacure 819	Bis(2,4,6-trimethylbenzoyl)-phenylphosphineoxide
CA	Cellulose acetate	LARP	Ligand-assisted reprecipitation
CB	Conduction band	LCDs	Liquid crystal displays
CBB	Carboxybenzene	LE	Luminous efficacy
CCT	Correlated color temperature	LEDs	Light-emitting diodes
CRI	Color rendering index	LHPS	Lead halide perovskites
DDAB	Di-dodecyl dimethyl ammonium bromide	MA	Methylammonium, $\text{CH}_3\text{NH}_3^+$
DFT	Density functional theory	MAA	Methacrylic acid
DMF	Dimethyl formamide	MMA	Methyl methacrylate
DOSY	Diffusion Ordered NMR Spectroscopy	MA-POSS	POSS-appended methacrylate
DPPA	Diphenylphosphinic acid	MOF	Metal-organic framework
EC	Ethyl cellulose	NCs	Nanocrystals
EL	Electroluminescence	NH <sub>2</sub> -POSS	Polyhedral silsesquioxane-[3-(2-aminoethyl)amino]-propylheptaisobutyl substituted
EQE	External quantum efficiency	NIR	Near-infrared
		NMR	Nuclear magnetic resonance
		NPs	Nanoparticles
		NSs	Nanosheets
		NTSC	National Television System Committee
		OA	Oleic acid
		OLA	Oleylamine
		OLEDs	Organic LEDs
		P2VP	Poly-2-vinylpyridine
		PC	Polycarbonate
		PCE	Power conversion efficiency
		pc-LEDs	Phosphor-converted light-emitting diodes
		PDs	Photodetectors
		PDMS	Polydimethylsiloxane
		PeLEDs	Perovskite LEDs
		PEA	Phenylethylamine, $\text{C}_8\text{H}_9\text{NH}_3$
		PEDOT	Poly(3,4-ethylenedioxythiophene)
		PiG	Phosphor-in-glass
		PL	Photoluminescence
		PLA	Poly(lactic acid)
		PLMA	Poly(lauryl methacrylate)
		PL QYs	Photoluminescence quantum yields
		PMA	Poly(maleic anhydride- <i>alt</i> -1-octadecene)
		PMMA	Polymethyl methacrylate
		POSS	Polyhedral oligomeric silsesquioxane
		PQDs	Perovskite quantum dots
		PS	Polystyrene
		PS- <i>b</i> -PEO	Polystyrene- <i>b</i> -poly(ethyl oxide)
		PSZ	Polysilazane
		PVs	Photovoltaics
		PVC	Polyvinyl chloride
		PVDF	Polyvinylidene fluoride
		PVP	Polyvinylpyrrolidone
		QLEDs	QD LEDs
		RE	Rare earth

RT	Room temperature
SBS	Poly(styrene-butadiene-styrene)
SDDA	Didodecyl dimethylammonium sulfide
SEBS	Poly(styrene-ethylene-butylenestyrene)
SEC	Spectro-electrochemical
SH- $\beta$ -CD	Mercapto- $\beta$ -cyclodextrin
TA	Transient absorption
TDPA	1-Tetradecylphosphonic acid
TerEDOT	2,2',5',2"-Ter-3,4-ethylenedioxothiophene
TEOS	Tetraethyl orthosilicate
TGA	Thermogravimetric analysis
TMA	Trimethylaluminum
TMOS	Tetramethyl orthosilicate
TMPPA	Bis-(2,2,4-trimethylpentyl)phosphinic acid
ToF-SIMS	Time-of-flight secondary ion-mass spectrometry
TOP	Trioctylphosphine
TOPO	Trioctylphosphine oxide
V18	4-Vinylbenzyl-dimethyloctadecylammonium chloride
VB	Valance band
wLEDs	White LEDs
XANES	X-ray absorption near-edge spectroscopy
XPS	X-ray photoelectron spectroscopy
XRD	X-ray diffraction
YAG	$Y_3Al_5O_{12}$

## Conflicts of interest

There are no conflicts to declare.

## Acknowledgements

This project was financially supported by the National Natural Science Foundation of China (NSFC 51772288, 51472231, 51720105015, and 51750110511), Science and Technology Development Planning Project of Jilin Province (20170101187JC and 20170414003GH), Jiangmen Innovative Research Team Program (2017), Major program of basic research and applied research of Guangdong Province (2017KZDXM083), the Key Research Program of Frontier Sciences, CAS (Grant No. YZDY-SSW-JSC018), and the CAS-Croucher Funding Scheme for Joint Laboratories (CAS18204).

## References

- 1 A. Kojima, K. Teshima, Y. Shirai and T. Miyasaka, *J. Am. Chem. Soc.*, 2009, **131**, 6050–6051.
- 2 M. Liu, M. B. Johnston and H. J. Snaith, *Nature*, 2013, **501**, 395.
- 3 D. W. de Quilettes, S. M. Vorpahl, S. D. Stranks, H. Nagaoka, G. E. Eperon, M. E. Ziffer, H. J. Snaith and D. S. Ginger, *Science*, 2015, **348**, 683–686.
- 4 N. J. Jeon, J. H. Noh, W. S. Yang, Y. C. Kim, S. Ryu, J. Seo and S. I. Seok, *Nature*, 2015, **517**, 476–480.
- 5 H. Tsai, W. Nie, J.-C. Blancon, C. C. Stoumpos, R. Asadpour, B. Harutyunyan, A. J. Neukirch, R. Verduzeo, J. J. Crochet, S. Tretiak, L. Pedesseau, J. Even, M. A. Alam, G. Gupta, J. Lou, P. M. Ajayan, M. J. Bedzyk, M. G. Kanatzidis and A. D. Mohite, *Nature*, 2016, **536**, 312–316.
- 6 F. Ye, H. Chen, F. Xie, W. Tang, M. Yin, J. He, E. Bi, Y. Wang, X. Yang and L. Han, *Energy Environ. Sci.*, 2016, **9**, 2295–2301.
- 7 N. Li, Z. Zhu, C.-C. Chueh, H. Liu, B. Peng, A. Petrone, X. Li, L. Wang and A. K. Y. Jen, *Adv. Energy Mater.*, 2017, **7**, 1601307.
- 8 W. S. Yang, B.-W. Park, E. H. Jung, N. J. Jeon, Y. C. Kim, D. U. Lee, S. S. Shin, J. Seo, E. K. Kim, J. H. Noh and S. I. Seok, *Science*, 2017, **356**, 1376–1379.
- 9 T. M. Brenner, D. A. Egger, L. Kronik, G. Hodes and D. Cahen, *Nat. Rev. Mater.*, 2016, **1**, 15007.
- 10 N. J. Jeon, H. Na, E. H. Jung, T.-Y. Yang, Y. G. Lee, G. Kim, H.-W. Shin, S. Il Seok, J. Lee and J. Seo, *Nat. Energy*, 2018, **3**, 682–689.
- 11 Z.-K. Tan, R. S. Moghaddam, M. L. Lai, P. Docampo, R. Higler, F. Deschler, M. Price, A. Sadhanala, L. M. Pazos, D. Credgington, F. Hanusch, T. Bein, H. J. Snaith and R. H. Friend, *Nat. Nanotechnol.*, 2014, **9**, 687–692.
- 12 H. Cho, S.-H. Jeong, M.-H. Park, Y.-H. Kim, C. Wolf, C.-L. Lee, J. H. Heo, A. Sadhanala, N. Myoung and S. Yoo, *Science*, 2015, **350**, 1222–1225.
- 13 M. Yuan, L. N. Quan, R. Comin, G. Walters, R. Sabatini, O. Voznyy, S. Hoogland, Y. Zhao, E. M. Beauregard and P. Kanjanaboons, *Nat. Nanotechnol.*, 2016, **11**, 872.
- 14 N. Wang, L. Cheng, R. Ge, S. Zhang, Y. Miao, W. Zou, C. Yi, Y. Sun, Y. Cao, R. Yang, Y. Wei, Q. Guo, Y. Ke, M. Yu, Y. Jin, Y. Liu, Q. Ding, D. Di, L. Yang, G. Xing, H. Tian, C. Jin, F. Cao, R. H. Friend, J. Wang and W. Huang, *Nat. Photonics*, 2016, **10**, 699–704.
- 15 Y. Ling, Y. Tian, X. Wang, J. C. Wang, J. M. Knox, F. Perez-Orive, Y. Du, L. Tan, K. Hanson, B. Ma and H. Gao, *Adv. Mater.*, 2016, **28**, 8983–8989.
- 16 L. Zhang, X. Yang, Q. Jiang, P. Wang, Z. Yin, X. Zhang, H. Tan, Y. M. Yang, M. Wei, B. R. Sutherland, E. H. Sargent and J. You, *Nat. Commun.*, 2017, **8**, 15640.
- 17 W. Zou, R. Li, S. Zhang, Y. Liu, N. Wang, Y. Cao, Y. Miao, M. Xu, Q. Guo, D. Di, L. Zhang, C. Yi, F. Gao, R. H. Friend, J. Wang and W. Huang, *Nat. Commun.*, 2018, **9**, 608.
- 18 J. Xing, Y. Zhao, M. Askerka, L. N. Quan, X. Gong, W. Zhao, J. Zhao, H. Tan, G. Long, L. Gao, Z. Yang, O. Voznyy, J. Tang, Z.-H. Lu, Q. Xiong and E. H. Sargent, *Nat. Commun.*, 2018, **9**, 3541.
- 19 L. N. Quan, F. P. García de Arquer, R. P. Sabatini and E. H. Sargent, *Adv. Mater.*, 2018, **30**, 1801996.
- 20 M. Bidikoudi, E. Fresta and R. D. Costa, *Chem. Commun.*, 2018, **54**, 8150–8169.
- 21 H. Zhu, Y. Fu, F. Meng, X. Wu, Z. Gong, Q. Ding, M. V. Gustafsson, M. T. Trinh, S. Jin and X. Zhu, *Nat. Mater.*, 2015, **14**, 636–642.
- 22 S. A. Veldhuis, P. P. Boix, N. Yantara, M. Li, T. C. Sum, N. Mathews and S. G. Mahisalkar, *Adv. Mater.*, 2016, **28**, 6804–6834.

- 23 X. Tang, Z. Hu, W. Yuan, W. Hu, H. Shao, D. Han, J. Zheng, J. Hao, Z. Zang, J. Du, Y. Leng, L. Fang and M. Zhou, *Adv. Opt. Mater.*, 2017, **5**, 1600788.
- 24 Y. Wang, X. Li, V. Nalla, H. Zeng and H. Sun, *Adv. Funct. Mater.*, 2017, **27**, 1605088.
- 25 W. Zheng, P. Huang, Z. Gong, D. Tu, J. Xu, Q. Zou, R. Li, W. You, J.-C. G. Bünzli and X. Chen, *Nat. Commun.*, 2018, **9**, 3462.
- 26 L. Jiang, R. Liu, R. Su, Y. Yu, H. Xu, Y. Wei, Z.-K. Zhou and X. Wang, *Nanoscale*, 2018, **10**, 13565–13571.
- 27 Y. C. Kim, K. H. Kim, D.-Y. Son, D.-N. Jeong, J.-Y. Seo, Y. S. Choi, I. T. Han, S. Y. Lee and N.-G. Park, *Nature*, 2017, **550**, 87.
- 28 W. Wei, Y. Zhang, Q. Xu, H. Wei, Y. Fang, Q. Wang, Y. Deng, T. Li, A. Gruverman, L. Cao and J. Huang, *Nat. Photonics*, 2017, **11**, 315.
- 29 S. Shrestha, R. Fischer, G. J. Matt, P. Feldner, T. Michel, A. Osvet, I. Levchuk, B. Merle, S. Golkar, H. Chen, S. F. Tedde, O. Schmidt, R. Hock, M. Rührig, M. Göken, W. Heiss, G. Anton and C. J. Brabec, *Nat. Photonics*, 2017, **11**, 436.
- 30 Q. Chen, J. Wu, X. Ou, B. Huang, J. Almutlaq, A. A. Zhumekenov, X. Guan, S. Han, L. Liang, Z. Yi, J. Li, X. Xie, Y. Wang, Y. Li, D. Fan, D. B. L. Teh, A. H. All, O. F. Mohammed, O. M. Bakr, T. Wu, M. Bettinelli, H. Yang, W. Huang and X. Liu, *Nature*, 2018, **561**, 88–93.
- 31 P. Büchele, M. Richter, S. F. Tedde, G. J. Matt, G. N. Ankah, R. Fischer, M. Biele, W. Metzger, S. Lilliu, O. Bikondoa, J. E. Macdonald, C. J. Brabec, T. Kraus, U. Lemmer and O. Schmidt, *Nat. Photonics*, 2015, **9**, 843–848.
- 32 J. H. Heo, D. H. Shin, J. K. Park, D. H. Kim, S. J. Lee and S. H. Im, *Adv. Mater.*, 2018, **30**, 1801743.
- 33 L. Dou, Y. M. Yang, J. You, Z. Hong, W.-H. Chang, G. Li and Y. Yang, *Nat. Commun.*, 2014, **5**, 5404.
- 34 M. I. Saidaminov, V. Adinolfi, R. Comin, A. L. Abdelhady, W. Peng, I. Dursun, M. Yuan, S. Hoogland, E. H. Sargent and O. M. Bakr, *Nat. Commun.*, 2015, **6**, 8724.
- 35 Y. Guo, C. Liu, H. Tanaka and E. Nakamura, *J. Phys. Chem. Lett.*, 2015, **6**, 535–539.
- 36 W. Deng, L. Huang, X. Xu, X. Zhang, X. Jin, S.-T. Lee and J. Jie, *Nano Lett.*, 2017, **17**, 2482–2489.
- 37 H. Wang and D. H. Kim, *Chem. Soc. Rev.*, 2017, **46**, 5204–5236.
- 38 Y. Dong, Y. Zou, J. Song, X. Song and H. Zeng, *J. Mater. Chem. C*, 2017, **5**, 11369–11394.
- 39 L. Polavarapu, B. Nickel, J. Feldmann and A. S. Urban, *Adv. Energy Mater.*, 2017, **7**, 1700267.
- 40 S.-T. Ha, R. Su, J. Xing, Q. Zhang and Q. Xiong, *Chem. Sci.*, 2017, **8**, 2522–2536.
- 41 Z. Shi, Y. Li, Y. Zhang, Y. Chen, X. Li, D. Wu, T. Xu, C. Shan and G. Du, *Nano Lett.*, 2017, **17**, 313–321.
- 42 J. Song, J. Li, X. Li, L. Xu, Y. Dong and H. Zeng, *Adv. Mater.*, 2015, **27**, 7162–7167.
- 43 A. B. Wong, M. Lai, S. W. Eaton, Y. Yu, E. Lin, L. Dou, A. Fu and P. Yang, *Nano Lett.*, 2015, **15**, 5519–5524.
- 44 Y. Liu, M. Guo, S. Dong, X. Jiao, T. Wang and D. Chen, *J. Mater. Chem. C*, 2018, **6**, 7797–7802.
- 45 Y. Tong, B. J. Bohn, E. Bladt, K. Wang, P. Müller-Buschbaum, S. Bals, A. S. Urban, L. Polavarapu and J. Feldmann, *Angew. Chem., Int. Ed.*, 2017, **56**, 13887–13892.
- 46 Y. Ling, Z. Yuan, Y. Tian, X. Wang, J. C. Wang, Y. Xin, K. Hanson, B. Ma and H. Gao, *Adv. Mater.*, 2016, **28**, 305–311.
- 47 Q. Liao, K. Hu, H. Zhang, X. Wang, J. Yao and H. Fu, *Adv. Mater.*, 2015, **27**, 3405–3410.
- 48 Y. Tong, E.-P. Yao, A. Manzi, E. Bladt, K. Wang, M. Döblinger, S. Bals, P. Müller-Buschbaum, A. S. Urban, L. Polavarapu and J. Feldmann, *Adv. Mater.*, 2018, **30**, 1801117.
- 49 K. Lin, J. Xing, L. N. Quan, F. P. G. de Arquer, X. Gong, J. Lu, L. Xie, W. Zhao, D. Zhang, C. Yan, W. Li, X. Liu, Y. Lu, J. Kirman, E. H. Sargent, Q. Xiong and Z. Wei, *Nature*, 2018, **562**, 245–248.
- 50 Y. Cao, N. Wang, H. Tian, J. Guo, Y. Wei, H. Chen, Y. Miao, W. Zou, K. Pan, Y. He, H. Cao, Y. Ke, M. Xu, Y. Wang, M. Yang, K. Du, Z. Fu, D. Kong, D. Dai, Y. Jin, G. Li, H. Li, Q. Peng, J. Wang and W. Huang, *Nature*, 2018, **562**, 249–253.
- 51 Q. Shan, J. Song, Y. Zou, J. Li, L. Xu, J. Xue, Y. Dong, B. Han, J. Chen and H. Zeng, *Small*, 2017, **13**, 1701770.
- 52 C. Wu, Y. Zou, T. Wu, M. Ban, V. Pecunia, Y. Han, Q. Liu, T. Song, S. Duhm and B. Sun, *Adv. Funct. Mater.*, 2017, **27**, 1700338.
- 53 H.-C. Wang, Z. Bao, H.-Y. Tsai, A.-C. Tang and R.-S. Liu, *Small*, 2018, **14**, 1702433.
- 54 A. Swarnkar, R. Chulliyil, V. K. Ravi, M. Irfanullah, A. Chowdhury and A. Nag, *Angew. Chem.*, 2015, **127**, 15644–15648.
- 55 X. Li, Y. Wu, S. Zhang, B. Cai, Y. Gu, J. Song and H. Zeng, *Adv. Funct. Mater.*, 2016, **26**, 2435–2445.
- 56 F. Zhang, H. Zhong, C. Chen, X.-g. Wu, X. Hu, H. Huang, J. Han, B. Zou and Y. Dong, *ACS Nano*, 2015, **9**, 4533–4542.
- 57 J. Li, L. Xu, T. Wang, J. Song, J. Chen, J. Xue, Y. Dong, B. Cai, Q. Shan, B. Han and H. Zeng, *Adv. Mater.*, 2017, **29**, 1603885.
- 58 D. Han, M. Imran, M. Zhang, S. Chang, X.-g. Wu, X. Zhang, J. Tang, M. Wang, S. Ali, X. Li, G. Yu, J. Han, L. Wang, B. Zou and H. Zhong, *ACS Nano*, 2018, **12**, 8808–8816.
- 59 J. Song, J. Li, L. Xu, J. Li, F. Zhang, B. Han, Q. Shan and H. Zeng, *Adv. Mater.*, 2018, **30**, 1800764.
- 60 K. Hoshi, T. Chiba, J. Sato, Y. Hayashi, Y. Takahashi, H. Ebe, S. Ohisa and J. Kido, *ACS Appl. Mater. Interfaces*, 2018, **10**, 24607–24612.
- 61 T. Chiba, K. Hoshi, Y.-J. Pu, Y. Takeda, Y. Hayashi, S. Ohisa, S. Kawata and J. Kido, *ACS Appl. Mater. Interfaces*, 2017, **9**, 18054–18060.
- 62 B. Geffroy, P. Le Roy and C. Prat, *Polym. Int.*, 2006, **55**, 572–582.
- 63 W. K. Bae, J. Kwak, J. W. Park, K. Char, C. Lee and S. Lee, *Adv. Mater.*, 2009, **21**, 1690–1694.
- 64 X. Dai, Z. Zhang, Y. Jin, Y. Niu, H. Cao, X. Liang, L. Chen, J. Wang and X. Peng, *Nature*, 2014, **515**, 96–99.
- 65 P. Pust, V. Weiler, C. Hecht, A. Tücks, A. S. Wochnik, A.-K. Henß, D. Wiechert, C. Scheu, P. J. Schmidt and W. Schnick, *Nat. Mater.*, 2014, **13**, 891–896.
- 66 G. Li, Y. Tian, Y. Zhao and J. Lin, *Chem. Soc. Rev.*, 2015, **44**, 8688–8713.
- 67 L. Wang, R.-J. Xie, T. Suehiro, T. Takeda and N. Hirosaki, *Chem. Rev.*, 2018, **118**, 1951–2009.

- 68 Z. Xia and A. Meijerink, *Chem. Soc. Rev.*, 2017, **46**, 275–299.
- 69 N. C. George, K. A. Denault and R. Seshadri, *Annu. Rev. Mater. Res.*, 2013, **43**, 481–501.
- 70 C. C. Lin and R.-S. Liu, *J. Phys. Chem. Lett.*, 2011, **2**, 1268–1277.
- 71 L. Protesescu, S. Yakunin, M. I. Bodnarchuk, F. Krieg, R. Caputo, C. H. Hendon, R. X. Yang, A. Walsh and M. V. Kovalenko, *Nano Lett.*, 2015, **15**, 3692–3696.
- 72 M. V. Kovalenko, L. Protesescu and M. I. Bodnarchuk, *Science*, 2017, **358**, 745–750.
- 73 Q. A. Akkerman, G. Rainò, M. V. Kovalenko and L. Manna, *Nat. Mater.*, 2018, **17**, 394–405.
- 74 C. Sun, Y. Zhang, C. Ruan, C. Yin, X. Wang, Y. Wang and W. W. Yu, *Adv. Mater.*, 2016, **28**, 10088–10094.
- 75 Y. Wang, J. He, H. Chen, J. Chen, R. Zhu, P. Ma, A. Towers, Y. Lin, A. J. Gesquiere, S. T. Wu and Y. Dong, *Adv. Mater.*, 2016, **28**, 10710–10717.
- 76 Q. Zhou, Z. Bai, W. g. Lu, Y. Wang, B. Zou and H. Zhong, *Adv. Mater.*, 2016, **28**, 9163–9168.
- 77 H. Hu, L. Wu, Y. Tan, Q. Zhong, M. Chen, Y. Qiu, D. Yang, B. Sun, Q. Zhang and Y. Yin, *J. Am. Chem. Soc.*, 2017, **140**, 406–412.
- 78 M. Imran, V. Caligiuri, M. Wang, L. Goldoni, M. Prato, R. Krahne, L. De Trizio and L. Manna, *J. Am. Chem. Soc.*, 2018, **140**, 2656–2664.
- 79 Y. Tong, E. Bladt, M. F. Aygüler, A. Manzi, K. Z. Milowska, V. A. Hintermayr, P. Docampo, S. Bals, A. S. Urban, L. Polavarapu and J. Feldmann, *Angew. Chem., Int. Ed.*, 2016, **55**, 13887–13892.
- 80 H. Liu, Z. Wu, H. Gao, J. Shao, H. Zou, D. Yao, Y. Liu, H. Zhang and B. Yang, *ACS Appl. Mater. Interfaces*, 2017, **9**, 42919–42927.
- 81 S. W. Dai, B. W. Hsu, C. Y. Chen, C. A. Lee, H. Y. Liu, H. F. Wang, Y. C. Huang, T. L. Wu, A. Manikandan, R. M. Ho, C.-S. Tsao, C.-H. Cheng, Y.-L. Chueh and H.-W. Lin, *Adv. Mater.*, 2018, **30**, 1705532.
- 82 D. N. Minh, J. Kim, J. Hyon, J. H. Sim, H. H. Sowlih, C. Seo, J. Nam, S. Eom, S. Suk, S. Lee, E. Kim and Y. Kang, *Chem. Mater.*, 2017, **29**, 5713–5719.
- 83 H. Huang, Q. Xue, B. Chen, Y. Xiong, J. Schneider, C. Zhi, H. Zhong and A. L. Rogach, *Angew. Chem., Int. Ed.*, 2017, **56**, 9571–9576.
- 84 S. Chang, Z. Bai and H. Zhong, *Adv. Opt. Mater.*, 2018, **6**, 1800380.
- 85 T. Guner and M. M. Demir, *Phys. Status Solidi A*, 2018, **215**, 1800120.
- 86 H. C. Yoon, H. Kang, S. Lee, J. H. Oh, H. Yang and Y. R. Do, *ACS Appl. Mater. Interfaces*, 2016, **8**, 18189–18200.
- 87 H. C. Yoon, J. H. Oh, S. Lee, J. B. Park and Y. R. Do, *Sci. Rep.*, 2017, **7**, 2808.
- 88 X. Dai, Y. Deng, X. Peng and Y. Jin, *Adv. Mater.*, 2017, **29**, 1607022.
- 89 Y. E. Panfil, M. Oded and U. Banin, *Angew. Chem., Int. Ed.*, 2018, **57**, 4274–4295.
- 90 N. H. Tiep, Z. Ku and H. J. Fan, *Adv. Energy Mater.*, 2016, **6**, 1501420.
- 91 J. You, L. Meng, T.-B. Song, T.-F. Guo, Y. M. Yang, W.-H. Chang, Z. Hong, H. Chen, H. Zhou, Q. Chen, Y. Liu, N. D. Marco and Y. Yang, *Nat. Nanotechnol.*, 2016, **11**, 75–81.
- 92 H. Cho, Y. H. Kim, C. Wolf, H. D. Lee and T. W. Lee, *Adv. Mater.*, 2018, **30**, 1704587.
- 93 T. A. Berhe, W.-N. Su, C.-H. Chen, C.-J. Pan, J.-H. Cheng, H.-M. Chen, M.-C. Tsai, L.-Y. Chen, A. A. Dubale and B.-J. Hwang, *Energy Environ. Sci.*, 2016, **9**, 323–356.
- 94 T. Leijtens, G. E. Eperon, N. K. Noel, S. N. Habisreutinger, A. Petrozza and H. J. Snaith, *Adv. Energy Mater.*, 2015, **5**, 1500963.
- 95 L. Gomez, C. de Weerd, J. L. Hueso and T. Gregorkiewicz, *Nanoscale*, 2017, **9**, 631–636.
- 96 F. Lang, O. Shargaiava, V. V. Brus, H. C. Neitzert, J. Rappich and N. H. Nickel, *Adv. Mater.*, 2018, **30**, 1702905.
- 97 J. De Roo, M. Ibáñez, P. Geiregat, G. Nedelcu, W. Walravens, J. Maes, J. C. Martins, I. Van Driessche, M. V. Kovalenko and Z. Hens, *ACS Nano*, 2016, **10**, 2071–2081.
- 98 X. Li, F. Cao, D. Yu, J. Chen, Z. Sun, Y. Shen, Y. Zhu, L. Wang, Y. Wei, Y. Wu and H. Zeng, *Small*, 2017, **13**, 1603996.
- 99 Y. Kim, E. Yassitepe, O. Voznyy, R. Comin, G. Walters, X. Gong, P. Kanjanaboons, A. F. Nogueira and E. H. Sargent, *ACS Appl. Mater. Interfaces*, 2015, **7**, 25007–25013.
- 100 S. Yang, Y. Wang, P. Liu, Y.-B. Cheng, H. J. Zhao and H. G. Yang, *Nat. Energy*, 2016, **1**, 15016.
- 101 R. Roesch, T. Faber, E. von Hauff, T. M. Brown, M. Lira-Cantu and H. Hoppe, *Adv. Energy Mater.*, 2015, **5**, 1501924.
- 102 S. Zou, Y. Liu, J. Li, C. Liu, R. Feng, F. Jiang, Y. Li, J. Song, H. Zeng, M. Hong and X. Chen, *J. Am. Chem. Soc.*, 2017, **139**, 11443–11450.
- 103 G. P. Nagabhushana, R. Shivaramaiah and A. Navrotsky, *Proc. Natl. Acad. Sci. U. S. A.*, 2016, **113**, 7717–7721.
- 104 E. J. Juarez-Perez, Z. Hawash, S. R. Raga, L. K. Ono and Y. Qi, *Energy Environ. Sci.*, 2016, **9**, 3406–3410.
- 105 M. Kulkarni, S. Gupta, N. Kedem, I. Levine, T. Bendikov, G. Hodes and D. Cahen, *J. Phys. Chem. Lett.*, 2015, **7**, 167–172.
- 106 G. Nedelcu, L. Protesescu, S. Yakunin, M. I. Bodnarchuk, M. J. Grotevent and M. V. Kovalenko, *Nano Lett.*, 2015, **15**, 5635–5640.
- 107 H. Huang, B. Chen, Z. Wang, T. F. Hung, A. S. Susha, H. Zhong and A. L. Rogach, *Chem. Sci.*, 2016, **7**, 5699–5703.
- 108 V. K. Ravi, R. A. Scheidt, A. Nag, M. Kuno and P. V. Kamat, *ACS Energy Lett.*, 2018, **3**, 1049–1055.
- 109 H. C. Wang, S. Y. Lin, A. C. Tang, B. P. Singh, H. C. Tong, C. Y. Chen, Y. C. Lee, T. L. Tsai and R. S. Liu, *Angew. Chem., Int. Ed.*, 2016, **55**, 7924–7929.
- 110 Q. A. Akkerman, V. D’Innocenzo, S. Accornero, A. Scarpellini, A. Petrozza, M. Prato and L. Manna, *J. Am. Chem. Soc.*, 2015, **137**, 10276–10281.
- 111 X. Chen, H. Hu, Z. Xia, W. Gao, W. Gou, Y. Qu and Y. Ma, *J. Mater. Chem. C*, 2017, **5**, 309–313.
- 112 C. Guhrenz, A. Benad, C. Ziegler, D. Haubold, N. Gaponik and A. Eychmüller, *Chem. Mater.*, 2016, **28**, 9033–9040.
- 113 H. Huang, M. I. Bodnarchuk, S. V. Kershaw, M. V. Kovalenko and A. L. Rogach, *ACS Energy Lett.*, 2017, **2**, 2071–2083.
- 114 D. Yang, X. Li and H. Zeng, *Adv. Mater. Interfaces*, 2018, **5**, 1701662.

- 115 S. Huang, Z. Li, B. Wang, N. Zhu, C. Zhang, L. Kong, Q. Zhang, A. Shan and L. Li, *ACS Appl. Mater. Interfaces*, 2017, **9**, 7249–7258.
- 116 K. Chen, S. Schünemann, S. Song and H. Tüysüz, *Chem. Soc. Rev.*, 2018, **47**, 7045–7077.
- 117 Z. Cheng and J. Lin, *CrystEngComm*, 2010, **12**, 2646–2662.
- 118 K. Huang, R. S. Tichy and J. B. Goodenough, *J. Am. Ceram. Soc.*, 1998, **81**, 2565–2575.
- 119 D. Lebeugle, D. Colson, A. Forget and M. Viret, *Appl. Phys. Lett.*, 2007, **91**, 022907.
- 120 J. Suntivich, K. J. May, H. A. Gasteiger, J. B. Goodenough and Y. Shao-Horn, *Science*, 2011, **334**, 1383–1385.
- 121 J. S. Manser, J. A. Christians and P. V. Kamat, *Chem. Rev.*, 2016, **116**, 12956–13008.
- 122 Y. Zhao and K. Zhu, *Chem. Soc. Rev.*, 2016, **45**, 655–689.
- 123 Z. Shi, J. Guo, Y. Chen, Q. Li, Y. Pan, H. Zhang, Y. Xia and W. Huang, *Adv. Mater.*, 2017, **29**, 1605005.
- 124 X. Guo and C. Burda, *Coord. Chem. Rev.*, 2016, **320**, 53–65.
- 125 C. C. Stoumpos and M. G. Kanatzidis, *Acc. Chem. Res.*, 2015, **48**, 2791–2802.
- 126 E. Salje, *Philos. Trans. R. Soc., A*, 1989, **328**, 409–416.
- 127 C. C. Stoumpos, C. D. Malliakas and M. G. Kanatzidis, *Inorg. Chem.*, 2013, **52**, 9019–9038.
- 128 K. Aleksandrov, *Ferroelectrics*, 1976, **14**, 801–805.
- 129 H. D. Megaw, *Crystal structures: a working approach*, Saunders Limited, 1973.
- 130 W. J. Yin, T. Shi and Y. Yan, *Adv. Mater.*, 2014, **26**, 4653–4658.
- 131 C. Quarti, E. Mosconi, J. M. Ball, V. D'Innocenzo, C. Tao, S. Pathak, H. J. Snaith, A. Petrozza and F. De Angelis, *Energy Environ. Sci.*, 2016, **9**, 155–163.
- 132 S. Colella, E. Mosconi, P. Fedeli, A. Listorti, F. Gazza, F. Orlandi, P. Ferro, T. Besagni, A. Rizzo, G. Calestani, G. Gigli, F. D. Angelis and R. Mosca, *Chem. Mater.*, 2013, **25**, 4613–4618.
- 133 D. P. Mcmeekin, G. Sadoughi, W. Rehman, G. E. Eperon, M. Saliba, M. T. Hörrantner, A. Haghhighirad, N. Sakai, L. Korte, B. Rech, M. B. Johnston, L. M. Herz and H. J. Snaith, *Science*, 2016, **351**, 151–155.
- 134 M. Saliba, T. Matsui, K. Domanski, J.-Y. Seo, A. Ummadisingu, S. M. Zakeeruddin, J.-P. Correa-Baena, W. R. Tress, A. Abate, A. Hagfeldt and M. Graetzel, *Science*, 2016, **354**, 206–209.
- 135 V. Goldschmidt, *Akad. Oslo I. Mat-Nat. Kl.*, 1926, **8**, 112–117.
- 136 G. Kieslich, S. Sun and A. K. Cheetham, *Chem. Sci.*, 2015, **6**, 3430–3433.
- 137 G. Kieslich, S. Sun and A. K. Cheetham, *Chem. Sci.*, 2014, **5**, 4712–4715.
- 138 M.-G. Ju, J. Dai, L. Ma and X. C. Zeng, *J. Am. Chem. Soc.*, 2017, **139**, 8038–8043.
- 139 W. Travis, E. Glover, H. Bronstein, D. Scanlon and R. Palgrave, *Chem. Sci.*, 2016, **7**, 4548–4556.
- 140 C. Li, X. Lu, W. Ding, L. Feng, Y. Gao and Z. Guo, *Acta Crystallogr., Sect. B: Struct. Sci.*, 2008, **64**, 702–707.
- 141 M. R. Filip, G. E. Eperon, H. J. Snaith and F. Giustino, *Nat. Commun.*, 2014, **5**, 5757.
- 142 A. Sadhanala, S. Ahmad, B. Zhao, N. Giesbrecht, P. M. Pearce, F. Deschler, R. L. Z. Hoye, K. C. Gödel, T. Bein, P. Docampo, S. E. Dutton, M. F. L. De Volder and R. H. Friend, *Nano Lett.*, 2015, **15**, 6095–6101.
- 143 J.-P. Correa-Baena, A. Abate, M. Saliba, W. Tress, T. J. Jacobsson, M. Grätzel and A. Hagfeldt, *Energy Environ. Sci.*, 2017, **10**, 710–727.
- 144 C. C. Stoumpos, C. D. Malliakas, J. A. Peters, Z. Liu, M. Sebastian, J. Im, T. C. Chasapis, A. C. Wibowo, D. Y. Chung and A. J. Freeman, *Cryst. Growth Des.*, 2013, **13**, 2722–2727.
- 145 F. Bertolotti, L. Protesescu, M. V. Kovalenko, S. Yakunin, A. Cervellino, S. J. Billinge, M. W. Terban, J. S. Pedersen, N. Masciocchi and A. Guagliardi, *ACS Nano*, 2017, **11**, 3819–3831.
- 146 A. Swarnkar, A. R. Marshall, E. M. Sanehira, B. D. Chernomordik, D. T. Moore, J. A. Christians, T. Chakrabarti and J. M. Luther, *Science*, 2016, **354**, 92–95.
- 147 A. Dutta, S. K. Dutta, S. Das Adhikari and N. Pradhan, *Angew. Chem., Int. Ed.*, 2018, **57**, 9083–9087.
- 148 L. Pedesseau, D. Saporì, B. Traore, R. Robles, H.-H. Fang, M. A. Loi, H. Tsai, W. Nie, J.-C. Blancon, A. Neukirch, S. Tretiak, A. D. Mohite, C. Katan, J. Even and M. Kepenekian, *ACS Nano*, 2016, **10**, 9776–9786.
- 149 Z. Yuan, Y. Shu, Y. Xin and B. Ma, *Chem. Commun.*, 2016, **52**, 3887–3890.
- 150 J. Jagielski, S. Kumar, W.-Y. Yu and C.-J. Shih, *J. Mater. Chem. C*, 2017, **5**, 5610–5627.
- 151 K. Tanaka, T. Takahashi, T. Ban, T. Kondo, K. Uchida and N. Miura, *Solid State Commun.*, 2003, **127**, 619–623.
- 152 S. Kumar, J. Jagielski, S. Yakunin, P. Rice, Y.-C. Chiu, M. Wang, G. Nedelcu, Y. Kim, S. Lin, E. J. Santos, M. V. Kovalenko and C.-J. Shih, *ACS Nano*, 2016, **10**, 9720–9729.
- 153 Z. Wu, C. Ji, Z. Sun, S. Wang, S. Zhao, W. Zhang, L. Li and J. Luo, *J. Mater. Chem. C*, 2018, **6**, 1171–1175.
- 154 M. C. Weidman, A. J. Goodman and W. A. Tisdale, *Chem. Mater.*, 2017, **29**, 5019–5030.
- 155 L. N. Quan, M. Yuan, R. Comin, O. Voznyy, E. M. Beauregard, S. Hoogland, A. Buin, A. R. Kirmani, K. Zhao, A. Amassian, D. H. Kim and E. H. Sargent, *J. Am. Chem. Soc.*, 2016, **138**, 2649–2655.
- 156 I. C. Smith, E. T. Hoke, D. Solis-Ibarra, M. D. McGehee and H. I. Karunadasa, *Angew. Chem., Int. Ed.*, 2014, **53**, 11232–11235.
- 157 D. H. Cao, C. C. Stoumpos, O. K. Farha, J. T. Hupp and M. G. Kanatzidis, *J. Am. Chem. Soc.*, 2015, **137**, 7843–7850.
- 158 C. R. Kagan, D. B. Mitzi and C. D. Dimitrakopoulos, *Science*, 1999, **286**, 945–947.
- 159 G. Grancini, C. Roldán-Carmona, I. Zimmermann, E. Mosconi, X. Lee, D. Martineau, S. Narbey, F. Oswald, F. De Angelis and M. Graetzel, *Nat. Commun.*, 2017, **8**, 15684.
- 160 C. Ma, C. Leng, Y. Ji, X. Wei, K. Sun, L. Tang, J. Yang, W. Luo, C. Li and Y. Deng, *Nanoscale*, 2016, **8**, 18309–18314.
- 161 G. Li, T. Zhang, N. Guo, F. Xu, X. Qian and Y. Zhao, *Angew. Chem., Int. Ed.*, 2016, **55**, 13460–13464.
- 162 Z. Wang, Q. Lin, F. P. Chmiel, N. Sakai, L. M. Herz and H. J. Snaith, *Nat. Energy*, 2017, **2**, 17135.
- 163 F. Li, Y. Pei, F. Xiao, T. Zeng, Z. Yang, J. Xu, J. Sun, B. Peng and M. Liu, *Nanoscale*, 2018, **10**, 6318–6322.

- 164 T. Zhang, L. Xie, L. Chen, N. Guo, G. Li, Z. Tian, B. Mao and Y. Zhao, *Adv. Funct. Mater.*, 2017, **27**, 1603568.
- 165 T. Ye, A. Bruno, G. Han, T. M. Koh, J. Li, N. F. Jamaludin, C. Soci, S. G. Mhaisalkar and W. L. Leong, *Adv. Funct. Mater.*, 2018, **28**, 1801654.
- 166 Y. Hu, T. Qiu, F. Bai, W. Ruan and S. Zhang, *Adv. Energy Mater.*, 2018, **8**, 1703620.
- 167 Y. Tian, C. Zhou, M. Worku, X. Wang, Y. Ling, H. Gao, Y. Zhou, Y. Miao, J. Guan and B. Ma, *Adv. Mater.*, 2018, **30**, 1707093.
- 168 Y. Chen, Y. Sun, J. Peng, J. Tang, K. Zheng and Z. Liang, *Adv. Mater.*, 2018, **30**, 1703487.
- 169 K. Zheng, Y. Chen, Y. Sun, J. Chen, P. Chábera, R. Schaller, M. J. Al-Marri, S. E. Canton, Z. Liang and T. Pullerits, *J. Mater. Chem. A*, 2018, **6**, 6244–6250.
- 170 H. Zhang, Q. Liao, Y. Wu, Z. Zhang, Q. Gao, P. Liu, M. Li, J. Yao and H. Fu, *Adv. Mater.*, 2018, **30**, 1706186.
- 171 J. Li, Q. Yu, Y. He, C. C. Stoumpos, G. Niu, G. G. Trimarchi, H. Guo, G. Dong, D. Wang, L. Wang and M. G. Kanatzidis, *J. Am. Chem. Soc.*, 2018, **140**, 11085–11090.
- 172 E. Shi, Y. Gao, B. P. Finkenauer, Akriti, A. H. Coffey and L. Dou, *Chem. Soc. Rev.*, 2018, **47**, 6046–6072.
- 173 H. Lin, C. Zhou, Y. Tian, T. Siegrist and B. Ma, *ACS Energy Lett.*, 2018, **3**, 54–62.
- 174 L. Dou, A. B. Wong, Y. Yu, M. Lai, N. Kornienko, S. W. Eaton, A. Fu, C. G. Bischak, J. Ma, T. Ding, N. S. Ginsberg, L.-W. Wang, A. P. Alivisatos and P. Yang, *Science*, 2015, **349**, 1518–1521.
- 175 J. Ren, X. Dong, G. Zhang, T. Li and Y. Wang, *New J. Chem.*, 2017, **41**, 13961–13967.
- 176 F. S. Zu, P. Amsalem, I. Salzmann, R. B. Wang, M. Ralaiarisoa, S. Kowarik, S. Duham and N. Koch, *Adv. Opt. Mater.*, 2017, **5**, 1700139.
- 177 H. Tsai, R. Asadpour, J.-C. Blancon, C. C. Stoumpos, O. Durand, J. W. Strzalka, B. Chen, R. Verduzco, P. M. Ajayan, S. Tretiak, J. Even, M. A. Alam, M. G. Kanatzidis, W. Nie and A. D. Mohite, *Science*, 2018, **360**, 67–70.
- 178 A. Ummadisingu, L. Steier, J.-Y. Seo, T. Matsui, A. Abate, W. Tress and M. Grätzel, *Nature*, 2017, **545**, 208–212.
- 179 G. F. Samu, C. Janáký and P. V. Kamat, *ACS Energy Lett.*, 2017, **2**, 1860–1861.
- 180 T. Zhang, S. H. Cheung, X. Meng, L. Zhu, Y. Bai, C. H. Y. Ho, S. Xiao, Q. Xue, S. K. So and S. Yang, *J. Phys. Chem. Lett.*, 2017, **8**, 5069–5076.
- 181 W. Nie, J.-C. Blancon, A. J. Neukirch, K. Appavoo, H. Tsai, M. Chhowalla, M. A. Alam, M. Y. Sfeir, C. Katan and J. Even, *Nat. Commun.*, 2016, **7**, 11574.
- 182 C. Zhao, B. Chen, X. Qiao, L. Luan, K. Lu and B. Hu, *Adv. Energy Mater.*, 2015, **5**, 1500279.
- 183 J. F. Galisteo-López, M. Anaya, M. Calvo and H. Míguez, *J. Phys. Chem. Lett.*, 2015, **6**, 2200–2205.
- 184 H. J. Snaith, A. Abate, J. M. Ball, G. E. Eperon, T. Leijtens, N. K. Noel, S. D. Stranks, J. T.-W. Wang, K. Wojciechowski and W. Zhang, *J. Phys. Chem. Lett.*, 2014, **5**, 1511–1515.
- 185 Y. Tian, M. Peter, E. Unger, M. Abdellah, K. Zheng, T. Pullerits, A. Yartsev, V. Sundström and I. G. Scheblykin, *Phys. Chem. Chem. Phys.*, 2015, **17**, 24978–24987.
- 186 W. Zhang, V. M. Burlakov, D. J. Graham, T. Leijtens, A. Osherov, V. Bulović, H. J. Snaith, D. S. Ginger and S. D. Stranks, *Nat. Commun.*, 2016, **7**, 11683.
- 187 E. T. Hoke, D. J. Slotcavage, E. R. Dohner, A. R. Bowring, H. I. Karunadasa and M. D. McGehee, *Chem. Sci.*, 2015, **6**, 613–617.
- 188 S. Huang, Z. Li, L. Kong, N. Zhu, A. Shan and L. Li, *J. Am. Chem. Soc.*, 2016, **138**, 5749–5752.
- 189 J. Chen, D. Liu, M. J. Al-Marri, L. Nuutila, H. Lehtivuori and K. Zheng, *Sci. China Mater.*, 2016, **59**, 719–727.
- 190 H.-S. Kim, C.-R. Lee, J.-H. Im, K.-B. Lee, T. Moehl, A. Marchioro, S.-J. Moon, R. Humphry-Baker, J.-H. Yum and J. E. Moser, *Sci. Rep.*, 2012, **2**, 591.
- 191 M. Lorenzon, V. Pinchetti, F. Bruni, W. K. Bae, F. Meinardi, V. I. Klimov and S. Brovelli, *Nano Lett.*, 2017, **17**, 1071–1081.
- 192 M. Lorenzon, S. Christodoulou, G. Vaccaro, J. Pedrini, F. Meinardi, I. Moreels and S. Brovelli, *Nat. Commun.*, 2015, **6**, 6434.
- 193 D. Meggiolaro, E. Mosconi and F. De Angelis, *ACS Energy Lett.*, 2017, **2**, 2794–2798.
- 194 M. Lorenzon, L. Sortino, Q. Akkerman, S. Accornero, J. Pedrini, M. Prato, V. Pinchetti, F. Meinardi, L. Manna and S. Brovelli, *Nano Lett.*, 2017, **17**, 3844–3853.
- 195 M. S. Abdou, F. P. Orfino, Y. Son and S. Holdcroft, *J. Am. Chem. Soc.*, 1997, **119**, 4518–4524.
- 196 H. Kautsky, *Trans. Faraday Soc.*, 1939, **35**, 216–219.
- 197 N. Aristidou, C. Eames, I. Sanchez-Molina, X. Bu, J. Kosco, M. S. Islam and S. A. Haque, *Nat. Commun.*, 2017, **8**, 15218.
- 198 S. D. Stranks, G. E. Eperon, G. Grancini, C. Menelaou, M. J. Alcocer, T. Leijtens, L. M. Herz, A. Petrozza and H. J. Snaith, *Science*, 2013, **342**, 341–344.
- 199 V. Sarritzu, N. Sestu, D. Marongiu, X. Chang, Q. Wang, S. Masi, S. Colella, A. Rizzo, A. Gocalinska, E. Pelucchi, M. L. Mercuri, F. Quochi, M. Saba, A. Mura and G. Bongiovanni, *Adv. Opt. Mater.*, 2018, **6**, 1701254.
- 200 J. A. Christians, P. A. Miranda Herrera and P. V. Kamat, *J. Am. Chem. Soc.*, 2015, **137**, 1530–1538.
- 201 E. Mosconi, J. M. Azpiroz and F. De Angelis, *Chem. Mater.*, 2015, **27**, 4885–4892.
- 202 H. Zhou, Q. Chen, G. Li, S. Luo, T.-b. Song, H.-S. Duan, Z. Hong, J. You, Y. Liu and Y. Yang, *Science*, 2014, **345**, 542–546.
- 203 X. Gong, M. Li, X. B. Shi, H. Ma, Z. K. Wang and L. S. Liao, *Adv. Funct. Mater.*, 2015, **25**, 6671–6678.
- 204 C. Müller, T. Glaser, M. Plogmeyer, M. Sendner, S. Döring, A. A. Bakulin, C. Brzuska, R. Scheer, M. S. Pschenichnikov, W. Kowalsky, A. Pucci and R. Lovrincic, *Chem. Mater.*, 2015, **27**, 7835–7841.
- 205 H. Wang, X. Li, M. Yuan and X. Yang, *Small*, 2018, **14**, 1703410.
- 206 L. Wu, H. Hu, Y. Xu, S. Jiang, M. Chen, Q. Zhong, D. Yang, Q. Liu, Y. Zhao, B. Sun, Q. Zhang and Y. Yin, *Nano Lett.*, 2017, **17**, 5799–5804.
- 207 B. Akbali, G. Topcu, T. Guner, M. Ozcan, M. M. Demir and H. Sahin, *Phys. Rev. Mater.*, 2018, **2**, 034601.
- 208 X. Zhang, X. Bai, H. Wu, X. Zhang, C. Sun, Y. Zhang, W. Zhang, W. Zheng, W. W. Yu and A. L. Rogach, *Angew. Chem.*, 2018, **130**, 3395–3400.

- 209 C. Geng, S. Xu, H. Zhong, A. L. Rogach and W. Bi, *Angew. Chem., Int. Ed.*, 2018, **57**, 9650–9654.
- 210 A. Jana and K. S. Kim, *ACS Energy Lett.*, 2018, **3**, 2120–2126.
- 211 A. M. A. Leguy, Y. Hu, M. Campoy-Quiles, M. I. Alonso, O. J. Weber, P. Azarhoosh, M. van Schilfgaarde, M. T. Weller, T. Bein, J. Nelson, P. Docampo and P. R. F. Barnes, *Chem. Mater.*, 2015, **27**, 3397–3407.
- 212 J. M. Frost, K. T. Butler, F. Brivio, C. H. Hendon, M. Van Schilfgaarde and A. Walsh, *Nano Lett.*, 2014, **14**, 2584–2590.
- 213 L. Zhang, M.-G. Ju and W. Liang, *Phys. Chem. Chem. Phys.*, 2016, **18**, 23174–23183.
- 214 S. N. Habisreutinger, T. Leijtens, G. E. Eperon, S. D. Stranks, R. J. Nicholas and H. J. Snaith, *Nano Lett.*, 2014, **14**, 5561–5568.
- 215 X. Zheng, B. Chen, J. Dai, Y. Fang, Y. Bai, Y. Lin, H. Wei, X. C. Zeng and J. Huang, *Nat. Energy*, 2017, **2**, 17102.
- 216 A. Dualeh, P. Gao, S. I. Seok, M. K. Nazeeruddin and M. Grätzel, *Chem. Mater.*, 2014, **26**, 6160–6164.
- 217 Q. Shao, L. Wang, L. Song, Y. Dong, C. Liang, J. He and J. Jiang, *J. Alloys Compd.*, 2017, **695**, 221–226.
- 218 Y. Zhao, C. Riimersma, F. Pietra, R. Koole, C. de Mello Donegá and A. Meijerink, *ACS Nano*, 2012, **6**, 9058–9067.
- 219 S. Wei, Y. Yang, X. Kang, L. Wang, L. Huang and D. Pan, *Chem. Commun.*, 2016, **52**, 7265–7268.
- 220 B. T. Diroll, G. Nedelcu, M. V. Kovalenko and R. D. Schaller, *Adv. Funct. Mater.*, 2017, **27**, 1606075.
- 221 Q. Jiang, M. Chen, J. Li, M. Wang, X. Zeng, T. Besara, J. Lu, Y. Xin, X. Shan, B. Pan, C. Wang, S. Lin, T. Siegrist, Q. Xiao and Z. Yu, *ACS Nano*, 2017, **11**, 1073–1079.
- 222 Y. Zhou, J. Chen, O. M. Bakr and H.-T. Sun, *Chem. Mater.*, 2018, **30**, 6589–6613.
- 223 F. C. Hanusch, E. Wiesenmayer, E. Mankel, A. Binek, P. Angloher, C. Fraunhofer, N. Giesbrecht, J. M. Feckl, W. Jaegermann, D. Johrendt, T. Bein and P. Docampo, *J. Phys. Chem. Lett.*, 2014, **5**, 2791–2795.
- 224 L. Protesescu, S. Yakunin, M. I. Bodnarchuk, F. Bertolotti, N. Masciocchi, A. Guagliardi and M. V. Kovalenko, *J. Am. Chem. Soc.*, 2016, **138**, 14202–14205.
- 225 L. Protesescu, S. Yakunin, S. Kumar, J. Bär, F. Bertolotti, N. Masciocchi, A. Guagliardi, M. Grotevent, I. Shorubalko, M. I. Bodnarchuk, C.-J. Shih and M. V. Kovalenko, *ACS Nano*, 2017, **11**, 3119–3134.
- 226 X. Zhang, H. Liu, W. Wang, J. Zhang, B. Xu, K. L. Karen, Y. Zheng, S. Liu, S. Chen, K. Wang and X. W. Sun, *Adv. Mater.*, 2017, **29**, 1606405.
- 227 D. Amgar, T. Binyamin, V. Uvarov and L. Etgar, *Nanoscale*, 2018, **10**, 6060–6068.
- 228 S. Huang, B. Wang, Q. Zhang, Z. Li, A. Shan and L. Li, *Adv. Opt. Mater.*, 2018, **6**, 1701106.
- 229 Y. Liu, G. Pan, R. Wang, H. Shao, H. Wang, W. Xu, H. Cui and H. Song, *Nanoscale*, 2018, **10**, 14067–14072.
- 230 M. Abdi-Jalebi, Z. Andaji-Garmaroudi, S. Cacovich, C. Stavrakas, B. Philippe, J. M. Richter, M. Alsari, E. P. Booker, E. M. Hutter, A. J. Pearson, S. Lilliu, T. J. Savenije, H. Rensmo, G. Divitini, C. Ducati, R. H. Friend and S. D. Stranks, *Nature*, 2018, **555**, 497–501.
- 231 B. Philippe, M. Saliba, J.-P. Correa-Baena, U. B. Cappel, S.-H. Turren-Cruz, M. Grätzel, A. Hagfeldt and H. k. Rensmo, *Chem. Mater.*, 2017, **29**, 3589–3596.
- 232 G. M. Dalpian and J. R. Chelikowsky, *Phys. Rev. Lett.*, 2006, **96**, 226802.
- 233 D. Cortecchia, S. Neutzner, A. R. Srimath Kandada, E. Mosconi, D. Meggiolaro, F. De Angelis, C. Soci and A. Petrozza, *J. Am. Chem. Soc.*, 2017, **139**, 39–42.
- 234 C. Quarti, N. Marchal and D. Beljonne, *J. Phys. Chem. Lett.*, 2018, **9**, 3416–3424.
- 235 S. Yang, Z. Lin, J. Wang, Y. Chen, Z. Liu, E. Yang, J. Zhang and Q. Ling, *ACS Appl. Mater. Interfaces*, 2018, **10**, 15980–15987.
- 236 A. García-Fernández, J. M. Bermúdez-García, S. Castro-García, A. L. Llamas-Saiz, R. Artiaga, J. J. López-Beceiro, M. Sánchez-Andújar and M. A. Señarís-Rodríguez, *Inorg. Chem.*, 2018, **57**, 3215–3222.
- 237 I. Neogi, A. Bruno, D. Bahulayan, T. W. Goh, B. Ghosh, R. Ganguly, D. Cortecchia, T. C. Sum, C. Soci, N. Mathews and S. G. Mhaisalkar, *ChemSusChem*, 2017, **10**, 3765–3772.
- 238 L. Mao, Y. Wu, C. C. Stoumpos, M. R. Wasielewski and M. G. Kanatzidis, *J. Am. Chem. Soc.*, 2017, **139**, 5210–5215.
- 239 S. Krishnamurthy, R. Naphade, W. J. Mir, S. Gosavi, S. Chakraborty, R. Vaidhyanathan and S. Ogale, *Adv. Opt. Mater.*, 2018, **6**, 1800751.
- 240 S. Wang, Y. Yao, J. Kong, S. Zhao, Z. Sun, Z. Wu, L. Li and J. Luo, *Chem. Commun.*, 2018, **54**, 4053–4056.
- 241 Z. Zhuang, C. Peng, G. Zhang, H. Yang, J. Yin and H. Fei, *Angew. Chem.*, 2017, **129**, 14603–14608.
- 242 H. Hu, S. Morris, X. Qiao, D. Zhao, T. Salim, B. Chen, E. Chia and Y.-M. Lam, *J. Mater. Chem. C*, 2018, **6**, 10301–10307.
- 243 S. Yang, W. Niu, A. L. Wang, Z. Fan, B. Chen, C. Tan, Q. Lu and H. Zhang, *Angew. Chem., Int. Ed.*, 2017, **56**, 4252–4255.
- 244 S. Bhaumik, S. A. Veldhuis, Y. F. Ng, M. Li, S. K. Muduli, T. C. Sum, B. Damodaran, S. Mhaisalkar and N. Mathews, *Chem. Commun.*, 2016, **52**, 7118–7121.
- 245 H. Zhu, M. T. Trinh, J. Wang, Y. Fu, P. P. Joshi, K. Miyata, S. Jin and X. Y. Zhu, *Adv. Mater.*, 2017, **29**, 1603072.
- 246 A. Swarnkar, W. J. Mir and A. Nag, *ACS Energy Lett.*, 2018, **3**, 286–289.
- 247 M. Liu, G. Zhong, Y. Yin, J. Miao, K. Li, C. Wang, X. Xu, C. Shen and H. Meng, *Adv. Sci.*, 2017, **4**, 1700335.
- 248 F. Yang, D. Hirotani, G. Kapil, M. A. Kamarudin, C. H. Ng, Y. Zhang, Q. Shen and S. Hayase, *Angew. Chem., Int. Ed.*, 2018, **57**.
- 249 W. Liu, Q. Lin, H. Li, K. Wu, I. n. Robel, J. M. Pietryga and V. I. Klimov, *J. Am. Chem. Soc.*, 2016, **138**, 14954–14961.
- 250 D. Parobek, B. J. Roman, Y. Dong, H. Jin, E. Lee, M. Sheldon and D. H. Son, *Nano Lett.*, 2016, **16**, 7376–7380.
- 251 H. Liu, Z. Wu, J. Shao, D. Yao, H. Gao, Y. Liu, W. Yu, H. Zhang and B. Yang, *ACS Nano*, 2017, **11**, 2239–2247.
- 252 F. Li, Z. Xia, Y. Gong, L. Gu and Q. Liu, *J. Mater. Chem. C*, 2017, **5**, 9281–9287.
- 253 P. K. Santra and P. V. Kamat, *J. Am. Chem. Soc.*, 2012, **134**, 2508–2511.
- 254 W. J. Mir, M. Jagadeeswararao, S. Das and A. Nag, *ACS Energy Lett.*, 2017, **2**, 537–543.

- 255 A. K. Guria, S. K. Dutta, S. D. Adhikari and N. Pradhan, *ACS Energy Lett.*, 2017, **2**, 1014–1021.
- 256 K. Xu, C. C. Lin, X. Xie and A. Meijerink, *Chem. Mater.*, 2017, **29**, 4265–4272.
- 257 G. Huang, C. Wang, S. Xu, S. Zong, J. Lu, Z. Wang, C. Lu and Y. Cui, *Adv. Mater.*, 2017, **29**, 1700095.
- 258 S. Das Adhikari, S. K. Dutta, A. Dutta, A. K. Guria and N. Pradhan, *Angew. Chem.*, 2017, **129**, 8872–8876.
- 259 A. Biswas, R. Bakthavatsalam and J. Kundu, *Chem. Mater.*, 2017, **29**, 7816–7825.
- 260 P. Arunkumar, K. H. Gil, S. Won, S. Unithrattil, Y. H. Kim, H. J. Kim and W. B. Im, *J. Phys. Chem. Lett.*, 2017, **8**, 4161–4166.
- 261 F. Li, Z. Xia, C. Pan, Y. Gong, L. Gu, Q. Liu and J. Z. Zhang, *ACS Appl. Mater. Interfaces*, 2018, **10**, 11739–11746.
- 262 G. Fang, D. Chen, S. Zhou, X. Chen, L. Lei, J. Zhong and Z. Ji, *J. Mater. Chem. C*, 2018, **6**, 5908–5915.
- 263 Q. A. Akkerman, D. Meggiolaro, Z. Dang, F. De Angelis and L. Manna, *ACS Energy Lett.*, 2017, **2**, 2183–2186.
- 264 T. C. Jellicoe, J. M. Richter, H. F. Glass, M. Tabachnyk, R. Brady, S. n. E. Dutton, A. Rao, R. H. Friend, D. Credginton, N. C. Greenham and M. L. Böhm, *J. Am. Chem. Soc.*, 2016, **138**, 2941–2944.
- 265 A. Wang, Y. Guo, F. Muhammad and Z. Deng, *Chem. Mater.*, 2017, **29**, 6493–6501.
- 266 D. Moghe, L. Wang, C. J. Traverse, A. Redoute, M. Sponseller, P. R. Brown, V. Bulović and R. R. Lunt, *Nano Energy*, 2016, **28**, 469–474.
- 267 G. Xing, M. H. Kumar, W. K. Chong, X. Liu, Y. Cai, H. Ding, M. Asta, M. Grätzel, S. Mhaisalkar, N. Mathews and T. C. Sum, *Adv. Mater.*, 2016, **28**, 8191–8196.
- 268 A. Wang, X. Yan, M. Zhang, S. Sun, M. Yang, W. Shen, X. Pan, P. Wang and Z. Deng, *Chem. Mater.*, 2016, **28**, 8132–8140.
- 269 M. Li, X. Zhang, K. Matras-Postolek, H.-S. Chen and P. Yang, *J. Mater. Chem. C*, 2018, **6**, 5506–5513.
- 270 F. Liu, C. Ding, Y. Zhang, T. S. Ropollés, T. Kamisaka, T. Toyoda, S. Hayase, T. Minemoto, K. Yoshino, S. Dai, M. Yanagida, H. Noguchi and Q. Shen, *J. Am. Chem. Soc.*, 2017, **139**, 16708–16719.
- 271 X. Zhang, W. Cao, W. Wang, B. Xu, S. Liu, H. Dai, S. Chen, K. Wang and X. W. Sun, *Nano Energy*, 2016, **30**, 511–516.
- 272 W. Van der Stam, J. J. Geuchies, T. Altantzis, K. H. Van Den Bos, J. D. Meeldijk, S. Van Aert, S. Bals, D. Vanmaekelbergh and C. de Mello Donega, *J. Am. Chem. Soc.*, 2017, **139**, 4087–4097.
- 273 H. C. Wang, W. Wang, A. C. Tang, H. Y. Tsai, Z. Bao, T. Ihara, N. Yarita, H. Tahara, Y. Kanemitsu, S. Chen and R. S. Liu, *Angew. Chem.*, 2017, **129**, 13838–13842.
- 274 Z.-J. Yong, S.-Q. Guo, J.-P. Ma, J. Zhang, Z.-Y. Li, Y.-M. Chen, B.-B. Zhang, Y. Zhou, J. Shu, J.-L. Gu, L.-R. Zheng, O. M. Bakr and H.-T. Sun, *J. Am. Chem. Soc.*, 2018, **140**, 9942–9951.
- 275 M. Leng, Z. Chen, Y. Yang, Z. Li, K. Zeng, K. Li, G. Niu, Y. He, Q. Zhou and J. Tang, *Angew. Chem., Int. Ed.*, 2016, **55**, 15012–15016.
- 276 M. Leng, Y. Yang, Z. Chen, W. Gao, J. Zhang, G. Niu, D. Li, H. Song, J. Zhang, S. Jin and J. Tang, *Nano Lett.*, 2018, **18**, 6076–6083.
- 277 M. Leng, Y. Yang, K. Zeng, Z. Chen, Z. Tan, S. Li, J. Li, B. Xu, D. Li, M. P. Hautzinger, Y. Fu, T. Zhai, L. Xu, G. Niu, S. Jin and J. Tang, *Adv. Funct. Mater.*, 2018, **28**, 1704446.
- 278 Y. Lou, M. Fang, J. Chen and Y. Zhao, *Chem. Commun.*, 2018, **54**, 3779–3782.
- 279 R. D. Nelson, K. Santra, Y. Wang, A. Hadi, J. W. Petrich and M. G. Panthani, *Chem. Commun.*, 2018, **54**, 3640–3643.
- 280 B. Yang, J. Chen, F. Hong, X. Mao, K. Zheng, S. Yang, Y. Li, T. Pullerits, W. Deng and K. Han, *Angew. Chem.*, 2017, **129**, 12645–12649.
- 281 R. Begum, M. R. Parida, A. L. Abdelhady, B. Murali, N. M. Alyami, G. H. Ahmed, M. N. Hedhili, O. M. Bakr and O. F. Mohammed, *J. Am. Chem. Soc.*, 2016, **139**, 731–737.
- 282 P. K. Nayak, M. Sendner, B. Wenger, Z. Wang, K. Sharma, A. J. Ramadan, R. Lovrincic, A. Pucci, P. K. Madhu and H. J. Snaith, *J. Am. Chem. Soc.*, 2018, **140**, 574–577.
- 283 H. Shao, X. Bai, H. Cui, G. Pan, P. Jing, S. Qu, J. Zhu, Y. Zhai, B. Dong and H. Song, *Nanoscale*, 2018, **10**, 1023–1029.
- 284 J. Zhang, Y. Yang, H. Deng, U. Farooq, X. Yang, J. Khan, J. Tang and H. Song, *ACS Nano*, 2017, **11**, 9294–9302.
- 285 S. Xiang, W. Li, Y. Wei, J. Liu, H. Liu, L. Zhu and H. Chen, *Nanoscale*, 2018, **10**, 9996–10004.
- 286 S. E. Creutz, E. N. Crites, M. C. De Siena and D. R. Gamelin, *Nano Lett.*, 2018, **18**, 1118–1123.
- 287 B. Yang, J. Chen, S. Yang, F. Hong, L. Sun, P. Han, T. Pullerits, W. Deng and K. Han, *Angew. Chem.*, 2018, **130**, 5457–5461.
- 288 L. Zhou, Y. F. Xu, B. X. Chen, D. B. Kuang and C. Y. Su, *Small*, 2018, **14**, 1703762.
- 289 J. Sun, J. Yang, J. I. Lee, J. H. Cho and M. S. Kang, *J. Phys. Chem. Lett.*, 2018, **9**, 1573–1583.
- 290 Q. Hu, Z. Li, Z. Tan, H. Song, C. Ge, G. Niu, J. Han and J. Tang, *Adv. Opt. Mater.*, 2018, **6**, 1700864.
- 291 L. Liu, J. Li and J. A. McLeod, *Nanoscale*, 2018, **10**, 11452–11459.
- 292 G. Pan, X. Bai, D. Yang, X. Chen, P. Jing, S. Qu, L. Zhang, D. Zhou, J. Zhu, W. Xu, B. Dong and H. Song, *Nano Lett.*, 2017, **17**, 8005–8011.
- 293 T. J. Milstein, D. M. Kroupa and D. R. Gamelin, *Nano Lett.*, 2018, **18**, 3792–3799.
- 294 X. Zhang, Y. Zhang, X. Zhang, W. Yin, Y. Wang, H. Wang, M. Lu, Z. Li, Z. Gu and W. Yu, *J. Mater. Chem. C*, 2018, **6**, 10101–10105.
- 295 D. Zhou, D. Liu, G. Pan, X. Chen, D. Li, W. Xu, X. Bai and H. Song, *Adv. Mater.*, 2017, **29**, 1704149.
- 296 J.-S. Yao, J. Ge, B.-N. Han, K.-H. Wang, H.-B. Yao, H.-L. Yu, J.-H. Li, B.-S. Zhu, J.-Z. Song, C. Chen, Q. Zhang, H.-B. Zeng, Y. Luo and S.-H. Yu, *J. Am. Chem. Soc.*, 2018, **140**, 3626–3634.
- 297 L. Qu and X. Peng, *J. Am. Chem. Soc.*, 2002, **124**, 2049–2055.
- 298 C. Pu and X. Peng, *J. Am. Chem. Soc.*, 2016, **138**, 8134–8142.

- 299 J. Kang and L.-W. Wang, *J. Phys. Chem. Lett.*, 2017, **8**, 489–493.
- 300 Y. Liu, H. Xiao and W. A. Goddard III, *Nano Lett.*, 2016, **16**, 3335–3340.
- 301 S. ten Brinck and I. Infante, *ACS Energy Lett.*, 2016, **1**, 1266–1272.
- 302 J. Pan, L. N. Quan, Y. Zhao, W. Peng, B. Murali, S. P. Sarmah, M. Yuan, L. Sinatra, N. M. Alyami, J. Liu, E. Yassitepe, Z. Yang, O. Voznyy, R. Comin, M. N. Hedhili, O. F. Mohammed, Z. H. Lu, D. H. Kim, E. H. Sargent and O. M. Bakr, *Adv. Mater.*, 2016, **28**, 8718–8725.
- 303 N. K. Noel, A. Abate, S. D. Stranks, E. S. Parrott, V. M. Burlakov, A. Goriely and H. J. Snaith, *ACS Nano*, 2014, **8**, 9815–9821.
- 304 C. Wang, A. S. Chesman and J. J. Jasieniak, *Chem. Commun.*, 2017, **53**, 232–235.
- 305 B. Luo, Y. C. Pu, S. A. Lindley, Y. Yang, L. Lu, Y. Li, X. Li and J. Z. Zhang, *Angew. Chem.*, 2016, **128**, 9010–9014.
- 306 Z. Liu, Y. Zhang, Y. Fan, Z. Chen, Z. Tang, J. Zhao, Y. Lv, J. Lin, X. Guo, J. Zhang and X. Liu, *ACS Appl. Mater. Interfaces*, 2018, **10**, 13053–13061.
- 307 T. Xuan, X. Yang, S. Lou, J. Huang, Y. Liu, J. Yu, H. Li, K.-L. Wong, C. Wang and J. Wang, *Nanoscale*, 2017, **9**, 15286–15290.
- 308 S. Gonzalez-Carrero, L. Francés-Soriano, M. González-Béjar, S. Agouram, R. E. Galian and J. Pérez-Prieto, *Small*, 2016, **12**, 5245–5250.
- 309 L. Wu, Q. Zhong, D. Yang, M. Chen, H. Hu, Q. Pan, H. Liu, M. Cao, Y. Xu, B. Sun and Q. Zhang, *Langmuir*, 2017, **33**, 12689–12696.
- 310 Q.-L. Li, W.-X. Lu, N. Wan and S.-N. Ding, *Chem. Commun.*, 2016, **52**, 12342–12345.
- 311 L. Rao, Y. Tang, C. Yan, J. Li, G. Zhong, K. Tang, B. Yu, Z. Li and J. Z. Zhang, *J. Mater. Chem. C*, 2018, **6**, 5375–5383.
- 312 F. Liu, Y. Zhang, C. Ding, S. Kobayashi, T. Izuishi, N. Nakazawa, T. Toyoda, T. Ohta, S. Hayase, T. Minemoto, K. Yoshino, S. Dai and Q. Shen, *ACS Nano*, 2017, **11**, 10373–10383.
- 313 H. Wang, N. Sui, X. Bai, Y. Zhang, Q. Rice, F. J. Seo, Q. Zhang, V. L. Colvin and W. W. Yu, *J. Phys. Chem. Lett.*, 2018, **9**, 4166–4173.
- 314 C. Lu, H. Li, K. Kolodziejski, C. Dun, W. Huang, D. Carroll and S. M. Geyer, *Nano Res.*, 2018, **11**, 762–768.
- 315 K. P. Mubiayi, N. Moloto and M. J. Moloto, *CrystEngComm*, 2018, **20**, 5275–5280.
- 316 H. Wu, Y. Zhang, M. Lu, X. Zhang, C. Sun, T. Zhang, V. L. Colvin and W. Y. William, *Nanoscale*, 2018, **10**, 4173–4178.
- 317 J. Pan, S. P. Sarmah, B. Murali, I. Dursun, W. Peng, M. R. Parida, J. Liu, L. Sinatra, N. Alyami, C. Zhao, E. Alarousu, T. K. Ng, B. S. Ooi, O. M. Bakr and O. F. Mohammed, *J. Phys. Chem. Lett.*, 2015, **6**, 5027–5033.
- 318 G. Li, J. Huang, H. Zhu, Y. Li, J.-X. Tang and Y. Jiang, *Chem. Mater.*, 2018, **30**, 6099–6107.
- 319 S. A. Veldhuis, Y. K. E. Tay, A. Bruno, S. S. Dintakurti, S. Bhaumik, S. K. Muduli, M. Li, N. Mathews, T. C. Sum and S. G. Mhaisalkar, *Nano Lett.*, 2017, **17**, 7424–7432.
- 320 G. H. Ahmed, J. K. El-Demellawi, J. Yin, J. Pan, D. B. Velusamy, M. N. Hedhili, E. Alarousu, O. M. Bakr, H. N. Alshareef and O. F. Mohammed, *ACS Energy Lett.*, 2018, 2301–2307.
- 321 J. Y. Woo, Y. Kim, J. Bae, T. G. Kim, J. W. Kim, D. C. Lee and S. Jeong, *Chem. Mater.*, 2017, **29**, 7088–7092.
- 322 B. A. Koscher, J. K. Swabeck, N. D. Bronstein and A. P. Alivisatos, *J. Am. Chem. Soc.*, 2017, **139**, 6566–6569.
- 323 T. Ahmed, S. Seth and A. Samanta, *Chem. Mater.*, 2018, **30**, 3633–3637.
- 324 Q. Jing, M. Zhang, X. Huang, X. Ren, P. Wang and Z. Lu, *Nanoscale*, 2017, **9**, 7391–7396.
- 325 B. J. Bohn, Y. Tong, M. Gramlich, M. L. Lai, M. Döblinger, K. Wang, R. L. Z. Hoye, P. Müller-Buschbaum, S. D. Stranks, A. S. Urban, L. Polavarapu and J. Feldmann, *Nano Lett.*, 2018, **18**, 5231–5238.
- 326 F. Zhang, S. Huang, P. Wang, X. Chen, S. Zhao, Y. Dong and H. Zhong, *Chem. Mater.*, 2017, **29**, 3793–3799.
- 327 L. Ruan, W. Shen, A. Wang, Q. Zhou, H. Zhang and Z. Deng, *Nanoscale*, 2017, **9**, 7252–7259.
- 328 S. R. Smock, T. J. Williams and R. L. Brutchey, *Angew. Chem.*, 2018, **130**, 11885–11889.
- 329 Q. Li, H. Li, H. Shen, F. Wang, F. Zhao, F. Li, X. Zhang, D. Li, X. Jin and W. Sun, *ACS Photonics*, 2017, **4**, 2504–2512.
- 330 F. Krieg, S. T. Ochsenbein, S. Yakunin, S. ten Brinck, P. Aellen, A. Süess, B. Clerc, D. Guggisberg, O. Nazarenko, Y. Shynkarenko, S. Kumar, C.-J. Shih, I. Infante and M. V. Kovalenko, *ACS Energy Lett.*, 2018, **3**, 641–646.
- 331 J. Pan, Y. Shang, J. Yin, M. De Bastiani, W. Peng, I. Dursun, L. Sinatra, A. M. El-Zohry, M. N. Hedhili, A.-H. Emwas, O. F. Mohammed, Z. Ning and O. M. Bakr, *J. Am. Chem. Soc.*, 2018, **140**, 562–565.
- 332 H. Sun, Z. Yang, M. Wei, W. Sun, X. Li, S. Ye, Y. Zhao, H. Tan, E. L. Kynaston, T. B. Schon, H. Yan, Z.-H. Lu, G. A. Ozin, E. H. Sargent and D. S. Seferos, *Adv. Mater.*, 2017, **29**, 1701153.
- 333 G. Li, F. W. R. Rivarola, N. J. Davis, S. Bai, T. C. Jellicoe, F. de la Peña, S. Hou, C. Ducati, F. Gao, R. H. Friend, N. C. Greenham and Z.-K. Tan, *Adv. Mater.*, 2016, **28**, 3528–3534.
- 334 F. Palazon, F. Di Stasio, Q. A. Akkerman, R. Krahne, M. Prato and L. Manna, *Chem. Mater.*, 2016, **28**, 2902–2906.
- 335 F. Palazon, Q. A. Akkerman, M. Prato and L. Manna, *ACS Nano*, 2015, **10**, 1224–1230.
- 336 S. Pathak, N. Sakai, F. Wisnivesky Rocca Rivarola, S. D. Stranks, J. Liu, G. E. Eperon, C. Ducati, K. Wojciechowski, J. T. Griffiths, A. A. Haghhighirad, A. Pellaroque, R. H. Friend and H. J. Snaith, *Chem. Mater.*, 2015, **27**, 8066–8075.
- 337 K. Ma, X.-Y. Du, Y.-W. Zhang and S. Chen, *J. Mater. Chem. C*, 2017, **5**, 9398–9404.
- 338 Y. H. Song, J. S. Yoo, B. K. Kang, S. H. Choi, E. K. Ji, H. S. Jung and D. H. Yoon, *Nanoscale*, 2016, **8**, 19523–19526.
- 339 D. N. Minh, S. Eom, L. A. T. Nguyen, J. Kim, J. H. Sim, C. Seo, J. Nam, S. Lee, S. Suk, J. Kim and Y. Kang, *Adv. Mater.*, 2018, **30**, 1802555.
- 340 W. Cha, H.-J. Kim, S. Lee and J. Kim, *J. Mater. Chem. C*, 2017, **5**, 6667–6671.
- 341 C. C. Lin, D.-H. Jiang, C.-C. Kuo, C.-J. Cho, Y.-H. Tsai, T. Satoh and C. Su, *ACS Appl. Mater. Interfaces*, 2018, **10**, 2210–2215.

- 342 P.-C. Tsai, J.-Y. Chen, E. Ercan, C.-C. Chueh, S.-H. Tung and W.-C. Chen, *Small*, 2018, **14**, 1704379.
- 343 H. Liao, S. Guo, S. Cao, L. Wang, F. Gao, Z. Yang, J. Zheng and W. Yang, *Adv. Opt. Mater.*, 2018, **6**, 1800346.
- 344 Y. Li, Y. Lv, Z. Guo, L. Dong, J. Zheng, C. Chai, N. Chen, Y. Lu and C. Chen, *ACS Appl. Mater. Interfaces*, 2018, **10**, 15888–15894.
- 345 M. Meyns, M. Perálvarez, A. Heuer-Jungemann, W. Hertog, M. Ibáñez, R. Nafria, A. Genc, J. Arbiol, M. V. Kovalenko and J. Carreras, *ACS Appl. Mater. Interfaces*, 2016, **8**, 19579–19586.
- 346 A. Pan, M. J. Jurow, F. Qiu, J. Yang, B. Ren, J. J. Urban, L. He and Y. Liu, *Nano Lett.*, 2017, **17**, 6759–6765.
- 347 S. Hou, Y. Guo, Y. Tang and Q. Quan, *ACS Appl. Mater. Interfaces*, 2017, **9**, 18417–18422.
- 348 S. Yang, F. Zhang, J. Tai, Y. Li, Y. Yang, H. Wang, J. Zhang, Z. Xie, B. Xu, H. Zhong, K. Liu and B. Yang, *Nanoscale*, 2018, **10**, 5820–5826.
- 349 W. Xu, Z. Cai, F. Li, J. Dong, Y. Wang, Y. Jiang and X. Chen, *Nano Res.*, 2017, **10**, 2692–2698.
- 350 S. N. Raja, Y. Bekenstein, M. A. Koc, S. Fischer, D. Zhang, L. Lin, R. O. Ritchie, P. Yang and A. P. Alivisatos, *ACS Appl. Mater. Interfaces*, 2016, **8**, 35523–35533.
- 351 X. Shen, C. Sun, X. Bai, X. Zhang, Y. Wang, Y. Wang, H. Song and W. W. Yu, *ACS Appl. Mater. Interfaces*, 2018, **10**, 16768–16775.
- 352 K. Chen, X. Deng, G. Dodekatos and H. Tüysüz, *J. Am. Chem. Soc.*, 2017, **139**, 12267–12273.
- 353 Y. C. Wong, J. De Andrew Ng and Z. K. Tan, *Adv. Mater.*, 2018, **30**, 1800774.
- 354 H. Zhang, X. Wang, Q. Liao, Z. Xu, H. Li, L. Zheng and H. Fu, *Adv. Funct. Mater.*, 2017, **27**, 1604382.
- 355 X. Yang, T. Xu, Y. Zhu, J. Cai, K. Gu, J. Zhu, Y. Wang, J. Shen and C. Li, *J. Mater. Chem. C*, 2018, **6**, 7971–7975.
- 356 Y. Wei, X. Deng, Z. Xie, X. Cai, S. Liang, P. a. Ma, Z. Hou, Z. Cheng and J. Lin, *Adv. Funct. Mater.*, 2017, **27**, 1703535.
- 357 J.-N. Liu, W.-B. Bu and J.-L. Shi, *Acc. Chem. Res.*, 2015, **48**, 1797–1805.
- 358 D. Gerion, F. Pinaud, S. C. Williams, W. J. Parak, D. Zanchet, S. Weiss and A. P. Alivisatos, *J. Phys. Chem. B*, 2001, **105**, 8861–8871.
- 359 D. K. Yi, S. T. Selvan, S. S. Lee, G. C. Papaefthymiou, D. Kundaliya and J. Y. Ying, *J. Am. Chem. Soc.*, 2005, **127**, 4990–4991.
- 360 W. Stöber, A. Fink and E. Bohn, *J. Colloid Interface Sci.*, 1968, **26**, 62–69.
- 361 J. Ziegler, S. Xu, E. Kucur, F. Meister, M. Batentschuk, F. Gindele and T. Nann, *Adv. Mater.*, 2008, **20**, 4068–4073.
- 362 D. N. Dirin, L. Protesescu, D. Trummer, I. V. Kochetygov, S. Yakunin, F. Krumeich, N. P. Stadie and M. V. Kovalenko, *Nano Lett.*, 2016, **16**, 5866–5874.
- 363 V. Malgras, S. Tominaka, J. W. Ryan, J. Henzie, T. Takei, K. Ohara and Y. Yamauchi, *J. Am. Chem. Soc.*, 2016, **138**, 13874–13881.
- 364 V. Malgras, J. Henzie, T. Takei and Y. Yamauchi, *Chem. Commun.*, 2017, **53**, 2359–2362.
- 365 V. Malgras, J. Henzie, T. Takei and Y. Yamauchi, *Angew. Chem.*, 2018, **130**, 9019–9023.
- 366 D. H. Park, J. S. Han, W. Kim and H. S. Jang, *Dyes Pigm.*, 2018, **149**, 246–252.
- 367 Z. Hu, Z. Liu, Y. Bian, S. Li, X. Tang, J. Du, Z. Zang, M. Zhou, W. Hu, Y. Tian and Y. Leng, *Adv. Opt. Mater.*, 2018, **6**, 1700997.
- 368 Q. Zhong, M. Cao, H. Hu, D. Yang, M. Chen, P. Li, L. Wu and Q. Zhang, *ACS Nano*, 2018, **12**, 8579–8587.
- 369 N. Ding, D. Zhou, X. Sun, W. Xu, H. Xu, G. Pan, D. Li, S. Zhang, B. Dong and H. Song, *Nanotechnology*, 2018, **29**, 345703.
- 370 X. Li, Y. Wang, H. Sun and H. Zeng, *Adv. Mater.*, 2017, **29**, 1701185.
- 371 W. Chen, J. Hao, W. Hu, Z. Zang, X. Tang, L. Fang, T. Niu and M. Zhou, *Small*, 2017, **13**, 1604085.
- 372 S. K. Balakrishnan and P. V. Kamat, *ACS Energy Lett.*, 2016, **2**, 88–93.
- 373 B. J. Roman, J. Otto, C. Galik, R. Downing and M. Sheldon, *Nano Lett.*, 2017, **17**, 5561–5566.
- 374 S. Guarnera, A. Abate, W. Zhang, J. M. Foster, G. Richardson, A. Petrozza and H. J. Snaith, *J. Phys. Chem. Lett.*, 2015, **6**, 432–437.
- 375 T. Leijtens, B. Lauber, G. E. Eperon, S. D. Stranks and H. J. Snaith, *J. Phys. Chem. Lett.*, 2014, **5**, 1096–1102.
- 376 J. Y. Sun, F. T. Rabouw, X. F. Yang, X. Y. Huang, X. P. Jing, S. Ye and Q. Y. Zhang, *Adv. Funct. Mater.*, 2017, **27**, 1704371.
- 377 Y. Wei, H. Xiao, Z. Xie, S. Liang, S. Liang, X. Cai, S. Huang, A. A. Al Kheraif, H. S. Jang, Z. Cheng and J. Lin, *Adv. Opt. Mater.*, 2018, **6**, 1701343.
- 378 Z. Zhao, Z. Wu, J. Cheng, L. Jing and Y. Hou, *J. Phys. Chem. C*, 2018, **122**, 16887–16893.
- 379 Z. Chen, Z.-G. Gu, W.-Q. Fu, F. Wang and J. Zhang, *ACS Appl. Mater. Interfaces*, 2016, **8**, 28737–28742.
- 380 C. Zhang, B. Wang, W. Li, S. Huang, L. Kong, Z. Li and L. Li, *Nat. Commun.*, 2017, **8**, 1138.
- 381 G. Yang, Q. Fan, B. Chen, Q. Zhou and H. Zhong, *J. Mater. Chem. C*, 2016, **4**, 11387–11391.
- 382 S. Lou, T. Xuan, C. Yu, M. Cao, C. Xia, J. Wang and H. Li, *J. Mater. Chem. C*, 2017, **5**, 7431–7435.
- 383 A. Loiudice, S. Saris, E. Oveisi, D. T. Alexander and R. Buonsanti, *Angew. Chem., Int. Ed.*, 2017, **56**, 10696–10701.
- 384 Z. J. Li, E. Hofman, J. Li, A. H. Davis, C. H. Tung, L. Z. Wu and W. Zheng, *Adv. Funct. Mater.*, 2018, **28**, 1704288.
- 385 S. Wang, C. Bi, J. Yuan, L. Zhang and J. Tian, *ACS Energy Lett.*, 2018, **3**, 245–251.
- 386 B. Wang, C. Zhang, S. Huang, Z. Li, L. Kong, L. Jin, J. Wang, K. Wu and L. Li, *ACS Appl. Mater. Interfaces*, 2018, **10**, 23303–23310.
- 387 Z. Ning, X. Gong, R. Comin, G. Walters, F. Fan, O. Voznyy, E. Yassitepe, A. Buin, S. Hoogland and E. H. Sargent, *Nature*, 2015, **523**, 324.
- 388 K.-H. Wang, L. Wu, L. Li, H.-B. Yao, H.-S. Qian and S.-H. Yu, *Angew. Chem., Int. Ed.*, 2016, **55**, 8328–8332.
- 389 X. Zhang, B. Xu, J. Zhang, Y. Gao, Y. Zheng, K. Wang and X. W. Sun, *Adv. Funct. Mater.*, 2016, **26**, 4595–4600.

- 390 X. Zhang, Z. Jin, J. Zhang, D. Bai, H. Bian, K. Wang, J. Sun, Q. Wang and S. F. Liu, *ACS Appl. Mater. Interfaces*, 2018, **10**, 7145–7154.
- 391 W. Shen, L. Ruan, Z. Shen and Z. Deng, *Chem. Commun.*, 2018, **54**, 2804–2807.
- 392 P. Song, B. Qiao, D. Song, Z. Liang, D. Gao, J. Cao, Z. Shen, Z. Xu and S. Zhao, *J. Alloys Compd.*, 2018, **767**, 98–105.
- 393 Q. A. Akkerman, S. Park, E. Radicchi, F. Nunzi, E. Mosconi, F. De Angelis, R. Brescia, P. Rastogi, M. Prato and L. Manna, *Nano Lett.*, 2017, **17**, 1924–1930.
- 394 Z. Liu, Y. Bekenstein, X. Ye, S. C. Nguyen, J. Swabeck, D. Zhang, S.-T. Lee, P. Yang, W. Ma and A. P. Alivisatos, *J. Am. Chem. Soc.*, 2017, **139**, 5309–5312.
- 395 Y. Zhang, M. I. Saidaminov, I. Dursun, H. Yang, B. Murali, E. Alarousu, E. Yengel, B. A. Alshankiti, O. M. Bakr and O. F. Mohammed, *J. Phys. Chem. Lett.*, 2017, **8**, 961–965.
- 396 Q. A. Akkerman, A. L. Abdelhady and L. Manna, *J. Phys. Chem. Lett.*, 2018, **9**, 2326–2337.
- 397 L. N. Quan, R. Quintero-Bermudez, O. Voznyy, G. Walters, A. Jain, J. Z. Fan, X. Zheng, Z. Yang and E. H. Sargent, *Adv. Mater.*, 2017, **29**, 1605945.
- 398 J. Xu, W. Huang, P. Li, D. R. Onken, C. Dun, Y. Guo, K. B. Ucer, C. Lu, H. Wang, S. M. Geyer, R. T. Williams and D. L. Carroll, *Adv. Mater.*, 2017, **29**, 1703703.
- 399 Y. Wang, D. Yu, Z. Wang, X. Li, X. Chen, V. Nalla, H. Zeng and H. Sun, *Small*, 2017, **13**, 1701587.
- 400 X. Chen, F. Zhang, Y. Ge, L. Shi, S. Huang, J. Tang, Z. Lv, L. Zhang, B. Zou and H. Zhong, *Adv. Funct. Mater.*, 2018, **28**, 1706567.
- 401 T. Xuan, S. Lou, J. Huang, L. Cao, X. Yang, H. Li and J. Wang, *Nanoscale*, 2018, **10**, 9840–9844.
- 402 C. Jia, H. Li, X. Meng and H. Li, *Chem. Commun.*, 2018, **54**, 6300–6303.
- 403 Y.-M. Chen, Y. Zhou, Q. Zhao, J.-Y. Zhang, J.-P. Ma, T.-T. Xuan, S.-Q. Guo, Z.-J. Yong, J. Wang, Y. Kuroiwa, C. Moriyoshi and H.-T. Sun, *ACS Appl. Mater. Interfaces*, 2018, **10**, 15905–15912.
- 404 X. Zhang, H.-C. Wang, A.-C. Tang, S.-Y. Lin, H.-C. Tong, C.-Y. Chen, Y.-C. Lee, T.-L. Tsai and R.-S. Liu, *Chem. Mater.*, 2016, **28**, 8493–8497.
- 405 Z. Li, L. Kong, S. Huang and L. Li, *Angew. Chem.*, 2017, **129**, 8246–8250.
- 406 L. Xu, J. Chen, J. Song, J. Li, J. Xue, Y. Dong, B. Cai, Q. Shan, B. Han and H. Zeng, *ACS Appl. Mater. Interfaces*, 2017, **9**, 26556–26564.
- 407 Y. Liu, F. Li, Q. Liu and Z. Xia, *Chem. Mater.*, 2018, **30**, 6922–6929.
- 408 V. González-Pedro, S. A. Veldhuis, R. Begum, M. J. Bañuls, A. Bruno, N. Mathews, S. Mhaisalkar and Á. Maquieira, *ACS Energy Lett.*, 2018, **3**, 1409–1414.
- 409 A. Pan, J. Wang, M. J. Jurow, M. Jia, Y. Liu, Y. Wu, Y. Zhang, L. He and Y. Liu, *Chem. Mater.*, 2018, **30**, 2771–2780.
- 410 H. C. Yoon, S. Lee, J. K. Song, H. Yang and Y. R. Do, *ACS Appl. Mater. Interfaces*, 2018, **10**, 11756–11767.
- 411 S. Liu and X. Luo, *LED packaging for lighting applications: design, manufacturing, and testing*, John Wiley & Sons, 2011.
- 412 M. Bahadur, A. W. Norris, A. Zarifsi, J. S. Alger and C. C. Windiate, Sixth International Conference on Solid State Lighting, 2006.
- 413 J. Hai, H. Li, Y. Zhao, F. Chen, Y. Peng and B. Wang, *Chem. Commun.*, 2017, **53**, 5400–5403.
- 414 R. Zhang, H. Lin, Y. Yu, D. Chen, J. Xu and Y. Wang, *Laser Photonics Rev.*, 2014, **8**, 158–164.
- 415 X. Di, Z. Hu, J. Jiang, M. He, L. Zhou, W. Xiang and X. Liang, *Chem. Commun.*, 2017, **53**, 11068–11071.
- 416 S. Liu, Y. Luo, M. He, X. Liang and W. Xiang, *J. Eur. Ceram. Soc.*, 2017, **38**, 1998–2004.
- 417 B. Ai, C. Liu, J. Wang, J. Xie, J. Han and X. Zhao, *J. Am. Ceram. Soc.*, 2016, **99**, 2875–2877.
- 418 B. Ai, C. Liu, Z. Deng, J. Wang, J. Han and X. Zhao, *Phys. Chem. Chem. Phys.*, 2017, **19**, 17349–17355.
- 419 R. Yuan, L. Shen, C. Shen, J. Liu, L. Zhou, W. Xiang and X. Liang, *Chem. Commun.*, 2018, **54**, 3395–3398.
- 420 M. C. Brennan, J. E. Herr, T. S. Nguyen-Beck, J. Zinna, S. Draguta, S. Rouvimov, J. Parkhill and M. Kuno, *J. Am. Chem. Soc.*, 2017, **139**, 12201–12208.
- 421 N. Reitinger, A. Hohenau, S. Köstler, J. R. Krenn and A. Leitner, *Phys. Status Solidi A*, 2011, **208**, 710–714.
- 422 J. Zhou, F. Huang, H. Lin, Z. Lin, J. Xu and Y. Wang, *J. Mater. Chem. C*, 2016, **4**, 7601–7606.
- 423 Y. Ohno, Fourth International Conference on Solid State Lighting, 2004.
- 424 J. Zhang, R. Hu, X. Yu, B. Xie and X. Luo, *Opt. Laser Technol.*, 2017, **88**, 161–165.